

# Optical tweezers for advanced microscopy

by

Anneke Erasmus



UNIVERSITEIT  
iYUNIVESITHI  
STELLENBOSCH  
UNIVERSITY

100  
1918 · 2018

*Thesis presented in partial fulfilment of the requirements for  
the degree of Master of Science (Physics) in the Faculty of  
Science at Stellenbosch University*

Supervisor: Prof. E.G. Rohwer

Co-supervisor: Dr. P.H. Neethling; Dr. G.W. Bosman

March 2018

# Declaration

By submitting this thesis electronically, I declare that the entirety of the work contained therein is my own, original work, that I am the sole author thereof (save to the extent explicitly otherwise stated), that reproduction and publication thereof by Stellenbosch University will not infringe any third party rights and that I have not previously in its entirety or in part submitted it for obtaining any qualification.

Date: ..... 2017/12/07 .....

Copyright © 2018 Stellenbosch University  
All rights reserved.

# Abstract

## Optical tweezers for advanced microscopy

A. Erasmus

*Department of Physics,  
University of Stellenbosch,  
Private Bag X1, Matieland 7602, South Africa.*

Thesis: MSc (Physics)

March 2018

The integration of lasers into microscopy has enabled new areas of research and expanded existing ones. Not only can one now image samples to resolutions and contrast unheard of before lasers became common, but one can now use lasers to exert minuscule forces on micron sized structures in your sample. This is achieved by creating a stable, single beam optical trap by tightly focusing a laser onto the sample containing micron-sized particles submerged in a fluid. Moving the trap position allows for the manipulation of micron-sized particles inside the sample. Such an optical trap is known as optical tweezers. In this work, optical tweezers are constructed and the trap is characterized by calibrating the picoNewton sized forces applied to micron-sized particles close to the trap centre. Applications of optical tweezers can be found in various aspects of biophotonics, some of which are discussed in this thesis. Using the constructed optical tweezers, the intracellular forces of molecular motors inside an onion cell were measured and the results are discussed. The optical tweezers setup can be expanded to include different imaging techniques. Two such imaging techniques, namely nonlinear microscopy and ptychography, a lensless imaging technique, are discussed in detail. Linear fluorescence micrographs were taken with the setup to illustrate how such an integration would work. Ptychography was demonstrated in a separate imaging setup to illustrate the underlying principles. In this fashion, the individual components are investigated and evaluated separately, with the ultimate goal of incorporating all of these techniques in a truly multimodal microscopy platform.

# Uittreksel

## Optiese-tangetjies vir gevorderde mikroskopie

*(“Optical tweezers for advanced microscopy”)*

A. Erasmus

*Departement Fisika,  
Universiteit van Stellenbosch,  
Privaatsak X1, Matieland 7602, Suid Afrika.*

Tesis: MSc (Fisika)

Maart 2018

Die integrasie van lasers in mikroskopie het dit moontlik gemaak om nuwe navorsingsgebiede te betree en bestaandes uit te brei. Met die ontwikkeling van hierdie tegnologie, kan monsters afgebeeld word met resolusies en kontras ongehoord van voordat lasers algemeen geword het. Verder word lasers toegepas om minimale kragte op mikroskopiese strukture in die monster uit te oefen. Dit word behaal deur 'n laser skerp op die monster te fokus, wat 'n stabiele, enkelstraal optiese val skep. Deur die optiese val-posisie relatief tot die monster te beweeg, kan die mikroskopiese deeltjies binne die monster gemanipuleer word. Hierdie optiese val is bekend as 'n optiese-tangetjie. In hierdie projek is 'n optiese-tangetjie gebou, die posisie van mikroskopiese deeltjies is oor tyd gemeet en so, indirek, is die kragte op die deeltjie waar geneem. Die kragte in die optiese val opstelling is op hierdie manier gekalibreer. Optiese-tangetjies het verskeie toepassings in biofotonika, waarvan sommige in hierdie tesis bespreek word. Een so 'n toepassing is die meet van intrasellulêre kragte van molekulêre motors binne 'n uiesel. Hierdie kragte is gemeet en die resultate word bespreek. Die optiese-tangetjie-opstelling is uitgebrei om verskillende afbeeldings tegnieke in te sluit. Een so 'n afbeeldings tegnieke wat bespreek is, is nie-lineêre mikroskopie. Lineêre floresensie-mikrograwe is geneem met die opstelling om te illustreer hoe so 'n integrasie sou werk. Nog 'n afbeeldings tegniek is ptychography. Ptychography is 'n tegniek wat 'n monster afbeeld sonder 'n lens. Dit is gedemonstreer in 'n afsonderlike afbeeldingsopstelling om die onderliggende beginsels te illustreer. Op hierdie manier word die individuele komponente afsonderlik ondersoek en geëvalueer, met die uiteindelijke doel om al hierdie tegnieke in 'n werklike multimodale mikroskopie opstelling in te sluit.

# Acknowledgements

I would like to express my sincere gratitude to Prof Rohwer, Dr Neethling, and Dr Bosman for their continuous support on this project, their patience, guidance, and motivation. Thank you also to the Laser Research Institute (LRI) team for insightful comments and valuable discussions. I am grateful for the positive environment created at the department and expressed through my supervisors that allow students to grow in their work. Thank you to Eric Hopmann and Dr Dirk Spangenberg for their insights and help on the ptychography section.

I would like to thank my parents, family, and friends for providing me with unfailing support and continuous encouragement throughout my years of study and through the process of my Master's and writing this thesis.

Lastly, I would like to thank the Harry Crossley scholarship and CSIR for financial support during my Master's.

# Contents

Declaration	i
Abstract	ii
Uittreksel	iii
Acknowledgements	iv
Contents	v
List of Figures	vii
List of Tables	ix
<b>1 Overview</b>	<b>1</b>
<b>2 Background and theory</b>	<b>3</b>
2.1 Multiphoton microscopy . . . . .	3
2.2 Optical tweezers . . . . .	9
2.3 Characterization of the optical tweezers . . . . .	12
2.4 Applications of the optical tweezers . . . . .	20
2.5 Iterative ptychographic imaging algorithms . . . . .	23
<b>3 Experimental setups</b>	<b>32</b>
3.1 Setup for the optical tweezers . . . . .	32
3.2 Characterizing the optical tweezers by force calibration setup . . . . .	42
3.3 Setup for the measurement of the stall forces of molecular motors . . . . .	45
3.4 Setup for the integration of optical tweezers with fluorescence microscopy	46
3.5 Setup for ptychography . . . . .	48
<b>4 Results and discussion</b>	<b>49</b>
4.1 Optical tweezers . . . . .	49
4.2 Fluorescence measurements . . . . .	57
4.3 Ptychography . . . . .	58
<b>5 Summary</b>	<b>66</b>
<b>Appendices</b>	<b>68</b>
<b>A Ptychography code</b>	<b>69</b>
A.1 PIE . . . . .	69

<i>CONTENTS</i>	<b>vi</b>
A.2 ePIE . . . . .	71
A.3 Experimental results . . . . .	77
<b>List of References</b>	<b>84</b>

# List of Figures

2.1	The Jablonski diagrams of linear and nonlinear processes: linear fluorescence, two photon fluorescence, second harmonic generation, third harmonic generation, and coherent anti-Stokes Raman spectroscopy. . . . .	3
2.2	Linear fluorescence occurs throughout a large region of the beam waist. While, two photon absorption fluorescence occurs in a relatively smaller region [1]. . .	4
2.3	Two photon fluorescence and SHG imaging of a labeled hippocampal slice culture sample from [2]. . . . .	6
2.4	The improvement using a compressed pulse, instead of an uncompressed pulse, for imaging a porcine skin sample is illustrated using two photon fluorescence, SHG and THG [3]. . . . .	8
2.5	Unstable, single beam trapping of particles [4]. . . . .	10
2.6	Stable trapping using two counter propagating beams, shown by Ashkin [4]. .	10
2.7	Stable, single beam, optical trapping is possible by creating a sharp focus of the beam [5]. . . . .	10
2.8	Optical trapping of a particle is due to momentum imparted to the particle in the direction of the focus. . . . .	11
2.9	The power spectrum used in the power spectral density method is plotted. . .	20
2.10	The power spectrum is simulated for different corner frequencies. . . . .	20
2.11	Molecular motors transport cargo along tracks in the cytoskeleton [6]. . . . .	21
2.12	Optical tweezers can be used to study the step size of molecular motors [7]. . .	22
2.13	Optical tweezers can be used to study use of vesicles as microreaction vessels [8].	23
2.14	The probe is scanned across the sample with significant overlap between neighbouring probe positions. . . . .	25
2.15	An illustration describing the anular spectrum and spatial frequencies. . . . .	30
2.16	Light from a point $P$ is captured on a screen representing the detector. . . . .	30
3.1	The setup of the optical tweezers. . . . .	32
3.2	Oil is placed on the oil immersion microscope. . . . .	34
3.3	The 10 $\mu\text{m}$ spacing grid of the grid distortion target slide. . . . .	36
3.4	The air force target resolution mask is imaged and line outs taken to determine the image resolution of the setup. . . . .	37
3.5	The power in the trap is plotted for various laser current settings. . . . .	38
3.6	Sample preparation of silica beads used for optical tweezing. . . . .	39
3.7	The piezo drivers are calibrated in the $x$ and $y$ coordinates of the trapping plane.	40
3.8	The difference between trapping a single bead and trapping multiple beads can be seen on the white light images. . . . .	41
3.9	The QPD response when a bead is off center in the optical trap is illustrated. .	44
3.10	A photo of the onion sample preparation for vesicle trapping. . . . .	45



3.11	The setup of the optical tweezers with fluorescence imaging using an UV laser source. . . . .	46
3.12	The ideal fluorescence (wide field) imaging integration with the optical tweezers setup. . . . .	46
3.13	The fluorescence spectrum of Rhodamine 6G dye (using excitation light of 405 nm). . . . .	47
3.14	Sample preparation of thin piece of leaf and a layer of onion stained Rhodamine 6G laser dye for fluorescence. . . . .	47
3.15	The setup for ptychography. . . . .	48
4.1	A trapped 1 $\mu\text{m}$ bead is moved with respect to the free beads in the sample. . . . .	49
4.2	An example of the position calibration. . . . .	50
4.3	The force constants in the trap determined using the equipartition method for beads 1 $\mu\text{m}$ in diameter. . . . .	51
4.4	The position of the bead fluctuating in the trap due to Brownian motion and the power spectrum of this motion. . . . .	52
4.5	The corner frequency is plotted for various trapping powers. . . . .	52
4.6	The force calibration is completed and the trap strength constant is plotted for various trapping powers (1 $\mu\text{m}$ beads). . . . .	53
4.7	The force calibration is completed and the trap strength constant is plotted for various trapping powers (4 $\mu\text{m}$ beads). . . . .	53
4.8	The force calibration is done on a 1 $\mu\text{m}$ bead at three different $z$ positions of the trap. . . . .	54
4.9	An image of an onion cell and identification of vesicles transported by molecular motors. . . . .	55
4.10	A white light image of a piece of leaf, and the same leaf imaged using the UV laser. . . . .	58
4.11	A white light image of a layer of onion stained with Rhodamine 6G, and imaged with fluorescence. . . . .	58
4.12	The sample to be reconstructed by the simulation is chosen as a light house image (for the amplitude) and an arrow image (for the phase). . . . .	59
4.13	The reconstructed amplitude and relative phase after 30 iterations of the PIE algorithm. . . . .	59
4.14	For different probe positions, different diffraction patterns are measured. . . . .	59
4.15	The images used as the sample's amplitude and relative phase, as well as the probe's amplitude and relative phase for the ePIE algorithm. . . . .	60
4.16	The probe estimate used in the PIE iterations, the reconstruction of the object in amplitude and relative phase after two PIE iterations. . . . .	61
4.17	The reconstructed object (in amplitude and phase), as well as the reconstructed probe after 350 ePIE iterations. . . . .	61
4.18	The difference function is plotted after two PIE and 350 ePIE iterations. . . . .	62
4.19	A cellulose acetate sample, to be reconstructed using PIE, is imaged using white light LED and CMOS camera in the ptychography setup. . . . .	63
4.20	After 100 PIE iterations, the associated amplitude and relative phase is reconstructed to image the cellulose acetate sample. . . . .	63
4.21	The reconstruction if no background is subtracted from the diffraction images. . . . .	65
4.22	The reconstruction if no pixel noise is subtracted from the diffraction images. . . . .	65
4.23	The reconstruction if the diffraction images are not zeropadded. . . . .	65
4.24	The reconstruction if no changes are made to the diffraction images. . . . .	65

# List of Tables

2.1	The ePIE updates the object and probe using the functions shown in this table.	28
3.1	The power in the trap is estimated by measuring the power before the objective.	38
3.2	The voltage-position calibration of the piezo drivers is shown here.	40
3.3	The average maximum pixel intensities are measured when one or multiple trapped beads are trapped.	42
3.4	The power is measured at the position of the QPD for various laser current settings.	43
4.1	The stall force for vesicles transported along predefined paths by molecular motors.	56

# Chapter 1

## Overview

Optical tweezing is a well established technique for spatial manipulation of a sample on a microscopic scale [4]. Optical tweezers apply forces (radiation pressure) on particles to trap them. In addition to trapping particles, the forces applied by the tweezers can also move the particles relative to their environment.

Single beam optical tweezing of a micron-sized, dielectric particle is possible by tightly focusing laser light to create a trap for a particle [5]. The tight focusing of the light causes a change in momentum of the light as it is refracted by the particle. This change in momentum imparts a force on the particle towards the focus - pushing the particle into the trap.

In this work, an optical tweezers setup is built and micron-sized particles are optically tweezed. The setup is characterized by determining the forces applied by the optical tweezers to trap a particle.

Since optical tweezers were introduced, they have been developed for various applications in the field of biology. *In vivo* optical tweezing is possible, because optical tweezers use continuous wave (cw) light with relatively low powers in the trap (25 mW to 500 mW), often using wavelengths between 700 nm and 1060 nm [9]. The size of the trap (focal region) and the magnitude of the forces that optical tweezers apply (picoNewtons), make optical tweezers well suited for studying cells [10; 11] with minimal damage to the samples [12]. A few applications of optical tweezers include: studying the stretching of DNA [13; 14, p. 372], studying cellular adhesion forces [15], assisting in cellular surgery [9], and investigating the use of vesicles as microreaction vessels [8]. It is also possible to study molecular motors using optical tweezers [16; 7]. In this work, the force required to stall a molecular motor's motion is investigated by trapping vesicles transported by the molecular motors in onion cells. This application of the optical tweezers demonstrates that the setup built can be used in a biological application.

In addition, the optical tweezers is set up such that it can be integrated into a multimodal microscope. Modalities of the multimodal microscope discussed in this work are multiphoton and nonlinear microscopy. These imaging techniques can include two photon fluorescence, second harmonic generation, third harmonic generation, and coherent anti-Stokes Raman spectroscopy. Multiphoton microscopy is inherently confocal, providing high resolution images [17].

The combination of the optical tweezers with a multimodal microscopy setup can provide better imaging of the trapped sample. Extra versatility is also added to the high resolution imaging setup, because the sample can now be tweezed. If, for example, a fluorophore is attached to a bead, the bead can be trapped using the optical tweezers. The position of the fluorophore can be manipulated, while stimulating a fluorescence

imaging signal in parallel. In this work, only preliminary fluorescence microscopy results are presented. Proposed modification of the setup for future work within a multimodal microscopy setup is discussed, including combining the microscope setup with a compressed super continuum excitation source [3].

Another microscopy technique looked at in this project is ptychography using an iterative ptychographic algorithm [18]. In ptychography, the amplitude and phase of light transmitted through a sample is reconstructed. This is achieved by illuminating sections of the sample and capturing the corresponding far field diffraction pattern. The intensity of the diffraction pattern is measured, but phase information about the sample is lost. With significant overlap between illumination spots on the sample, the results converge to a reconstructed relative phase corresponding to the sample. The ptychographic iterative engine (PIE) is an algorithm that uses the above mentioned measured far field diffraction patterns and iteratively implements the ptychographic reconstruction process [19]. The resolution of ptychography is limited by the angular spectrum, which is limited by the detection system.

By recovering the relative phase of the transmitted light through ptychography, phase contrast imaging is possible. This is useful in biological studies to image transparent samples and study mitosis, apoptosis, and cellular differentiation [20], for example. In addition to providing high contrast images, ptychography is a form of label free imaging. In microscopy, label free imaging is preferred over imaging that makes use of fluorescent markers, which could influence the cell and cell's environment. However, to image a dynamic system using ptychography is not trivial. The probe must scan the entire structure faster than the dynamics of the sample evolves.

In this work, components of an integrated optical tweezers and multimodal microscopy setup will be looked at. Each will be considered as separate entities, with the idea that in future work they can be incorporated into a multimodal system. The main focus of this work is the construction, characterization, and implementation of the optical tweezers.

**Thesis structure** The structure of this thesis is as follows. Chapter 2 gives a theoretical background of multiphoton microscopy and optical tweezers. It provides the technical details required for characterizing the optical tweezers and applying the optical tweezers to determine the stall forces of molecular motors. A theoretical description of ptychography is also discussed. Chapter 3 contains the setup of the optical tweezers, fluorescence microscopy, and ptychography. Following this, the results of this work are shown and discussed in chapter 4. Chapter 5 is the concluding chapter, containing a summary of the work.

## Chapter 2

# Background and theory

This chapter will introduce the concepts and techniques, as well as describe the theoretical background of the topics covered. It will start with an overview of different high resolution imaging techniques, then describe optical tweezing and the accompanying background theory in detail. This is followed by applications of optical tweezing. Finally, another imaging technique (ptychography), will be discussed.

### 2.1 Multiphoton microscopy

The multiphoton microscopy (MPM) technique has a resolution comparable, and slightly better, to that of confocal laser scanning microscopy with a resolution of 180 nm to 250 nm in the lateral plane [17]. The term multiphoton refers to the absorption of multiple photons and emission of one photon with a higher energy and consequently shorter wavelength than the originally absorbed photons. Examples of this is two photon fluorescence (TPF) or three photon fluorescence.

**Two Photon Fluorescence** Two photon fluorescence was carried out in a laser scanning microscope by Denk, Strickler and Webb [21]. For two photon fluorescence occurring in a material which can fluoresce, as depicted in figure 2.1 (b), two photons of equal energy are absorbed simultaneously, in a process called two photon absorption (TPA). There is a nonradiative decay that occurs to the lowest vibrational energy level of the electronic states [22]. One photon is emitted as fluorescence. The emitted photon has a higher energy than the initial incoming photons. Because the wavelength of the emitted photon is different to the incoming (excitation) light, the detection is made simpler by filtering out the excitation light and only detecting the emitted light.

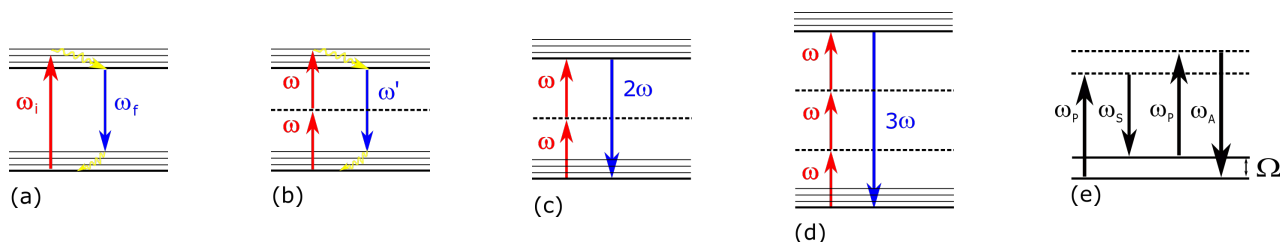


**Figure 2.1:** The Jablonski diagrams of linear and nonlinear processes are shown: (a) linear fluorescence, (b) two photon fluorescence (TPF), (c) second harmonic generation (SHG), (d) third harmonic generation (THG), and (e) coherent anti-Stokes Raman spectroscopy (CARS).

In contrast to two photon fluorescence, figure 2.1 (a) shows the process of linear fluorescence, due to one photon absorption, also used for imaging. This occurs naturally in some biological samples such as chlorophyll which fluoresces under ultraviolet (UV) light. In fluorescence microscopy, only one photon is absorbed and one photon emitted again. The probability of this occurring depends linearly on the incident intensity. This linear process has a probability to occur over the entire illuminated region which causes light to be detected from a large area, details of the sample to be smeared out and imaging resolution to be lowered. However, the advantage of two photon fluorescence over linear fluorescence microscopy is that in two photon fluorescence, the two photon absorption will only occur in the region where the intensity is sufficient due to the nonlinear dependence of the two photon fluorescence signal on the incident light intensity. This is limited to a smaller region - the focal area.

The effect of the above is shown in figure 2.2. Zipfel, Williams, and Webb [1] display the contrast between fluorescence induced by one photon, or two photons. The region from which the nonlinear signal of the two photon fluorescence occurs is localized to a smaller region than the linear fluorescence.

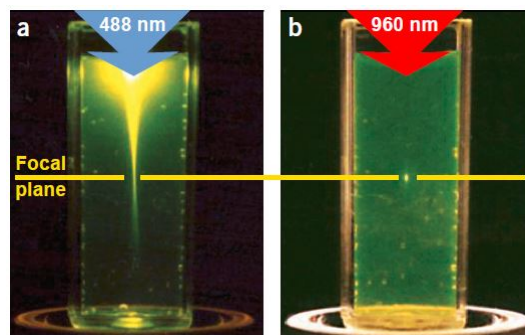


**Figure 2.2:** On the left, linear fluorescence is shown to occur throughout a large region of the beam waist ( $\lambda = 488$  nm, NA of 0.16). On the right, two photon absorption fluorescence is shown to occur in a relatively much smaller region ( $\lambda = 960$  nm, NA of 0.16). The figure is taken from [1].

In addition, the wavelength of the emitted photon in linear fluorescence is closer in range to the wavelength of the excitation photon, (because only one photon was used for excitation and the energy of the photon matches that of the energy gap). This property of linear fluorescence makes filtering the emission spectrum more complicated than in two photon absorption, where the difference in wavelength is larger. In two photon fluorescence, the wavelength of the emitted photon is approximately double that of the incoming, excitation light. This makes detection simpler by filtering out the excitation light and only detecting the emitted light as done by Xu and Webb [23].

Two photon fluorescence is a nonlinear process, due to the fact that the rate at which it occurs depends on the square of the excitation intensity, (because of the requirement of two photons to be absorbed simultaneously) [23]. The rate of two photon absorption is dependent on the square of the incident light's intensity and the cross section of two photon absorption [2, p. 141]. This nonlinear dependence of the rate of two photon fluorescence occurring is the reason this case of MPM is also referred to as nonlinear microscopy.

To create localized regions of high intensities, the laser is focused to as close as possible to the theoretical diffraction limit with a high numerical aperture microscope ob-

jective lens. The two photon absorption, and consequently two photon fluorescence, signal detected from outside the focus of the laser is far less than in the focus due to its nonlinear dependence on the excitation light intensity. This produces a localized three dimensional region, from which the MPM signal originates [1].

MPM can be expanded from two photon fluorescence to include other nonlinear optical processes such as second harmonic generation (SHG), third harmonic generation (THG), and coherent anti-Stokes Raman spectroscopy (CARS).

The above mentioned nonlinear processes follow directly from the extended medium polarization described as [24, p. 2]:

$$P(t) = \epsilon_0\chi E(t) + \epsilon_0\chi^{(2)}E(t)^2 + \epsilon_0\chi^{(3)}E(t)^3 + \dots \quad (2.1)$$

Here,  $P(t)$  describes the polarization of the medium in terms of the strength of the incident electric field,  $E(t)$ . This is done by the summing over all of the contributions from the first order of the electric field to higher orders. Each term is weighted by the susceptibility of the medium,  $\chi^n$  (a property of the material).

**Second Harmonic Generation** In second harmonic generation, two photons interact in the material to produce an emitted photon with energy equal to the sum of the incident photons' energy (figure 2.1 (c)). However, the material must have noncentrosymmetric properties for SHG to occur. In other words,  $\chi^{(2)} \neq 0$ . Light interacting with a material polarizes it and the second order susceptibility term in equation (2.1) is responsible for SHG [2, p. 154].

The SHG radiation produced by the polarized dipole is directional and mainly along the beam propagation direction [2, p. 407]. The fact that the second harmonic signal is coherent, causes a stronger signal emitted than the incoherent emission signal from two photon fluorescence with no preferred direction. However, the forward preference also makes the SHG signal weaker for epi-detection.

As in two photon fluorescence, the rate of this process is quadratically dependent on the excitation intensity, making it a nonlinear process [2, p. 379]. Because two photon fluorescence and SHG signals both depend quadratically on the incident light's intensity, they both have the same spatial resolution. These two techniques can be exploited by using them simultaneously as shown by Masters and So [2, p. 363] in figure 2.3. The figure shows the same sample, a hippocampal slice culture sample (50  $\mu\text{m}$  thick) labeled with a stilbene derivative, imaged simultaneously with two photon fluorescence above and SHG below. Using the two techniques can highlight different properties of the sample.

As mentioned above, SHG only occurs in noncentrosymmetric media. This is the advantage of SHG imaging. Imaging using SHG can be used to specifically target non-centrosymmetric structures in the sample, such as collagen [25].

**Third Harmonic Generation** Using the fact that a material has a non-zero third order susceptibility,  $\chi^{(3)} \neq 0$  in equation (2.1), third harmonic generation (THG) is possible (third harmonic generation can occur in centro- and noncentrosymmetric materials) [26]. Materials that are centrosymmetric and cannot be imaged using second harmonic generation, can be imaged using third harmonic generation. This is due to the key fact that third harmonic generation depends on the third order nonlinear susceptibility of the material. However, higher intensities are needed as this is a third order process. Three photons must therefore interact simultaneously, the probability of which will increase if the number of photons present increases, (scales with  $I_0^3$ , where  $I_0$  is the incident intensity).

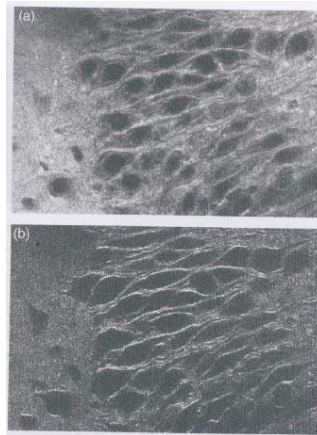


**Figure 2.3:** An image of hippocampal slice culture sample ( $50 \mu\text{m}$  thick) labeled with a stilbene derivative is taken from [2, p. 363]. The sample was imaged simultaneously with two photon fluorescence above and SHG below.

Third harmonic generation occurs when three photons interact simultaneously in the material and one photon with the sum of the energy of the three individual photons is emitted (figure 2.1 (d)). The dependence of the rate at which the process occurs on the intensity of the incident light is to the third order, implying that it is a nonlinear process. Comparatively, in cases where intensity is lower, third harmonic generation is less likely to occur than second order processes, such as two photon fluorescence or second harmonic generation. Higher intensities are needed for three photons to interact simultaneously and produce a significant third harmonic generation signal.

In third harmonic generation and second harmonic generation microscopy there is the added benefit that, because the photons are not absorbed, but only interact in the material (parametric processes), there is a reduction in the risk of photodamage to the sample. The wavelength of the emitted photon is the exact sum of the two or three photons that interact and no energy is deposited in the sample.

**CARS** Coherent anti-Stokes Raman Spectroscopy (CARS) is another third order nonlinear technique applied in spectroscopy and microscopy. It probes the molecular vibrations of a sample and yields spectroscopic information about the sample.

A pump beam,  $\omega_p$ , and a Stokes beam,  $\omega_s$ , interact to produce an anti-Stokes photon. The difference in frequency creates a beat frequency between the pump and Stokes photon,  $\Omega = \omega_p - \omega_s$ , and is tuned such that it matches the frequency of a molecular vibrational mode in the sample [2, p. 87]. This vibrational mode is consequently driven by the beat frequency, and the molecule oscillates. A probe beam is used to excite from the excited vibrational level and a coherent anti-Stokes signal is emitted,  $\omega_A$ , and detected as the CARS signal. The four wave mixing process is shown in figure 2.1 (e). Three incident photons are needed. The pump photon excites to a virtual level and the Stokes photon again de-excites to a excited vibrational state. A second pump photon excites to a second virtual level and the de-excitation of that state is measured as the anti-Stokes photon emitted.

CARS is a nonlinear process that depends quadratically on the third order susceptibility of the sample, quadratically on the pump beam intensity, and linearly on the Stokes beam [2, p. 172],

$$I_{CARS} \propto 9|\chi^{(3)}|^2 I_p^2 I_s. \quad (2.2)$$



Because of this non-linearity of incident intensity, the CARS signal is only generated in the small focal region where the probability for multiple photons to interact is large enough, and this provides the high resolution imaging capabilities.

As mentioned above, the nonlinear signal of these microscopy techniques is localized to a high spatial resolution region. Detection of the nonlinear signal is measured from various positions on the sample using a (raster) scanning technique. A two dimensional array of, for example fluorescent, signals is detected and an image constructed in this way.

**The source of the high intensities** To produce localized high intensities for stimulating nonlinear processes, short pulses of high peak intensities are required. This can be achieved by using, for example, a Ti:Sapphire femtosecond laser. The focusing of a compressed Ti:Sapphire femtosecond laser pulse implies that the intensities are only present for short bursts at a time. In other words, with short pulses of high intensities, the sample is exposed to low average power with low energy deposition into the sample. The spatial localization and short pulses reduces the risks of photodamage to the sample. Regions outside the highly localized focus are also not at risk of photodamage [1].

For MPM, the aim is to utilize near transform limited (TL) pulses. A transform limited pulse is the shortest pulse possible associated with a specific spectral bandwidth, with no chirp on the pulse. These short pulses ensure that while scanning the sample, the time during which energy is deposited at each point on the sample is minimized - reducing the risk of photodamage. Also, the short pulses ensure the necessary intensities needed to stimulate nonlinear processes to image the sample.

The femtosecond pulses from the Ti:Sapphire laser are made even shorter, into the near transform limited pulses. This is done through generating a supercontinuum by sending Ti:Sapphire femtosecond pulses through an ANDi-PCF (All Normal Dispersion - Photonic Crystal Fiber). Sending the pulses from the laser through the ANDi-PCF increases the spectral bandwidth due to the nonlinear processes occurring in the fiber, such as self phase modulation [27]. The supercontinuum is coherent, which implies that the spectral components are ordered in time and allows for pulse compression by phase modulation.

The spectrally broadened pulse is compressed in time using a Multiphoton Intrapulse Interference Phase Scan (MIIPS) algorithm to compensate for dispersion in the pulse [28]. By performing this phase modulation and compressing the pulses in time - increasing the peak intensities - the probability of the nonlinear processes occurring is increased.

Additionally to phase shaping, it is also possible to perform amplitude shaping [3]. This allows a section of the supercontinuum to be selected and compressed. In doing so, a specific range of wavelengths are chosen as an excitation source. Amplitude shaping reduces the number of photons, therefore also reducing the potential photodamage to the sample. If, however, the full bandwidth supercontinuum is compressed to obtain shorter pulses, a range of excitation wavelengths are used. In this case, the light emitted by the sample can be sent through an optical wavelength filter to distinguish between different wavelengths and nonlinear processes occurring in the sample.

**Multimodal microscopy in literature** The near transform limited pulses are focused by a high numerical aperture microscope objective lens onto the sample. The nonlinear signal can subsequently be detected using a scanning technique.

By implementing pulse shaping, a significant improvement in the nonlinear signal was observed by Liu, Tu, Benalcazar, Chaney, and Boppart [3]. They showed a mul-

timodal microscopy setup integrating two photon fluorescence, SHG and THG imaging techniques. In figure 2.4, the advantage of employing pulse shaping, mentioned above, is shown on imaging porcine skin taken from the paper by Liu, Tu, Benalcazar, Chaney, and Boppart [3]. The contrast of the image obtained using a compressed pulse is much greater than the image captured using an uncompressed pulse. The colours indicate the sample imaged with two photon fluorescence in red, second harmonic generation in green, and third harmonic generation in blue. The figure 2.4 was imaged with a compressed pulse above, and below with a uncompressed pulse. In this paper, they discuss the improvement in images by using a compressed pulse. The nonlinear signals are greatly enhanced by using a compressed pulse. The paper also demonstrates the integration of the three nonlinear imaging techniques to image the same sample.

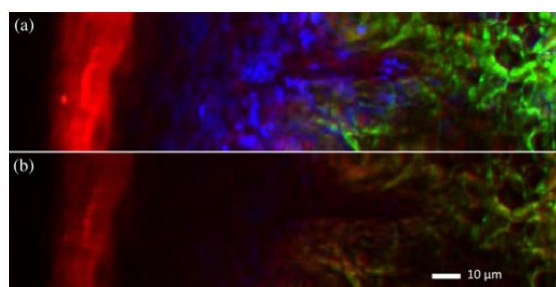


**Figure 2.4:** Image taken from the paper [3]. Liu, Tu, Benalcazar, Chaney, and Boppart discuss porcine skin imaged using two photon fluorescence (red), second harmonic generation (green) and third harmonic generation (blue). The image above was captured using a compressed pulse, while the image below with an uncompressed pulse. The improvement in contrast by using a compressed pulse is clearly visible.

In addition, CARS can also be integrated into a multimodal microscopy setup. CARS would provide the additional spectral information about the vibrational levels of the molecule. Liu, King, Tu, Zhao and Boppart [29] demonstrate CARS vibrational spectroscopy with an ANDi-nonlinear fiber and objective lens.

In contrast to confocal microscopy, where light is captured only from a small section of the larger sample area that is illuminated (by using for example a pinhole to block light), in nonlinear microscopy, the light detected from a localized region is the only light emitted. Nonlinear microscopy is inherently confocal and similar to a confocal microscopy setup, the sample is scanned and at each position, data is recorded building up an image. However, nonlinear microscopy is advantageous over confocal microscopy, because the scattered light from other regions outside the small excited region in confocal microscopy can reduce the resolution of the image [1].

According to Zipfel, Williams and Webb [1], MPM can image samples to the depth of hundreds of microns. The issue with imaging thicker samples, is not necessarily the stimulation of the nonlinear signal. Rather, the difficulty lies in detecting the nonlinear signal. Scattering and absorption of the nonlinear signal through the sample decreases the number of photons detected. This can also reduce the resolution of the images.

Combining different imaging modalities allow simultaneous use of various techniques to image one sample. Other modalities, such as optical coherence microscopy, have also been integrated into a multiphoton microscopy setup by Graf and Boppart [27]. The fact that multiphoton microscopy does not cause appreciable photodamage and is noninvasive

means that imaging can be performed several times, on the same sample area, to acquire data of the sample over longer time scales [27].

### **A combination of nonlinear imaging with optical tweezing in literature**

Previous studies have shown high resolution imaging and simultaneous optical tweezing is possible. For example Lang, Fordyce, Engh, Neuman, and Block [30] describe the setup of a single molecule fluorescence (SMF) microscope and optical tweezers. In this paper, they separate DNA strands and monitor the forces using optical tweezers while imaging the fluorescently labeled DNA molecules. Such a setup not only allows for high resolution imaging, but also for purposeful movement of parts of the sample, and measurements of structural properties of the sample using the optical tweezers. Another example of single molecule fluorescence measurements combined with optical tweezing is given by van Dijk, et al. [31].

Agate, Brown, Sibbett, and Dholakia [32] demonstrated optical tweezing with simultaneous two photon fluorescence using a femtosecond laser. By switching the laser between continuous wave and pulsed modes, the two photon fluorescence of the trapped particle can be turned on and off. Other spectroscopic optical traps have also been built, such as the setup used by Petrov [33] for Raman measurements on trapped samples.

The integration of nonlinear microscopy with the optical tweezers setup provides an additional degree of freedom to the setup. Spatial manipulation in the sample and other intracellular investigations are now also possible. The optical tweezers is explained in more detail in the following section.

## **2.2 Optical tweezers**

In this section, optical tweezing is discussed. In 1970, Ashkin [4] showed how light applying a force onto a particle, in the form of radiation pressure, can be used to optically trap particles. In this paper, he demonstrates that a beam of photons create a gradient force that can cause a particle located near the side, or edge, of the beam to be accelerated into the beam path. However, once in the beam, the particle travels in the direction of the beam and is not stably trapped. This is due to a scattering force that the photons apply to the particle.

In figure 2.5 there is a gradient force that causes the particle to move left, into the beam path. Because the particle, in this case a bead, has a higher index of refraction to the medium it is in, the incident ray is refracted as it enters and exits the particle. There is a change of momentum of the photons (entering and exiting the bead) to the right. This, due to conservation of momentum, causes the particle to experience a force to the left, into the beam path. This force has a component along the  $x$  axis that contributes to the gradient force shifting the particle to the left. The Gaussian beam creates a gradient force towards the highest intensity of the beam.

There also exists a scattering force that the particle experiences. This scattering force has a  $z$  component that pushes the bead in the direction of the beam. The combination of the gradient and scattering forces therefore cause the particle to be pulled into the beam path and accelerated in the direction of the beam.

This is an unstable trap, because the particle does not remain trapped in one known position. Ashkin [4] also showed that using two counter propagating beams one can form a very stable trap and could solve this problem, figure 2.6.

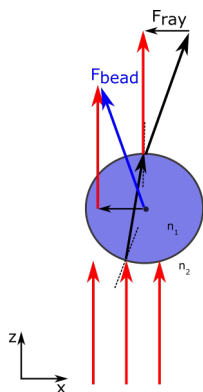


**Figure 2.5:** The particle in this figure is not in a stable trap. Radiation pressure forces will push the particle to the left, into the beam path, but then the particle will continue along the optical axis due to the scattering force [4].

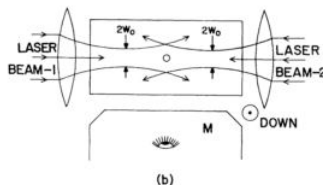


**Figure 2.6:** Using two counter propagating beams, a stable trap can be formed where scattering forces do not cause the particle to accelerate in the direction of the beam as shown by Ashkin. This figure is from [4].

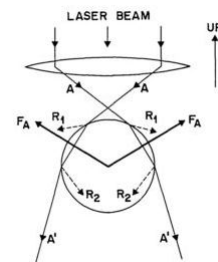


**Figure 2.7:** Ashkin, Dziedzic, Bjorkholm, and Chu showed that by focusing the laser, a trap is formed and the particle is trapped just after the focus of a beam. A single beam trapping ray diagram is shown from [5].

In 1986 Ashkin, Dziedzic, Bjorkholm, and Chu [5] showed another method of stable trapping using only a single beam. To overcome the scattering force causing the particle to accelerate along the optical axis ( $z$  axis in figure 2.5), a stable single beam trap is formed by using a sharply focused laser beam. The trap is then formed just after the focus, figure 2.7. The force due to the refraction of the rays and the scattering forces are in balance, such that the particle remains in one position, the so called trap position. By increasing the numerical aperture of the focusing lens, the beam is focused tighter and the scattering forces are dominated by gradient forces such that the trap position is stabilized near the focus of the beam. In figure 2.7, the force  $F_A$  due to refraction, accelerates the particle into the trap. This force balances out the scattering forces,  $R$ , that push the particle along the beam path.

**The geometric ray optics regime** In the section above, how a particle is trapped was described in terms of geometric ray optics and made use of the conservation of momentum. In the ray optics regime, the wavelength of the trapping laser is much less than the diameter of the particle. As mentioned above, a small portion of the photons are reflected and scattered, changing the direction of the particle in the opposite direction. The forces due to the scattering need to be smaller than the forces of the photons transmitted through the transparent particle.

The beam consists of photons with a momentum  $\vec{p}$ . As photons enter the particle they undergo a change in momentum (due to refraction). For conservation of momentum to hold, this change must be equal and opposite to the momentum gained by the particle. This force causes a shift of the particle towards the trap center and is the mechanism that causes the particle to become trapped. The same principle holds along the optical axis too.

Consider the forces on the particle perpendicular to the optical axis (along the  $x$  and  $y$  axes) as shown in figure 2.8. The focus is indicated by the black dot and the bold vectors imply higher number of photons. When the ray enters the particle, refraction

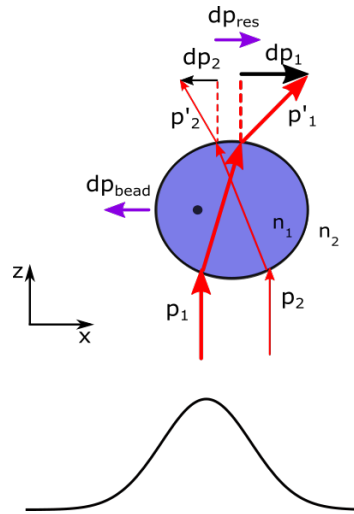


**Figure 2.8:** Trapping the particle near the focus of the beam for displacements of the bead to the sides of the focus is illustrated in the geometric ray optics regime. Conservation of momentum implies that the momentum change of the light due to refraction is the opposite momentum change that the particle undergoes. The focus is indicated by a the black dot.  $dp_{res}$  is the net change in momentum of the two light rays, and  $dp_{bead}$  is the equal and opposite change in momentum of the bead.

occurs and the direction of the ray changes slightly towards the normal due to the larger refractive index it encounters ( $n_1 > n_2$ ). When the ray exits the particle, the ray is refracted away from the normal as it moves to a medium with a smaller refractive index. When the ray changes direction, the momentum changes direction.

The change in momentum is directly proportional to the force the particle experiences. If there is a resultant change in momentum of the light beams to the right ( $dp_{res}$ ), as in figure 2.8, a force to the left is applied to the particle and it moves to the left (due to  $dp_{bead}$ ).

Assuming the beam has a Gaussian profile, as in figure 2.8, the intensity is larger in the center of the beam. Therefore, there are more photons to transfer momentum to the particle in the center. The force applied to the particle at the center of the beam is greater than the force applied by the photons in the outer parts of the beam. Therefore the particle is pushed to the center of the beam with a larger force and is trapped.

The forces that the rays of light exert on the particle can be decomposed into three sections. A ray is refracted as it enters and some of the light is reflected off the surface (the reflections contribute to the scattering force). As the light exits the particle, some of the light is not transmitted, but is reflected at the surface inside the particle. This ray then travels inside the particle again and the same occurs when it reaches the surface and wants to exit the particle. The light ray is reflected in the particle multiple times. However, the first reflection off the particle's outside surface and the first transmitted ray contribute to the majority of the forces. Each of these forces are proportional to the momentum of the light. As described by Jones, Marago, and Volpe [14, p. 24],

$$\vec{F} = N\vec{p}, \quad (2.3)$$

where  $N = \frac{P\lambda_0}{hc}$  is the number of photons per second incident on the particle and proportional to the power ( $P$ ). Therefore, if the intensity of the laser increases, the forces in the trap also increase.

The total force that the light ray in the geometric optics regime can exert can be described by a scattering and a gradient force. The gradient force dominates and keeps the particle in the trap position. The scattering force pushes the particle forward (causing the trap position to be slightly displaced from the focus of the beam [14, p. 34]).

Additionally, trapping the particle in the  $z$  direction, is based on the same momentum conservation principles as in figure 2.8. Before being trapped, the particle is either above or below the focus. The resultant force causes the particle to move either up or down such that the center of the particle is located at the trap position near the focus of the beam, and scattering forces are balanced by the net gradient force at that position.

**Rayleigh regime** If the diameter of the particle is much smaller than the wavelength of the light, the particle is modeled as an induced dipole, because the particle is too small to consider the effects of refraction [34]. This is called the Rayleigh regime. The laser, as an electromagnetic wave, induces an oscillating dipole in the particle. The force can again be broken up into two forces acting on the particle, a scattering and gradient force.

As before, incoming photons are scattered off the particle. Another way to see this is that the dipole absorbs a photon from the laser and emits it in a random direction. The emission causes a force in the direction opposite to the emission of the photon, but because there is no preferential direction, this force is averaged to zero. The absorption of the photon causes a recoil and force in the direction of the beam. This is the scattering force that pushes the particle along the beam path.

To counter the scattering force, again as in the geometric optics regime, there exists a gradient force. In the Rayleigh regime, the gradient force is due to the potential energy of a dipole in the electric field and is proportional to the gradient of the intensity of the incident light [14, p. 61]. If a Gaussian intensity profile of the beam is again assumed and the gradient applied to this intensity, the gradient force can be shown to be inversely proportional to the Gaussian beam waist and proportional to the maximum intensity. Therefore a sharper focus and higher intensities imply a stronger trap.

For the particles dealt with experimentally in this work, (of sizes on the order of micrometers) trapped by near infrared light, the geometric ray optics regime approach is applicable. According to Bechhoefer and Wilson [35], trapping is most effective if the wavelength is comparable to the size of particle. However, in that case, a more complex method is needed to find the solution.

The creation of a stable optical trap is dependent on the intensity of the light as explained above, the refractive index of the trapped particle with respect to the refractive index of its surroundings, and the numerical aperture (NA) of the focusing lens. The higher the numerical aperture of the lens used to focus the trapping laser is, the more stable the trap is.

A particle near the trap experiences a restoring force into the trap. In the next section, the trap strength will be looked at in more detail.

## 2.3 Characterization of the optical tweezers

To characterize the optical tweezers, the strength of the force that the trap exerts on particles will be determined. The force of the trap on a particle is proportional to the particle's displacement from the trap's center,  $F = -kx$  [36]. Here,  $k$  is a measure of the trap strength and the displacement is no larger than the particle's radius [14, p. 34]. Since

the force is the negative of the gradient of the potential energy, the potential energy of the trap can be expressed a parabolic function,  $E_p = \frac{1}{2}kx^2$ . The first order approximation is used here, because only small displacements from the trap center are considered. From this, one can see that if the trap strength increases ( $k$  increases), the corresponding parabolic function becomes narrower. Where as a weaker trap will yield a broader trap potential energy function.

The extent to which the particles can be trapped must be quantified to know what is the force exerted on the particles towards the trap center when they are displaced slightly out of the trap center. A particle displaced by a relatively small distance from the trap center can be approximated by a harmonic oscillator with a linear restoring force acting on the particle to pull it into back to the center of the trap. This restoring (trapping) force can be approximated by Hooke's law,  $F = -kx$ . The trapping force results as a consequence of radiation pressure acting in three dimensions thereby localizing the position of the trap in three dimensions.

Linear forces depending on the displacement,  $x$ , of the particle keep it in the center of the trap with a proportionality factor  $k$ . The strength of the trap is therefore quantified by the factor  $k$ . To determine  $k$  (the trap strength or stiffness constant) the equipartition theorem or a power spectral method can be used. Both of these methods rely on position sensing detection. Once the trap strength constant is known, the force on the particle in the trap can be determined relative to the particle's displacement from the trap.

It was said by Tlusty, Meller, and Bar-Ziv [37], that in the geometric ray optics limit with relatively small optical gradients (in other words, a weak focus), that the force is independent of the particle's radius. This was shown true for particles where the radius was bigger or equal to ten times the wavelength of the trapping light. In this work (using a strong focus), particles of radius  $0.5 \mu\text{m}$  and  $2 \mu\text{m}$  are trapped using a  $975 \text{ nm}$  laser, for example, this implies that the trapping force is dependent on the particle size. Note, that the drag coefficient used to determine the forces will also depend on the radius of the particle.

The forces of the trap depend on the sample properties, such as the particle size and the viscosity of the surrounding media. Therefore depending on the application of the tweezers, the forces must be calibrated using a sample with similar properties to that of the sample one wants to study. For example, to determine the forces of molecular motors on trapped vesicles in onion cells, silica beads of similar size as the vesicles placed in water is used as a sample for calibration.

### 2.3.1 Method 1: Equipartition theorem

The equipartition theorem states that the energy of the particle at thermal equilibrium and a single degree of freedom of the particle are related as follows,

$$\frac{1}{2}k_B T = \frac{1}{2}k_i \langle x_i^2(t) \rangle, \quad (2.4)$$

where  $k_B$  is the Boltzman factor,  $T$  is the temperature,  $k_i$  is the trap strength to be determined, and  $\langle x_i^2(t) \rangle$  is the average position of the particle over time. (The subscript  $i$  refers to the different degrees of freedom, for two coordinates, the equation will exist in both coordinates).

The temperature of the system is never zero. Therefore the energy is never zero. Due to Brownian motion, there will always be a statistical average displacement of the particle's position. This average variance in position can be measured and used to find

the trap constant,  $k$ , in equation (2.4) [38]. However, a more accurate and reliable method to determine of the trap stiffness is using the power spectrum [39].

### 2.3.2 Method 2: Power spectral density (PSD) method

The trap strength can be determined using the power spectral density method. As discussed in the previous section, due to Brownian motion, the particle's position will vary over time even when in the trap. In this section, the spectrum of the particle's variations in position will be used to determine the trap strength.

Brownian motion refers to the larger particle, which is in a fluid of smaller particles that constantly collide with the larger particle. For example, the larger particle could be a bead, and the smaller particles could be water molecules. This is a stochastic process and because of this, the average of these forces on the trapped bead over time, is zero. If there were no trap, this force would cause the bead to diffuse in the fluid. However, because of the trap, the bead is confined to a small spatial region.

Due to the stochastic force, the position of the bead will fluctuate rapidly over time in the trap. The position of the trapped bead can be measured with a quadrant position detector that gives the bead's position relative to the trap center as a voltage signal. The fluctuating position corresponds to a fluctuating voltage amplitude around a certain amplitude that is the trap center.

Brownian motion, from the environment that the bead is in, tries to displace the bead from its equilibrium position in the trap. The trap creates a potential to localize the bead in space and Brownian motion drives some oscillating motion of the bead with damping due to the viscosity of the fluid.

The motion of a particle in the optical trap, a bead for example in this explanation, is approximated by a damped harmonic oscillator that is driven by a stochastic force. It is described by the following Langevin equation:

$$m \frac{dx^2}{dt^2} = -\gamma \frac{dx}{dt} - kx + F(t). \quad (2.5)$$

Here,  $m$  is the mass of the bead,  $F(t)$  is the stochastic force due to Brownian motion,  $\gamma$  is the viscous drag coefficient, and  $k$  is the trap stiffness constant to be determined.

**The mass term** The inertial term that contains the mass ( $m \frac{dx^2}{dt^2}$ ) in the differential equation (2.5) can be neglected. This is because the viscosity of the medium (a function of the drag coefficient,  $\gamma$ ) in which the bead to be trapped exists, is very high. Because of the high viscosity of the medium, the viscous term ( $\gamma \frac{dx}{dt}$ ) dominates the inertial term.

Also, the correlation time of the stochastic force is much shorter than that of the motion of the trapped bead. The inertial motion of the trapped bead through the water is on a much longer time scale and therefore the inertial term can be neglected.

From equation (2.5), the relaxation time is  $\frac{\gamma}{k}$  [35]. This is much faster than the time scale of the trapped particle's inertial motion, the inertial term can thus be neglected [39].

After neglecting the mass term, the equation of motion equation (2.5) becomes

$$\frac{dx(t)}{dt} + \frac{k}{\gamma} x(t) = \frac{1}{\gamma} F(t) \quad (2.6)$$



**The damping term** The damping term in equation (2.5),  $\gamma \frac{dx(t)}{dt}$ , includes the viscous drag coefficient,  $\gamma$ . This is given by

$$\gamma = 6\pi\eta r \quad (2.7)$$

where  $r(= 2\mu m)$  is the radius of the particle (bead) and  $\eta$  is the viscosity of the fluid.

$\gamma$  is calculated by solving the hydrodynamic equation of motion for a small sphere far from the surface of the fluid. Equation (2.7) is the simple solution for Stokes drag [40]. This applies to a trapped particle (bead) too. When the bead is close to the surface there is a shear force (friction) between the bead and the surface that can also influence the drag on the bead.

The rigidity of the particle to be trapped also plays a role in the drag term. If the particle that experiences the drag is actually a different fluid droplet inside the solution, the surface tension of the droplet should be large enough such the droplet can be assumed rigid [41, p. 235].

In this work, it will be assumed that the particle to be trapped is under the correct conditions such that the drag coefficient can be chosen as  $\gamma = 6\pi\eta r$ . Any variations from the assumptions in biological samples, can cause an error in the measurements due to the assumptions mentioned above.

**The stochastic force in the trap and the frequency of the motion of the bead in the trap** The stochastic force due to Brownian motion is represented by  $F(t)$  in equations (2.5) and (2.6). Due to repeated collisions of the water molecules against the bead (in this explanation the particle in the trap is the bead), a stochastic force is exerted on the bead. Over a long time period, the average of the force caused by these collisions is zero.  $F(t)$  is an external force. Without  $F(t)$  the system would be largely over damped and decay to no oscillations, because the system is damped by the viscous drag.

A quadrant position detector (QPD) records the position of the trapped bead over time to measure the effect of  $F(t)$ . Over time, the stochastic force applied to the bead pushes the bead around in the trap due to Brownian motion. This causes the bead to be displaced and the amplitude measured by the quadrant position detector to fluctuate. However, as mentioned above, this measured amplitude averages to zero because of the stochastic nature of the force.

From a plot of the bead's position over time, a power spectrum (of a Lorentzian form) is generated by computing a discrete Fourier transform of the position signal (and squaring this). A power spectrum, in the frequency domain, displays the amplitude of the fluctuations of a certain frequency. It will be seen from the power spectrum that many frequencies are present in the trap at a nearly constant amplitude. However, above a certain "roll off" or "corner frequency" ( $f_c$ ), the amplitudes of the oscillations begin to decrease (as shown in figure 2.10 to follow). The corner frequency,  $f_c$ , is the highest frequency of motion of a bead in a specific trap that can be supported by the trap (the potential energy well). If the trap is very stiff, the bead can oscillate at very high frequencies in a more confined position (smaller displacements).

If the trap stiffness constant is large and the trap is strong, the spatial variations will be small, and the possible frequencies in the trap is higher than for a weaker trap. The stronger the forces in the trap, the steeper the gradient of the potential energy well created by the trap and the higher the frequency of the system.

**The power spectrum** In the following, the distribution of the power spectrum mentioned above (a Lorentzian function) is to be derived, similar to [35]. From this distribution, the trap stiffness can be determined and in turn, the force of the trap.

The variance in the displacement of the bead in the trap due to the stochastic force (what is measured experimentally) will be determined by solving the differential equation (2.6). Then this will be transformed to the frequency domain. The modulus squared of the variance in the frequency domain gives the Lorentzian distribution of the power spectrum. The final step will be to relate the correlation of the stochastic force with the temperature ( $T$ ), the viscous drag coefficient ( $\gamma$ ), and strength of the stochastic force ( $\lambda$ ) such that the power spectrum is in terms of these physical variables. From this power spectrum, the trap strength constant ( $k$ ) can then be determined.

It is through the corner frequency,  $f_c$ , that the trap stiffness,  $k$ , is connected to the power spectrum measured experimentally. The corner frequency must therefore be defined. The stochastic force correlation time (or relaxation time of the stochastic force) is  $\tau = \frac{\gamma}{k}$  from equation (2.6). Thus, the frequency is  $f_c = \frac{1}{2\pi\tau} = \frac{k}{2\pi\gamma}$  [42, p. 69]. Since  $f_c$  is where the power spectrum starts to decrease, one can determine  $f_c$  from the data, and from that find  $k$ .

*Remark.* The Fourier transform is taken as

$$\mathcal{F}\{F(t)\} = \tilde{F}(\omega) = \int_{-\infty}^{\infty} dt F(t) e^{-i\omega t} \quad (2.8)$$

(The tilde represents a Fourier transform)

Starting with equation (2.6), to solve for the variance in displacement in the frequency domain, the Fourier transform is applied to both sides of the equation. For simplicity, let  $\tilde{x}(\omega) = \mathcal{F}\{x(t)\}$ .

$$\begin{aligned} \mathcal{F}\{F(t)\} &= \mathcal{F}\left\{kx(t) + \gamma \frac{dx(t)}{dt}\right\} \\ \tilde{F}(\omega) &= \mathcal{F}\{kx(t)\} + \mathcal{F}\left\{\gamma \frac{dx(t)}{dt}\right\} \\ &= \tilde{x}(\omega) (k + i\omega\gamma) \end{aligned} \quad (2.9)$$

Let  $\omega = 2\pi f$  and using  $f_c = \frac{k}{2\pi\gamma}$ , equation (2.9) becomes

$$\tilde{F}(\omega) = \tilde{x}(\omega) (2\pi\gamma) (f_c + if) \quad (2.10)$$

Rewriting equation (2.10) so that the position in the frequency domain is be written as a function of the force:

$$\tilde{x}(\omega) = \frac{\tilde{F}(\omega)}{2\pi\gamma(f_c + if)}. \quad (2.11)$$

Taking the average square magnitude of  $\tilde{x}(\omega)$  gives the power spectrum in frequency space as

$$\begin{aligned} |\tilde{x}(\omega)|^2 &= \left| \frac{\tilde{F}(\omega)}{2\pi\gamma(f_c + if)} \right|^2 \\ &= \frac{|\tilde{F}(\omega)|^2}{4\pi^2\gamma^2(f_c^2 + f^2)} \end{aligned} \quad (2.12)$$

Now,  $|\tilde{F}(\omega)|^2$  in equation (2.12) - the variance in the external force in frequency, must be determined. Also, because of the stochastic nature of the force, an average over the stochastic force due to Brownian motion must be taken. To do this,  $|\tilde{F}(\omega)|^2$ , is inverse Fourier transformed to the time domain.

It is also assumed that the correlation function of the force in time decays to zero after a very short time interval. Water molecules, causing the Brownian motion of the trapped bead, collide with the bead for only a brief, finite, instance in time. These individual collisions are seen as instantaneous compared to the motion of the bead. The assumption is made that there is white noise in the system. To mathematically describe this white noise assumption, the following is said:

$$\langle F(t)F(t') \rangle = \lambda\delta(t - t') \quad (2.13)$$

where  $\lambda$  is defined as the strength of the random (stochastic) forces. The Dirac delta function in equation (2.13) is due to the fact that the random forces are applied on a very short time scale [35]. In other words, they are uncorrelated random kicks given to the trapped bead.

In the discrete case, equation (2.13) becomes

$$|\tilde{F}(\omega)|^2 = \lambda. \quad (2.14)$$

To determine the strength of the stochastic force,  $\lambda$ , the autocorrelation of the position of the particle in time is calculated,  $\langle x(t_1)x(t_2) \rangle$ . To do this,  $x(t)$  first needs to be found using the equation of motion (2.6),

$$\frac{dx(t)}{dt} = \frac{1}{\gamma}F(t) - \frac{k}{\gamma}x(t)$$

Using the integrating factor,  $e^{\int P(t)dt}$  where  $P(t) = \frac{k}{\gamma}$ , one finds that  $x(t)$  is given by

$$x(t) = e^{-\frac{kt}{\gamma}} \int_a^t e^{\frac{kt'}{\gamma}} \frac{F(t')}{\gamma} dt' \quad (2.15)$$

Now that  $x(t)$  is defined, the autocorrelation function of position in time at two points in time ( $t_1$  and  $t_2$ ), using equation (2.15) can be calculated. By substituting  $a = 0$  in equation (2.15), the autocorrelation is found as follows:

$$\begin{aligned} \langle x(t_1)x(t_2) \rangle &= \left\langle \left[ e^{-\frac{k}{\gamma}t_1} \int_0^{t_1} e^{\frac{kt'}{\gamma}} \frac{F(t')}{\gamma} dt' \right] \left[ e^{-\frac{k}{\gamma}t_2} \int_0^{t_2} e^{\frac{kt''}{\gamma}} \frac{F(t'')}{\gamma} dt'' \right] \right\rangle \\ &= \frac{1}{\gamma^2} e^{-\frac{k}{\gamma}(t_1+t_2)} \left\langle \int_0^{t_1} dt' e^{\frac{kt'}{\gamma}} F(t') \int_0^{t_2} dt'' e^{\frac{kt''}{\gamma}} F(t'') \right\rangle \\ &= \frac{1}{\gamma^2} e^{-\frac{k}{\gamma}(t_1+t_2)} \int_0^{t_1} dt' \int_0^{t_2} dt'' e^{(t'+t'')\left(\frac{k}{\gamma}\right)} \langle F(t')F(t'') \rangle \end{aligned}$$

Substituting equation (2.13):

$$\begin{aligned}
\langle x(t_1)x(t_2) \rangle &= \frac{1}{\gamma^2} e^{\frac{-k}{\gamma}(t_1+t_2)} \int_0^{t_1} dt' \int_0^{t_2} dt'' e^{(t'+t'')(\frac{k}{\gamma})} \lambda \delta(t' - t'') \\
&= \frac{\lambda}{\gamma^2} e^{\frac{-k}{\gamma}(t_1+t_2)} \int_0^{t_1} dt' e^{(2t')(\frac{k}{\gamma})} \\
&= \frac{\lambda}{2k\gamma} \left( e^{\frac{k}{\gamma}(t_1-t_2)} - e^{\frac{-k}{\gamma}(t_1+t_2)} \right)
\end{aligned} \tag{2.16}$$

Assuming long time scales, the first exponential term in brackets in equation (2.16) dominates and this simplifies to

$$\langle x(t_1)x(t_2) \rangle = \frac{\lambda}{2k\gamma} \left( e^{\frac{k}{\gamma}(t_1-t_2)} \right) \tag{2.17}$$

The strength of the stochastic forces,  $\lambda$ , in equation (2.17) can now be related to the temperature,  $T$ , of the surrounding medium of the trapped particle and to the drag coefficient,  $\gamma$ , by using the equipartition theorem, equation (2.18) below. Assuming equilibrium conditions implies,

$$\frac{1}{2} k \langle x^2 \rangle = \frac{N}{2} k_B T. \tag{2.18}$$

Although trapping occurs in three dimension, the measurement of the forces is done only in two dimensions. Therefore for the particle in the trap, there are two degrees of freedom corresponding to the two dimensions of the optical trapping plane perpendicular to the optical axis,  $N = 2$ . Therefore equation (2.18) becomes

$$\langle x(t)^2 \rangle = \frac{k_B T}{k}. \tag{2.19}$$

The variance in the particle's (bead's) position at a certain time, taken as  $t_1 = t_2 = t$ , is (using equation (2.17)),

$$\langle x(t)x(t) \rangle = \langle x(t)^2 \rangle = \frac{\lambda}{2k\gamma} \tag{2.20}$$

However, by equating the equipartition theorem in equation (2.19) and equation (2.20),  $\lambda$  can be written in terms of  $\gamma$  and  $T$ .

$$\begin{aligned}
\frac{2k_B T}{k} &= \frac{\lambda}{2\gamma k} \\
\lambda &= 4k_B T \gamma
\end{aligned} \tag{2.21}$$

The goal was to write equation (2.12) in terms of variables seen in the system, such as temperature ( $T$ ) and a drag coefficient ( $\gamma$ ). From equation (2.14),  $|\tilde{x}(\omega)|^2$  equals  $\lambda$ . Thus it follows, from equation (2.21), that

$$|\tilde{F}(\omega)|^2 = \lambda \tag{2.22}$$

$$= 4k_B T \gamma \tag{2.23}$$

This result shows that the strength of the stochastic forces ( $\lambda$ ), or the amplitude of the forces, does not depend on the mass of the trapped particle (bead) or the stiffness of the trap. The strength of the stochastic forces only depends on the viscosity of the

water and the size of the particle (bead) - as it is related to the drag coefficient,  $\gamma$ . This also stated by Howard in [42, p. 70].

Equation (2.12) can now be written as

$$\begin{aligned} |\tilde{x}(\omega)|^2 &= \frac{|\tilde{F}(\omega)|^2}{4\pi^2\gamma^2(f_c^2 + f^2)} \\ &= \frac{k_B T}{\pi^2\gamma(f_c^2 + f^2)} \end{aligned} \quad (2.24)$$

Equation (2.24) is be fitted to the power spectrum of the data recorded by measuring the position of the bead in the trap to determine  $k$ . This is the same as used by Gittes and Schmidt [40], after Fourier transforming the Langevin equation (2.6), taking the average of the square of the magnitude, and applying the white noise assumption.

Figure 2.9 shows how the fit to the power spectrum in (green), is a combination the following two (blue and orange) fits. The maximum amplitude of the power spectrum is shown in blue by the function

$$k_B T \pi^2 \gamma f_c^2, \quad (2.25)$$

where the constant corner frequency was  $f_c = 490$  Hz. If the system contains no trap and no damping, for a free particle, the corner frequency is zero. A fit for this case is shown in orange in figure 2.9 by

$$\frac{k_B T}{\pi^2 \gamma f^2}. \quad (2.26)$$

In the plots of figure 2.9, the temperature is 298 K, the viscosity is 1.012 mPa.s, and the radius of the particle is  $0.5 \mu\text{m}$ . The green curve is the combination of the two curves, equation (2.24). Where the amplitude starts to decrease is at the corner frequency of 490 Hz.

An example of how the function is expected to change for a stronger and weaker trap is shown in figure 2.10. Here, equation (2.24) is plotted with all variables kept constant as in figure 2.9, except the corner frequency,  $f_c$ . The corner frequency is changed from 50 Hz to 100 Hz, to 500 Hz. As the corner frequency increases, the point where the graph starts to decrease (roll off) shifts to higher frequencies and the amplitude of the initial constant segment decreases. For a certain trap strength, frequencies up to the corner frequency will be present at a constant amplitude. For stronger traps this frequency is higher than weaker ones.

From fitting the function in equation (2.24) to experimental data, the corner frequency is extracted.  $f$  in equation (2.24) is the frequency of the trapped particle's position fluctuations.

The Thorlabs OTKB software follows the procedure described above. The corner frequency,  $f_c = \frac{k}{2\pi\gamma}$ , can be extracted (where  $\gamma = 6\pi\eta r$  is the viscous drag coefficient) and  $k$  determined from the corner frequency. The software requires the diameter, temperature and fluid type (from which it determines the viscosity from an internal database).

Once the trap coefficient,  $k$ , is known the force that the trap exerts on the particle at various displacements from the trap can be calculated via Hooke's law,

$$F = -kx \quad (2.27)$$

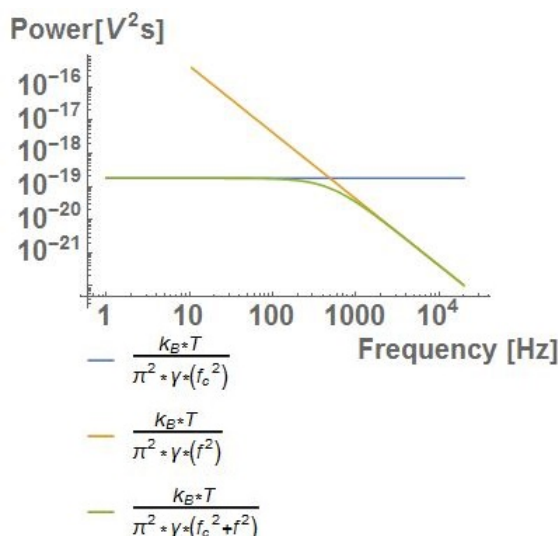


**Figure 2.9:** The power spectrum described by equation (2.24) is plotted. The blue curve shows the maximum amplitude of the trap. The orange curve considers a free bead, where there is no trapping force or damping acting on the system, and the corner frequency is zero. The green curve shows the combination of the blue and orange curves: the power spectrum to be fit for a particle in a trap. In this figure, the temperature is 298 K, the viscosity is 1.012 mPa.s, and the radius of the particle is 0.5  $\mu\text{m}$ .

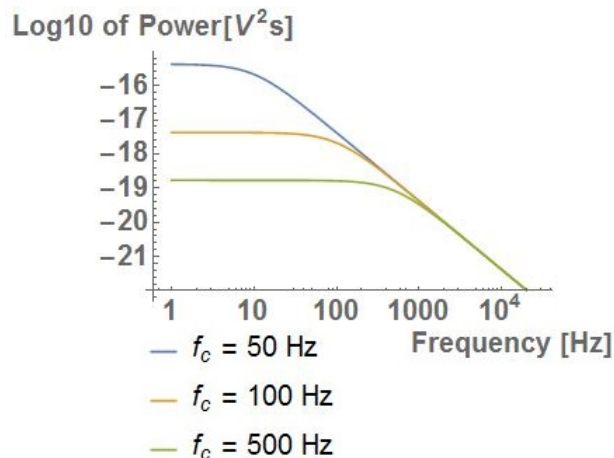


**Figure 2.10:** The power spectrum, equation (2.24), is plotted for different corner frequencies: 50 Hz (in blue), 100 Hz (in orange), and 500 Hz (in green). Physically, different corner frequencies would stem from different trap strengths (trapping powers). As the trap strength increases, the corner frequency shifts to higher frequencies and the amplitude decreases. In this figure, the temperature is 298 K, the viscosity is 1.012 mPa.s, and the radius of the particle is 0.5  $\mu\text{m}$ .

## 2.4 Applications of the optical tweezers

Since Ashkin introduced the idea of stable, single beam optical tweezing there have been many developments to apply this technique in fields such as microbiology, DNA studies [30], micro-machining [43], and micro-chemistry [8]. Some applications of optical traps and tweezers are described below.

### 2.4.1 Measuring the stall forces of molecular motors (Actin-Myosin motor proteins) in onion cells

An example of applying the optical tweezers to the study of biological samples is measuring the forces required to stall the motion of molecular motors. In this work, this is done using onion (*Allium cepa*) cells and measuring the stall forces of molecular motors transporting vesicles in the cells.

Onion cells are chosen because they are relatively large, onions are easily accessible, and transparent (a clear image can be formed using the transmission microscopy setup of the optical tweezers). The fluid in the cell is assumed to have similar viscosity to that of water. Also, since the vesicles are able to be trapped using the optical tweezers setup, it is assumed they have a refractive index higher than water (or their respective environment) to allow for stable trapping. The vesicle in the cell is therefore similar to that of the silica beads that is used in determining the trap strength and characterization of the trap.

The onion cells have a brick like shape. The cell walls surround the cytoplasm, also known as the cytosol of the cell. Inside the cytoplasm is the vacuole (storage space for the cell's contents) and the nucleus. The cytoskeleton forms part of the cytoplasm. The cytoskeleton consists of actin filaments and microtubules that give the cell its structure and form.

In a cell, molecular motor proteins facilitate the transport of cargo along predefined paths in the cytoskeleton of the cell: actin filaments and microtubules. Examples of such cargo are vesicles that are made of lipids joined together to form a spherical structure. The movement of the molecular motors along a predefined track in the cell allows for effective transportation of vesicles [44, p. 809].

The myosin molecular motor consists of a stalk with two heads on one end, attaching to the track, and a tail on the other end, holding the cargo. The vesicle (cargo), attached to the motor, moves forward as the motor steps forward on the track [45].

An example of myosin molecular motor proteins, is the myosin V motor. The myosin V motors move along intertwined and twisted actin-filaments. Actin-filaments are chain like and have a diameter of approximately 6 nm [42, p. 119].

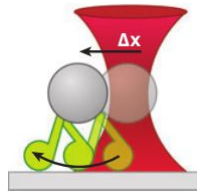


**Figure 2.11:** Molecular motors transport cargo along tracks in the cytoskeleton, such as actin filaments and microtubules [6].

A cartoon of a molecular motor transporting cargo along a cytoskeletal track is shown in figure 2.11 [6]. The motor is attached to the filament at its head, while the tail holds the cargo (in the figure this is a bead). Movement of the motor proteins can be described as a type of walking. The motors use energy from an ATP (Adenosine triphosphate) molecule to enable the motor to move [45]. The one head releases the track, the motor is bent forward, and the head attaches to the track again at a new position.

The mechanics and movement of the motors (the walking processes) has proven difficult to detect. Yildiz and Selvin [45] discuss two possible movement models for the myosin V motor: the hand-over-hand and inch-worm models. In both of these cases, the motor is never completely detached from the track (it is a processive motor). In the hand-over-hand motion, the heads pass each other in each step. In the inch-worm approach, one head always moves ahead of the other, the two heads do not pass each other.

The heads of the motors are small in comparison to the probes used to track their movement and therefore movement of the heads themselves is hard to track - one would need nanometer resolution. Yildiz and Selvin [45] used fluorescence imaging with one nanometer accuracy to show that myosin V and kinesin motors exhibit hand-over-hand movements (achieved by labeling one head with dye). It is therefore known that myosin V motors are displaced by this hand-over-hand motion. What is not yet well understood is how the environment gives the motor a preferential direction in which to move [46].

Myosin V motors are said to move with speeds up to  $0.4 \mu\text{m}$  per second [47]. On the other hand, the speed of myosin I and II motors ranges between  $0.04 \mu\text{m/s}$  and  $4.5 \mu\text{m/s}$  [44, p. 771]. However, these speeds mentioned are not measured in onion cells,

which have potentially different variables (such as viscosity or concentration of available ATP). The difference in such factors of the environment can effect the movement of the motors.

Another group of motors is the kinesin motor family. Kinesin motors travel along microtubules of the cytoskeleton, which have a pipe-like structure. When ATP is used, kinesin motors move along the microtubules, at speeds of up to  $0.8 \mu\text{m/s}$  [48].

An optical trapping laboratory guide of the MIT department of physics [49] describes the use of optical tweezers to measure the stall forces of actin-myosin motor proteins in onion cells. Using this reference, the molecular motors considered in this work is assumed to be myosin motors moving along actin filaments. Specifically it is the myosin V motor that transports vesicles [42, p. 215]. It is the vesicles that are imaged and trapped in this work, because the myosin V motors found in chick brains, for example, are approximately 31 nm in length [47] and due to the resolution of the setup used in this work, the motors themselves are not expected to be seen in the images.

The picoNewton forces [44, p. 771] that the molecular motors exert while transporting the vesicles along the filaments can be measured and analyzed using the optical tweezers setup. If the vesicle is released from the trap by decreasing the trap strength and it continues along the path, it is assumed that the vesicle is still attached to the motor. Therefore, it is the stall force of the motor that is measured, and not the force between the motor and the vesicle (in which case the vesicle would have been pulled off the motor).

## 2.4.2 Other applications of optical tweezers

In this work only the forces applied by molecular motors will be determined experimentally. However, other applications of the optical tweezers setup also exist. Two examples are discussed below: using the optical tweezers to measure the step size that the molecular motors take, and using vesicles as reaction vessels.

### 2.4.2.1 Measuring step size of molecular motors

Optical tweezers have been used to measure the step sizes of molecular motors. The step size and forces of myosin motors (the motor protein responsible for muscle contraction) were investigated by Finer, Simmons, and Spudich [7].

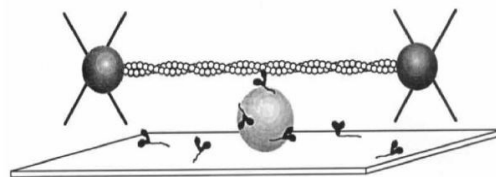


**Figure 2.12:** Molecular motor's step sizes are studied by Finer, Simmons, and Spudich [7]. A bead is fixed to a cover slide and covered with myosin motors. Two optical tweezers hold the ends of an actin filament attached to beads and move the filament into the vicinity of the motors. The displacement of the trapped beads are measured as an indication of the step size of the motors walking on the filament. The image is taken from [7].

A fixed bead on a cover slide was coated with myosin motors, figure 2.12. The two ends of an actin filament were attached to beads, and these two beads were trapped using two



optical tweezers. When the filament is brought near the fixed bead and myosin motors, the filament moves as the motors on the cover slide walk on it. This movement of the filament can be detected, because the position of the ends of the filament are measured using the optical tweezers. The displacements measured on the detector are  $11 \pm 2.4$  nm, which is said to be the step size of the myosin motor.

Myosin V, the motor protein responsible for vesicle transportation, was studied similarly by Mehta et al. [50]. Myosin V motors were scattered across a cover slide with fixed silica beads. The ends of an actin filament are secured to two polystyrene beads that are trapped in two optical tweezers. The filament is pulled tight putting tension on the filament. The positions of the polystyrene beads are measured. When the filament comes near the silica bead and myosin motors, the polystyrene beads move as the motors move along the filament.

#### 2.4.2.2 Using vesicles as reaction vessels

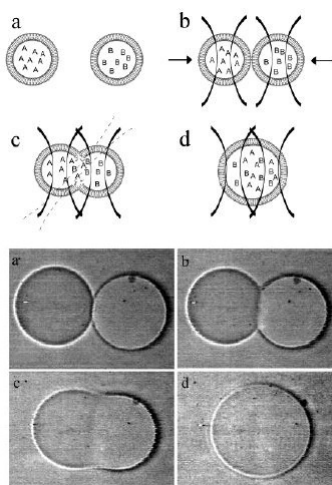


**Figure 2.13:** Optical tweezers are used to trap and bring two large vesicles into contact with each other. As shown by Kulin, Kishore, Helmerson and Locascio [8], two vesicles merge, their contents mix and can react.

Optical tweezers can be also be used to study the use of vesicles as microreaction vessels [14, p. 434]. For example, two vesicles can be fused and their contents can be mixed. Kulin, Kishore, Helmerson and Locascio [8] used two optical tweezers to bring two very large vesicles, with different contents, into contact. A third laser broke the lipid membrane of the vesicles and caused the vesicles to merge into one - mixing their contents. Figure 2.13 shows the process in steps (a) to (d).

## 2.5 Iterative ptychographic imaging algorithms

In this section, another well known imaging technique used in microscopy, ptychography, will be discussed. A ptychographic phase retrieval algorithm, Ptychographical Iterative Engine (PIE) [19], will be discussed as a technique used for imaging samples.

The advantage of ptychography is that amplitude as well as relative phase information is obtained from the sample. In the following, the reconstructed amplitude of the sample refers to the amount of light transmitted by the sample to the detector. The amplitude is

an indication of how much light was lost by absorption, reflection or scattering. The relative phase change that the light undergoes as a result of transmission through the sample, is referred to as the relative phase of associated with the sample. This relative phase holds information about the optical path that the light followed and thus information about the refractive index or physical depth of the sample.

The ptychographic iterative engine (PIE) is a phase retrieval algorithm for ptychography. By reconstructing phase associated with the sample, ptychography allows for phase contrast microscopy. For example, certain biological samples are transparent to visible wavelengths. They do not absorb the light and thus will not produce contrast in intensity (or amplitude) [18]. Samples that cannot be imaged with a high contrast using imaging techniques that only consider the amplitude of the electric field, can be better identified using their phase information. The spatial resolution of the image is limited by the theoretical diffraction limit, the wavelength of the light, and the size of the angular spectrum captured by the detector.

Ptychography is implemented by scanning a probe (a localized illumination beam) across the sample. The illumination spot of one probe position must overlap with that of the next - its neighbour. Diffraction patterns are recorded in the far field. Each diffraction pattern is a convolution of the probe amplitude and phase and sample's effect on the amplitude and phase at that probe position. The diffraction patterns are used in the iterative algorithm as input for the phase reconstruction algorithm. The phase is reconstructed by allowing the reconstruction of the phase to converge in the overlaps between neighbouring probe positions. Between two intensity distributions measured in the far field, theoretically, there exists one phase that is consistent with both intensity distributions [19].

### 2.5.1 The ptychographic iterative engine (PIE)

The PIE algorithm allows for imaging the object (or sample) by reconstructing the transmitted electric field after the sample. (The terms object and sample will be used interchangeably in the following.)

The probe is a localized illumination structure. It is a beam sent through a pinhole to "probe" a specific region of the sample. There are no restrictions on the wavefront of the probe, however, it must be localized on the sample and the probe's electric field must remain constant, [19]. For PIE, the full electric field description of the probe must be known.

The probe is scanned across the sample in object space. Object space refers to the sample plane, also referred to as real space. At each probe position a diffraction pattern is captured in the far field. The plane in which the diffraction patterns are recorded will be referred to as frequency space, since this is where the spatial frequencies are recorded. Each diffraction pattern is a convolution of the angular spectrum of the object and the probe. Each diffraction pattern is associated with a corresponding probe position in object space, with spatial coordinates. For example, figure 2.14 shows the sample (rectangular area), with circular probes at two positions in object space:  $A$  and  $B$ . One diffraction pattern will be recorded when the probe is at  $A$  and another at  $B$ .

Ptychography requires a certain degree of redundancy in the recorded data. This redundancy requirement exists because of the following argument. The images consist of pixels and there are  $N$  pixels in the image to be reconstructed. Each pixel corresponds to an equation. There are  $2N$  unknowns to be solved for (amplitude and phase) in each image. Therefore  $2N$  equations are needed in order to solve both the amplitude

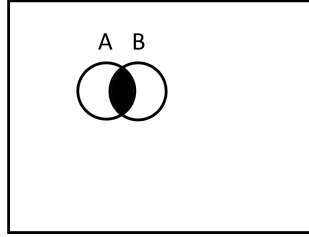


**Figure 2.14:** The probe (pinhole) is positioned over the sample in object space to select a circular region of the sample only. A diffraction pattern of this is recorded (in the far field). The diffraction pattern is a convolution of the probe and the sample. This is done at the various positions on the sample:  $A$ ,  $B$ , etc. As the probe is moved from one position,  $A$ , to a neighbouring position,  $B$ , there must be a significant overlap between neighbouring probe spots.

and phase. In one dimension this implies an overlap of probe positions of at least 50% is needed such that each pixel is imaged twice. The redundancy is achieved by having overlap between the illuminated spots of subsequent probe positions. According to Maiden and Rodenburg [51], the overlap between probe positions should be between 60% and 70%. The overlap constraint fulfills the redundancy requirement and allows the reconstruction to converge.

The diffraction patterns are recorded in the far field (Fraunhofer regime) such that the Fourier transform of the diffraction pattern is a good approximation of the object space at that position.

**The PIE algorithm** The PIE algorithm is described below as explained by Faulkner and Rodenburg [52].

1. Initially, the transmitted light's amplitude ( $E_{g,i}$ ) and phase ( $\phi_{g,i}$ ) are unknown in object space. For this reason, a matrix of zeroes or random values are used as an estimate (a guess) of the object's wave function,  $O_{g,i}(\vec{r})$ , in amplitude and phase. The subscript  $g$  refers to the fact that it is a guess and  $i$  refers to the  $i$ -th iteration of the algorithm. Since the matrix is two dimensional, the object has coordinates  $\vec{r} = (x, y)$ .

Also initiated is a complex valued probe function  $P(\vec{r} - \vec{R}_j)$ , (with amplitude and phase). A circular flat top function for the amplitude with no phase is chosen as a probe, for example. The probe and the object can be moved relative to each other, indicated with a two dimensional vector  $\vec{R}_j = (x_j, y_j)$  [19]. Here,  $j$  runs from one to the total number of probe spots needed to scan across the object, (with signification spatial overlap between neighbouring probe spots).

2. In object space, the object and the probe functions are multiplied with each other, to simulate light transmitted through a pinhole and the light then constrained to a region of a sample. For thin objects, this light has the following wave function when the probe is at a certain position relative to the object (in other words the pinhole lies over a certain part of the sample depending on probe position):

$$\begin{aligned}\psi_{g,i}(\vec{r}, \vec{R}_j) &= O_{g,i}P(\vec{r} - \vec{R}_j) \\ &= |\psi_{g,i}(\vec{r}, \vec{R}_j)|e^{i\phi_{g,i}(\vec{r}, \vec{R}_j)}\end{aligned}\quad (2.28)$$

The wave function above is written in terms of the amplitude and phase.

3. Equation (2.28) is Fourier transformed to spatial frequency space, creating a guessed diffraction pattern.

$$\begin{aligned}\Psi_{G,i}(\vec{r}, \vec{R}_j) &= \mathcal{F}\{\psi_{g,i}(\vec{r}, \vec{R}_j)\} \\ &= |\Psi_{G,i}(\vec{r}, \vec{R}_j)|e^{i\Theta_{G,i}(\vec{r}, \vec{R}_j)}\end{aligned}\quad (2.29)$$

where  $\vec{r} = (X, Y)$  is the spatial coordinates in frequency space corresponding to the Fourier transform of  $\vec{r} = (x, y)$ . And  $\Theta_{G,i}(\vec{r}, \vec{R}_j)$  is the phase in frequency space corresponding to  $\phi_{g,i}(\vec{r}, \vec{R}_j)$ .

Equation (2.29) consists of a guessed amplitude and phase wave functions, which are initially assumed as zeroes or random valued matrices.

4. However, at this probe position,  $\vec{R}_j$ , the diffraction pattern was experimentally recorded. The diffraction pattern contains the measured amplitude (square root of intensity measured) of the diffraction pattern wave function:  $|\Psi_{C,i}(\vec{r}, \vec{R}_j)|$ . The subscript  $C$  indicates that this is a measured, known wave function and not a guess. Replacing the amplitude in equation (2.29) above with this measured amplitude, corrects the guessed wave function's amplitude in frequency space. The phase is still unknown.

$$\Psi_{C,i}(\vec{r}, \vec{R}_j) = |\Psi_{C,i}(\vec{r}, \vec{R}_j)|e^{i\Theta_{G,i}(\vec{r}, \vec{R}_j)}\quad (2.30)$$

5. Computing the inverse Fourier transform of equation (2.30) yields an amplitude-corrected object at this probe position,  $\vec{R}_j$ ,

$$\psi_{c,i}(\vec{r}, \vec{R}_j) = \mathcal{F}^{-1}\{\Psi_{C,i}(\vec{r}, \vec{R}_j)\}\quad (2.31)$$

This wave function of the transmitted light now has a corrected amplitude (from what was measured), but still has a guessed phase to be determined.

6. To update the object ( $O_{g,i}$ ) at this probe position, an update function as well as an error function are calculated.

- a) The update function,  $U$ , is defined as

$$U = \frac{|P(\vec{r} - \vec{R}_j)|P^*(\vec{r} - \vec{R}_j)}{|P_{max}(\vec{r} - \vec{R}_j)|(|P(\vec{r} - \vec{R}_j)|^2 + \alpha)}.\quad (2.32)$$

In equation (2.32),  $\alpha$  is a constant variable that can be optimized for. It is chosen relatively small and exists to prevent a division by zero error occurring. The update function windows the function it is multiplied with to emphasize the part of the object covered by the probe, at this probe position.

- b) The error function is defined as the difference between the guessed wave function, with unknown amplitude, and the corrected wave function:

$$\vec{E}_i(\vec{r}, \vec{R}_j) = \psi_{c,i}(\vec{r}, \vec{R}_j) - \psi_{g,i}(\vec{r}, \vec{R}_j)\quad (2.33)$$

7. The object guess is updated using equations (2.32) and (2.33),

$$O_{g,i+1}(\vec{r}) = O_{g,i}(\vec{r}) + \beta U \vec{E}_i(\vec{r}, \vec{R}_j). \quad (2.34)$$

The object is only updated in the probe spot and nowhere else on the object, because of the windowing by the function  $U$ .

$\beta$  is a weighting factor between zero and one that can be optimized for. Generally,  $\beta$  is close to one. It weights the amount of feedback in the algorithm. If  $\beta$  is large, more emphasis is given to the previous guess. However, if  $\beta$  is small, more emphasis is given to the new guess [53].

The index  $i$  is increased, because at this position  $\vec{r}$  in object space, the object has a new wave function to be used in the next iteration of the algorithm.

8. The probe is now shifted to the next, neighbouring position on the sample,  $\vec{R}_{j+1}$ . As mentioned before, this next  $\vec{R}_{j+1}$  position must have a significant overlap to  $\vec{R}_j$  to fulfill the redundancy requirement. If the probe position is one where a neighbouring position has already been updated in this  $i^{\text{th}}$  iteration, the spot updating will have more updated-pixels than guessed-pixels to use when creating the virtual diffraction pattern (steps 2 and 3). For example, in figure 2.14  $B$  will contain updated information of the overlapping region with  $A$ .

Discrepancies between the position of the diffraction pattern recorded and that created by the algorithm, can cause the image to blur or create artifacts in the reconstructed image [51].

9. Once the probe has moved across the entire object, sample, to be imaged and  $j$  equals the number of probe spots used, the probe starts again at  $j = 1$ . The steps above, 2 to 8 are repeated iteratively while  $i$  increases.

After executing the algorithm iteratively multiple times, the reconstructed object wave form will no longer change significantly. The difference between  $O_{g,i}(\vec{r})$  and  $O_{g,i+1}(\vec{r})$  can be calculated [53] and if this is below a threshold value chosen, the PIE algorithm is ended. At this point in time, one could say that the object has converged to the reconstruction.

### 2.5.2 The extended Ptychographic Iterative Engine (ePIE)

The extended Ptychographic Iterative Engine (ePIE) is an extension to the PIE algorithm. As in the PIE algorithm in section 2.5.1, the probe is scanned across the object (sample) and the diffraction patterns are recorded on a detector in the far field. The difference is that in ePIE the strict requirement that the full description of the probe's electric field must be known is more relaxed. One only needs to have some idea of what the probe looks like as the probe is also reconstructed by the ePIE algorithm. This is useful when the probe's spatial and temporal profile is unknown. Although it is possible that an unknown probe can reconstruct the object, it can cause the algorithm to require more iterations. A guessed probe vastly different from the actual experimental probe used, will yield less accurate reconstructions [53].

**The ePIE algorithm** The ePIE algorithm is discussed here in the following section, similar to [51]. An initial guess for the probe is chosen at a position in object space relative

to the sample. For example, if the probe is unknown, an initial guess could be a flat top function of similar diameter.

The algorithm then follows the same procedure to the PIE. However, after the inverse Fourier transform in step 5, an additional update and error function (as defined for the PIE algorithm in the previous section) is defined for the probe wave function. The probe is then updated along with the object. The new functions are shown in table 2.1. The constants  $\beta$  and  $\gamma$  are chosen to weight the update and generally chosen close to one as in the PIE.

Object	Probe
$O_{i+1}(\vec{r}) = O_i(\vec{r}) + \beta U_{O,i} \vec{E}_i(\vec{r}, \vec{R}_j)$	$P_{i+1}(\vec{r}) = P_i(\vec{r}) + \gamma U_{P,i} \vec{E}_i(\vec{r}, \vec{R}_j)$
$U_{O,i} = \frac{ P(\vec{r}-\vec{R}) P^*(\vec{r}-\vec{R})}{ P_{max}(\vec{r}-\vec{R}) ( P(\vec{r}-\vec{R}) ^2+\alpha)}$	$U_{P,i} = \frac{ O(\vec{r}) O^*(\vec{r})}{ O_{max}(\vec{r}) ( O(\vec{r}) ^2+\alpha)}$
$\vec{E}_i(\vec{r}, \vec{R}_j) = \psi_{c,i}(\vec{r}, \vec{R}_j) - \psi_{g,i}(\vec{r}, \vec{R}_j)$	$\vec{E}_i(\vec{r}, \vec{R}_j) = \psi_{c,i}(\vec{r}, \vec{R}_j) - \psi_{g,i}(\vec{r}, \vec{R}_j)$

**Table 2.1:** The ePIE updates the object and probe using the functions shown in this table.

The probe continues to scan the sample multiple times (with significant overlap between neighbouring probe spots) and the guess wave functions are updated and converge to the amplitude and phase of the light transmitted by the sample.

Using this extension to the algorithm is useful when using a complex or unknown probe. This applies if, for example, the probe is Gaussian, but the PIE algorithm uses a flat top as a probe throughout the reconstruction. Using a more similar probe will allow the reconstruction of the sample in amplitude and phase to converge faster.

As mentioned in the previous section describing the PIE, while iterating through the algorithm, a difference function ( $\sigma$ ) can be calculated. This difference is defined as [53]

$$\sigma = \frac{\sum(|\Psi_{c,i}(\vec{r}, \vec{R}_j)|^2 - |\Psi_{g,i}(\vec{r}, \vec{R}_j)|^2)^2}{N} \quad (2.35)$$

where  $N$  is the number of pixels in the image. This value gives an absolute difference between images reconstructed in consecutive iterations. If  $\sigma$  is close to zero, it means that the images are not changing significantly any more and that the iterations can be terminated.

### 2.5.3 The resolution of imaging with ptychography

The resolution of an image reconstructed using the ptychography depends on two main factors. First, it depends on the wavelength of the illumination light. The wavelength defines the smallest possible resolution physically achievable with that wavelength. This image resolution is approximately half the wavelength. Second, the resolution depends on the quality of the angular spectrum captured. There are various physical factors that influence the angular spectrum of the light captured. These include the size of the detector's active region, pixel resolution of the detector, the dynamic range of the detector, and the noise in the diffraction patterns.

**The angular spectrum captured** The term angular spectrum is used to describe the diffraction pattern, because each point at which the intensity is measured on a screen represents an angle at which the waves propagated from the source to reach that point. Each point at the source radiates light radially outwards in all directions. It is assumed that the distance from the object to the detector is large enough that when the wavefronts reach the detector, they are no longer spherical, but flat - plane waves. At each point on the detector, the intensity measured is the sum of all the plane waves, from each point on a source, reaching that 'pixel'.

Referring to figure 2.15, the screen where the light (angular spectrum) is detected is shown by  $S$ . Each point on the source can be seen as a point on the source. The angular spectrum exists due to the fact that the waves originating at the source reach the detector at a specific angle. The light is propagating from left to right along the  $z$  axis (the screen is placed at a point  $z$  on this axis) and point  $P$  is a source emitting light in all directions ( $z = 0$  at  $P$ ) reaching the screen as plane waves.

At each point  $A$  on the screen, there exists a well defined direction of the ray, propagating from point  $P$  [54, p.442]. For each ray originating from a specific point on the source, there is a corresponding wave vector,  $\vec{k}$ , at each point  $A$ . The wave vector has an associated magnitude and directional cosines (as shown in figure 2.15 for  $a$ , similar holds for  $b$  and  $c$ ):

$$\vec{k} = \frac{2\pi}{\lambda}(a\hat{x} + b\hat{y} + c\hat{z}) \quad (2.36)$$

with  $\hat{\phantom{x}}$  indicating unit vectors.

Across the screen,  $U(x, y, z)$  is the function representing the interference pattern detected.  $U(x, y, z)$  is a composition (Fourier transform) of a collection of plane waves, all traveling in different directions with different wave vectors towards the screen. Because of this, each wave has its own directional cosines. Spatial frequencies are related to the projection of the wave vector on to the  $x$  (red in figure 2.15),  $y$  and  $z$  axes and to the directional cosines [54, p. 57].

The resolution of the reconstructed image, is determined by the size (the upper limit) of the angular spectrum (in frequency space) detected [19]. Higher frequencies correspond to sharper edges in object space. The sharpest edges of the sample will be captured in the higher frequency components (larger diffraction angles) of the diffraction pattern captured on the detector. Therefore the resolution is dependent on the detector's physical size.

Another way to explain is s by considering figure 2.16. Light transmits though a sample (at point  $P$ ) in the object plane ( $O$ ) and the diffraction pattern is captured on a screen at  $S$ . The point source ( $P$ ) emits light radially in all directions, but by the time the waves reach the frequency plane at  $S$ , the light is approximated by a plane wave with a flat wave front. These plane waves arrive at the screen at an angle  $a$ , as is shown in the figure. In the figure,  $d$  is the size of the active region of the detector.

Smaller features at point  $P$  cause diffraction at larger angles of  $a$  than if  $P$  had larger features. For example, a small slit has a larger, more spread out, diffraction pattern compared to a larger slit at the same propagation distance from the source. Therefore to resolve smaller features in the object plane, the detector at  $S$  would need a larger active region  $d$ . Or the detector must be brought closer to the object plane.

**Adding higher frequency components and the resulting resolution** Adding more contributions from higher orders of the diffraction pattern is the same as adding

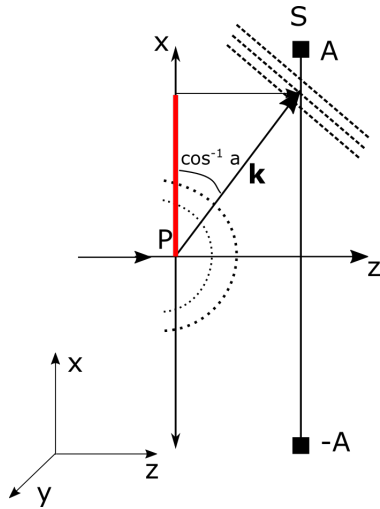


**Figure 2.15:** If  $P$  is a point on the source emitting spherical waves (dotted radial lines), the angular spectrum at the detector screen ( $S$ ) is an interference of plane waves (dotted lines), each with wave vector  $\vec{k}$ . These plane waves each propagate at a specific angle. These angles correspond to the different spatial frequencies ( $f_x$ ) of the spectrum.

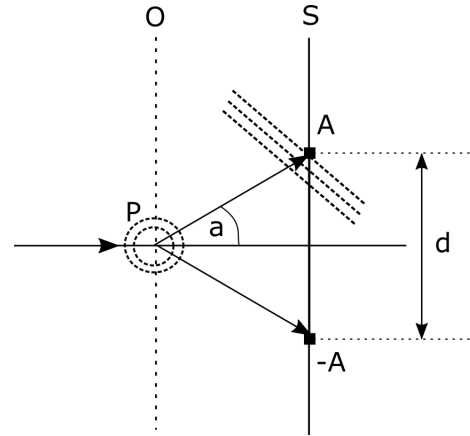


**Figure 2.16:** Light from a point  $P$  extends onto a screen  $S$ , forming the angular spectrum. The detector's outer pixels are shown by  $A$  and  $-A$  (along one dimension).

more frequencies to a Fourier series. A Fourier series becomes more accurate if higher order terms are also included. For example, if a square function is to be approximated by cosine waves of various frequencies, the more terms in the Fourier series are added, the better the approximation becomes.

If more spatial frequency components are added to the diffraction pattern measured, the period (resolution) in object space increases. If the period decreases in object space it means that finer structures are causing the interference. These smaller features can then be resolved due to the higher spatial frequencies detected. This is the core reason why it is necessary to detect the higher diffraction orders in ptychography.

The other limit to the resolution that the detector possibly imposes is through the pixel size. This will limit the size of the features that can be resolved in the reconstructed image.

**The detector's dynamic range** The dynamic range of the detector is an important factor in obtaining well reconstructed images [19]. The dynamic range of the detector refers to the ability of the detector to detect subtle changes in the intensity. For example, a 10 bit CMOS sensor will have a larger dynamic range than an 8 bit sensor.

The high peak intensity of the zeroth order in the diffraction pattern recorded, can cause subtle, but significant changes in the intensity of higher orders to be too small to detect. If the zeroth order could be reduced in intensity, the exposure time of the detector can be increased and the higher orders better resolved in intensity.

To remove the high peak intensity of the zeroth order of the diffraction pattern, a diffuser can be placed over the pinhole, as done by [18]. The intensity that would have been localized in the zeroth order of the airy pattern is now scattered into other orders. This, however, changes the probe. Due to the fact that no knowledge of the electric field distribution of the light through the diffuser is available, the ePIE algorithm is needed to



reconstruct the probe along with the sample. This was done by Maiden, Rodenburg, and Humphry [18] and proved to increase the dynamic range up to ten times.

**Noise in the images acquired** The resolution of the images obtained can also be influenced negatively if there is too much background noise or system noise in the experimentally measured diffraction patterns. The higher orders of the diffraction pattern have very low intensities, and so the higher orders are possibly hard to distinguish above the noise. Removing the noise should be done before the PIE or ePIE algorithm is implemented to improve the quality of the reconstruction.

While these factors (the wavelength of the light; detector's active region dimensions, pixel size, and dynamic range; as well as the noise in the images) influence the resolution, ptychographic imaging is not affected by the resolution limitations of the optical components, such as a lens.

By using a detector with a larger active region, dynamic range, and reducing the background noise, the resolution can be improved. The advantages of ptychography providing, not only information about the amplitude of the transmitted light, but also the relative phase associated with the sample, makes ptychography very useful for microscopy.

# Chapter 3

## Experimental setups

In this chapter, the experimental setups of the optical tweezers, integration of the optical tweezers with fluorescence microscopy, and the ptychography setup will be discussed.

### 3.1 Setup for the optical tweezers

A Thorlabs kit for Modular Tweezers, *Thorlabs OTKB(/M)*, was set up to trap micron sized particles using a 975 nm diode laser. A diagram of the setup can be seen on the left in figure 3.1, and an image of the laboratory setup to the right of the schematic.

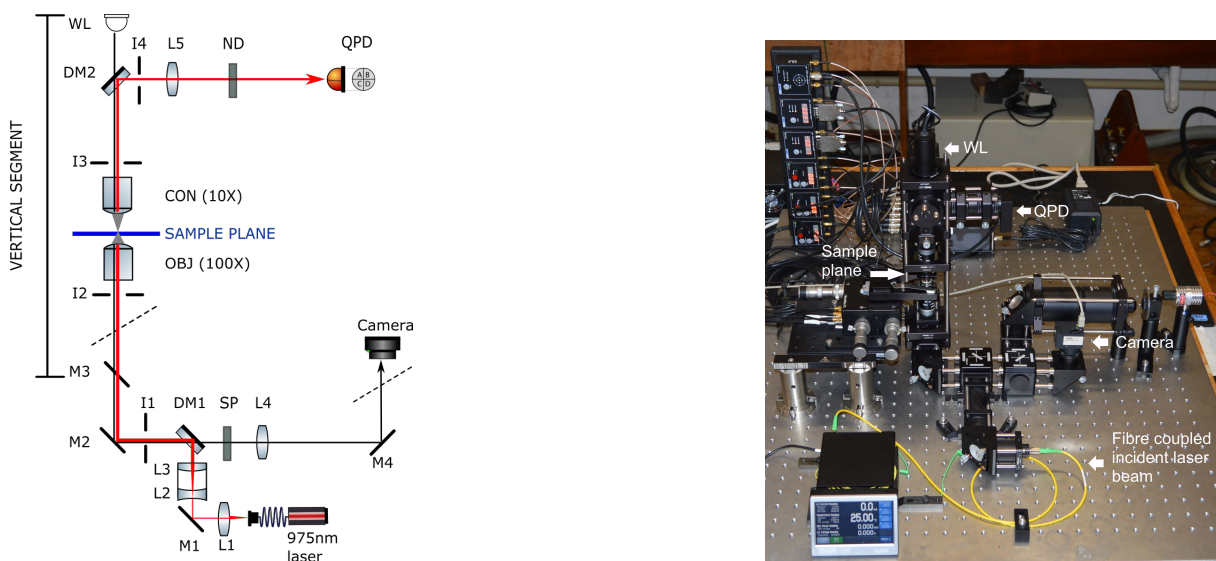


**Figure 3.1:** The figure on the left shows a schematic diagram of the optical tweezers setup and to the right is a photo taken of the experimental setup. The optical tweezers setup used to trap particles uses a 100X microscope objective to focus a 975 nm laser beam. The sample is placed on a translation stage (controlled by piezo drivers). The image of the sample can be viewed on a camera using a white light (WL) LED as an illumination source. A quadrant position detector (QPD) is included in the setup for trap force measurements as described in section 3.2.

A 975 nm, near infrared (NIR), diode laser (*Thorlabs Compact Laser Diode Controller, CLD101X*) is used in this optical tweezers setup. Shorter wavelengths focus to a smaller spatial region than longer wavelengths, but water absorbs light at shorter wavelengths and most biological samples consist of large percentages water [55, p. 152]. Therefore to

avoid the unintended absorption of light, one typically uses a source with a wavelength that falls outside of the sample's absorption window (in this case 975 nm).

The laser is coupled into a single mode fiber (*Thorlabs SM980 – 5.8 – 125*) with corresponding patch cord (*Thorlabs P3 – 980A – FC – 1*). The single mode fiber ensures that only the Gaussian mode  $TEM_{00}$  is transmitted to the setup, no other orders besides the  $TEM_{00}$  order are transmitted. Higher order spatial modes would influence the trap efficiency, because the beam would not be focused as tightly as when only a Gaussian mode is allowed [35]. A weaker focus would decrease the gradient force on particles near the trap, weakening the trap itself.

The numerical aperture (NA) defines the acceptance angle of the light coupled into the fiber, and the angle at which the light diverges when it leaves the fiber at the other end. In this way, the numerical aperture influences the lens chosen to collimate the light after it leaves the fiber. The fiber has a numerical aperture of 0.14.

From the fiber, the light enters a collimator (L1 in figure 3.1) with a focal length of 6.11 mm and NA of 0.28, to ensure that the light coupled out to the setup is collimated. In figure 3.1, the beam is reflected off mirror 1 (M1) to the beam expander (lenses L2 and L3) where the diameter of the beam waist is increased to fill the back aperture of the 100X objective lens. Optimal use is made of the objective lens by ensuring that the back aperture is completely filled. This is done by increasing the beam diameter, which causes a sharper focus through the objective lens. The (Galilean) beam expander consists of two achromatic doublet lenses. The first lens (*Thorlabs ACN254 – 050 – B*) has a focal length of  $-50$  mm. The second lens (*Thorlabs AC254 – 150 – B*) has a focal length of 150 mm, which collimates the beam again. The distance between the two lenses of the beam expander is adjusted to optimize the collimation. The light after the beam expander should be centered (accomplished by adjusting mirror 1) and collimated (such that it remains the same size over a distance of several centimeters).

The filter cube after the beam expander contains a shortpass dichroic mirror (DM1) (*Thorlabs DMSP805R*, with reflection at 975 nm is 99.8%, and transmission below 805 nm is above 50% - including white light). DM1 reflects the NIR beam to the 100X objective found in the vertical part of the cage assembly. This dichroic mirror has a cut off at 805 nm, which allows the visible illumination light (used to image the sample) to pass through to the camera. Iris 1 (I1) is used for alignment purposes only and is left open after alignment. Mirror 3 (M3) reflects the beam such that it now travels vertically upwards. Mirrors 2 (M2) and 3 (M3) are aligned using irises I1 and I2.

The vertical segment is held steady by securing it to the a vertical post (*Thorlabs DP14A*). Iris 3 (I3) is placed after the 10X objective. The two irises I2 and I3 are used for alignment of the vertical segment and are left open after alignment is completed.

After iris 2 (I2), the beam travels through a 100X oil immersion Nikon E-Plan objective lens. The 100X objective lens is used to create the sharp focus used to trap particles. The objective focuses the laser beam to a point less than half a millimeter from the objective lens, the lens has a working distance of 0.23 mm. Due to the short working distance, cover slides of 0.17 mm in thickness are recommended.

Microscope objective immersion oil is placed on the top of the objective as seen in figure 3.2. The oil reduces reflection losses. Also, there exists a mismatch in index of refraction of the objective lens, air, and cover slide,

$$n_{air} \approx 1; \quad n_{glass} \approx 1.5$$

This mismatch in index of refraction can result in spherical aberrations [56]. Oil (with  $n_{oil} \approx 1.5$ )

is added such that there is less of a difference between the index of refraction and the refraction of the light rays is less.

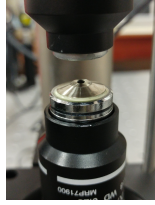


**Figure 3.2:** A drop of microscope objective oil is placed on the 100X oil immersion objective to decrease the mismatch in the numerical aperture between the objective lens and cover slide.

The 100X objective has a numerical aperture of 1.25. A higher numerical aperture implies a higher resolution. From  $NA = n \sin \theta$ , it follows that a higher NA means a larger  $\sin \theta$ , and so a larger angle  $\theta$ . If the angle is larger it means the angle from which light is captured is larger and that light is focused tighter. For a high intensity at the focus, a small Rayleigh range,  $z_R$ , is ideal. The Raleigh range and numerical aperture are related by  $z_R = \frac{w_0}{NA}$  where  $w_0$  is the spot radius at the focus. Therefore a large NA is ideal as it implies a short distance of highly focused light (spatially, it is highly localized). Theoretically, the spot size (diameter) created by the 100X microscope objective is [57]

$$\begin{aligned} D &= 1.22 \frac{\lambda}{NA} \\ &= 1.22 \frac{975 \times 10^{-9}}{1.25} \\ &= 952 \times 10^{-9} \text{m} \end{aligned}$$

This is not the exact trap size (as the trap is influenced by the gradient of the electric field), but a good approximation.

Above the sample is the condenser lens that is a 10X Nikon E-Plan objective, which has a working distance of 7 mm. This means that sample must be placed approximately 7 mm below the condenser lens. The condenser has a numerical aperture of 0.25. The condenser collimates the diverging NIR light transmitted by the sample such that the sample can be imaged (using an additional imaging lens) onto a quadrant position detector for further trap characterization. This will be explained in more detail in section 3.2.

The other purpose of the condenser is to illuminate the sample with the white light (WL). By moving the condenser up and down, one can also see the brightness of the sample on the camera change as the focus of the condenser is moved nearer or farther from the sample plane. If the bead is in the trap (focal plane of the trapping laser), it will also be in the focal plane of the imaging system.

The condenser can also be adjusted left and right on a  $xy$ -mount (*Thorlabs CXY1*). To ensure optimal alignment of the objective and condenser such that their focal spots centrally overlap, iris 3 above the condenser is closed and the power is measured above this iris. The  $xy$ -mount is adjusted until the power measured is maximal.

A shortpass dichroic mirror (DM2) reflects the 975 nm light away from the LED white light illumination source (WL in figure 3.1), to the quadrant position detector. DM2 is aligned such that the NIR light is used to image the particle's position relative to the trap onto the quadrant position detector.

The white light is used to image the sample onto a camera. The light from the LED is focused onto the sample by the condenser. The white light follows the same path as the NIR light, but in the opposite direction. It propagates down the vertical segment and to the filter cube containing the shortpass dichroic mirror (DM1). This mirror has a cutoff at 805 nm, meaning that the white light passes straight through the dichroic mirror, but any light of wavelengths more than 805 nm is reflected by the mirror. After the dichroic mirror, there is another shortpass filter with a cutoff at 750 nm (*Thorlabs FESH0750*, with a transmission of less than 1% at 975 nm and transmission of above 90% below 745 nm). This filter reflects the light from the light of wavelengths above 750 nm, preventing it from reaching the camera.

To image the sample, an 8 bit CMOS (Complementary Metal-Oxide-Semiconductor) sensor (*Thorlabs DCC1240C-HQ*, *USB 2.0 digital camera*) is used as a camera, with  $1280 \times 1024$  pixels, and a square pixel of size of  $5.3 \mu\text{m}$ . A CMOS sensor is a two dimensional array of photodiodes. Incident photons are absorbed and converted to an electronic signal. The voltage is related to the intensity of each pixel in the image on the screen [58, p. 119].

To create an image of the sample on the camera, a tube lens is placed before the camera (L4). Because the objective is infinity-corrected, in theory it does not matter where the lens is placed, it will focus collimated light at the focal point of the tube lens on to the camera. Before reaching the camera, the light is reflected vertically off another mirror (M4). This mirror is just for convenience, making it easier to reach the camera rather than having it parallel to the table in this setup.

In practice, however, the objective is not perfectly infinity-corrected. Therefore, to find the relative positions of the tube lens and camera, a bead is trapped and brought into focus by adjusting the distance between the tube lens and camera. Note that the beads stuck on the cover slide or an imaging grid slide should not be used since it can still be translated through the focus using the control of the  $z$  position of the stage. A trapped bead is suspended in water in the exact trap position. Moving the  $z$  position of the stage will not move the bead unless it is pulled down onto the slide or surface of the water. When the bead in the trap is in focus, the beads stuck on the cover slide will be out of focus, because they lie in different focal planes.

A biconvex lens (*Thorlabs LB1945*) with a focal length of 200 mm is used as a tube lens. As explained above, the lens is placed at the optimal imaging position from the 100X objective to create a sharp image on the camera.

The sample is placed on a NanoMax-TS (*Thorlabs MAX311D/M*) translation stage mounted on a (*Thorlabs TBB1515/M*) platform. The sample is held stationary in a sample holder that clamps the cover slide into a stable position. The stage can be moved in the  $x$ ,  $y$  and  $z$  plane by piezo controllers (*Thorlabs T-cube piezo controllers*, *TPZ001*). The controllers are connected to a T-cube USB 2.0 controller hub (*Thorlabs TCH002*). The piezos allow for very fine adjustments to the position in the order of submicrons. By applying a voltage to the piezos, they expand and translate the stage. The displacements by the piezos can be calibrated in order to know how far the stage moves for a given applied voltage. Using the ATP User software (*Thorlabs*, *version 3.3.5872.27953*) that controls the drivers, a voltage between 0 V and 75 V can be applied to the piezos. This allows for a maximum displacement of the stage of  $20 \mu\text{m}$ . The theoretical resolution of the piezo driver stage in open loop mode is 20 nm. While in closed loop mode, achieved by also including the the strain gauge controllers, the resolution is 5 nm.

### 3.1.1 Determining the pixel calibration

A microscope slide with a resolution grid printed on it (*Thorlabs grid distortion target R1LS3P*) is placed on the translation stage and moved into the focus of the objective and condenser. It is placed with the grid, printed on the surface of the 1.5 ( $\pm 0.2$ ) mm thick slide, towards the 100X objective. By adjusting the  $z$  component of the stage, the grid comes into focus as the slide comes into contact with the drop of oil on the objective.

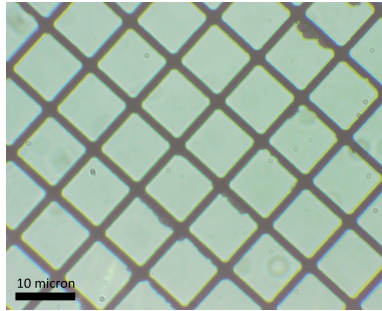


**Figure 3.3:** Imaging the 10  $\mu\text{m}$  spacing grid of the grid distortion target slide using the white light LED and camera in the optical tweezers setup.

The white LED light is used for this imaging. The 10  $\mu\text{m}$  spaced grid is imaged, shown in figure 3.3. The size of the grid spacing is taken from the center of a black line to the center of the next black line. The grid size of 10  $\mu\text{m}$  is measured as 240 pixels. Therefore 1 pixels corresponds to 0.042  $\mu\text{m}$  (this is the pixel resolution). The standard deviation on this measurement of 10  $\mu\text{m}$ , after averaging over 10 measurements, is 16 pixels (corresponding to 0.67  $\mu\text{m}$ ).

It can be noted by imaging the grid, that the squares of the grid are imaged as squares which implies that there is no noticeable astigmatism that magnifies the one axis different to the other.

### 3.1.2 Determining the image resolution

The image resolution is determined using the air force target resolution mask (*Thorlabs R3L1S4P, USAF1951 with positive pattern*). Figure 3.4 shows the smallest resolution lines, group 7 element 6, of the target on the left. The right hand side of figure 3.4 displays the pixel intensity as line outs are take along the  $x$  (above) and  $y$  (below) axes.

In the target, group 7 element 6 has 228 lines per millimeter and the distance between two lines is specified as 2.19  $\mu\text{m}$ . Two neighbouring lines are visibly distinguishable from each other. This was the smallest target available to image. The distance of 2.19  $\mu\text{m}$  is well resolved as seen in the image and line outs plotted. This distance of approximately 2.19  $\mu\text{m}$  is thus not the resolution limit of the setup. However, this shows that with this setup, samples of this size or bigger can be well resolved.

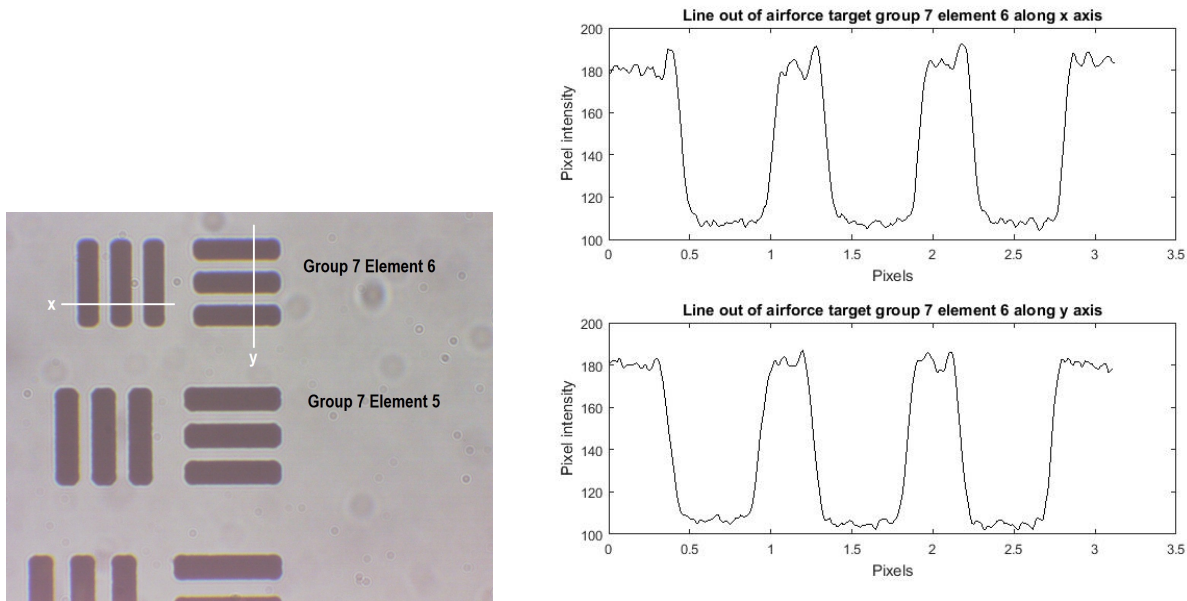


**Figure 3.4:** The lines on the air force target is imaged to the left. At the top is group 7, element 6, which has 228 lines per millimeter and the distance between two lines is  $2.19 \mu\text{m}$ . Line outs along the  $x$  and  $y$  axes are plotted on the right.

### 3.1.3 Determining the power in the optical trap

To measure the power in the focus, in other words the power in the trap, the power is measured before the 100X objective, the spot size here is 8 mm in diameter, and the hand held Thorlabs power meter (*Thorlabs PM160*) has a detection area of 9.5 mm in diameter). It is assumed that the beam diameter is slightly smaller than the back aperture of the objective such that light is not lost when entering the objective. Also, the losses in the objective are small enough to be neglected. For various laser current settings the power is measured and tabulated in table 3.1. Initially the laser current is increased in increments of 10 mA, but after 10 increased measurements the increase in the power measured is linear, so the increments are increased to 50 mA steps.

These measurements are averages taken over the course of seven different days, at different time periods after the laser had been switched on. The power measurements do not deviate significantly over the course of the different measurements. Also, increasing and decreasing the laser current yields the same power measurements. Measurements were only taken up to the laser setting of 500 mA, because the power meter saturates above 200 mW.

Table 3.1 is used to draw the calibration curve, figure 3.5. Significant power is measured from 40 mA and higher. For currents in the laser below 40 mA, lasing does not yet occur. The power increases linearly in this relation as the current is increased on the laser. A linear fit is drawn through the points above 50 mA to give the calibration from the laser setting to the power in the trap (in Watts),

$$P(x) = 0.00043x - 0.016 \quad (3.1)$$

These powers will be referred to later in the text as the trap power.

Laser current [mA]	Power [W]	Standard deviation [W]
0	$6.0 \times 10^{-9}$	$1.0 \times 10^{-9}$
10	$1.8 \times 10^{-6}$	$7.8 \times 10^{-9}$
20	$8.2 \times 10^{-6}$	$3.1 \times 10^{-8}$
30	$3.4 \times 10^{-5}$	$1.4 \times 10^{-7}$
40	$1.1 \times 10^{-3}$	$7.1 \times 10^{-5}$
50	$4.4 \times 10^{-3}$	$5.1 \times 10^{-5}$
60	$8.7 \times 10^{-3}$	$6.3 \times 10^{-5}$
70	$1.3 \times 10^{-2}$	$7.4 \times 10^{-5}$
80	$1.8 \times 10^{-2}$	$7.8 \times 10^{-5}$
90	$2.2 \times 10^{-2}$	$9.4 \times 10^{-5}$
100	$2.7 \times 10^{-2}$	$6.2 \times 10^{-4}$
150	$4.8 \times 10^{-2}$	$2.1 \times 10^{-4}$
200	$7.0 \times 10^{-2}$	$2.8 \times 10^{-4}$
250	$9.2 \times 10^{-2}$	$3.5 \times 10^{-4}$
300	$1.1 \times 10^{-1}$	$5.2 \times 10^{-4}$
350	$1.3 \times 10^{-1}$	$8.3 \times 10^{-4}$
400	$1.6 \times 10^{-1}$	$1.0 \times 10^{-3}$
450	$1.8 \times 10^{-1}$	$8.3 \times 10^{-4}$
500	$2.0 \times 10^{-1}$	$6.9 \times 10^{-4}$

**Table 3.1:** The power in the setup of the optical tweezers is measured before the 100X objective for the various laser current settings.

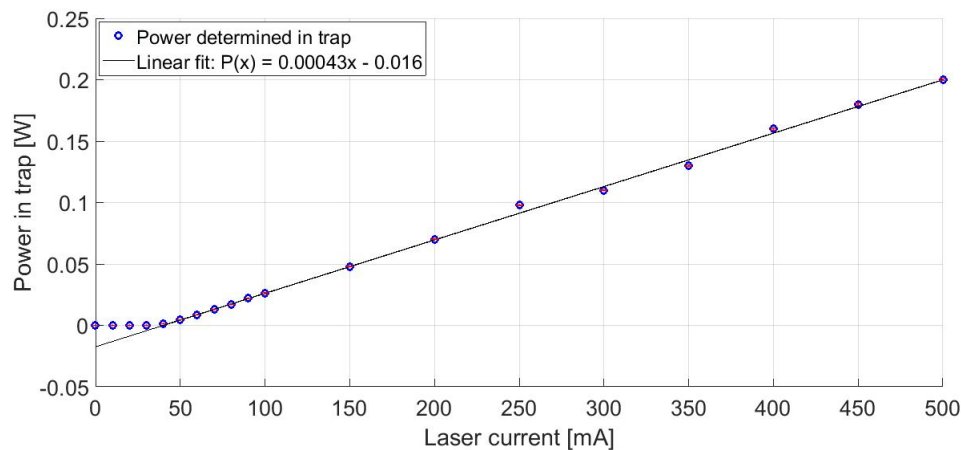


**Figure 3.5:** The power in the trap is plotted here for various laser current settings with a fit of  $P(x) = 0.00043x - 0.016$ .

### 3.1.4 Sample preparation

The sample that is used for principle trapping demonstrations and trap force calibrations are dielectric silica beads suspended in distilled water. Two sizes of particles of diameters  $1 \mu\text{m}$  and  $4 \mu\text{m}$  were used respectively. A droplet of the suspension is placed onto a  $0.17 \text{ mm}$  thick cover slide, figure 3.6 (a). The  $1 \mu\text{m}$  silicon dioxide particles (*Sigma-Aldrich*, product code 56798) are specified to be  $1.04 \mu\text{m}$  in diameter, (but the average diameter of the particles will be measured in the following section).



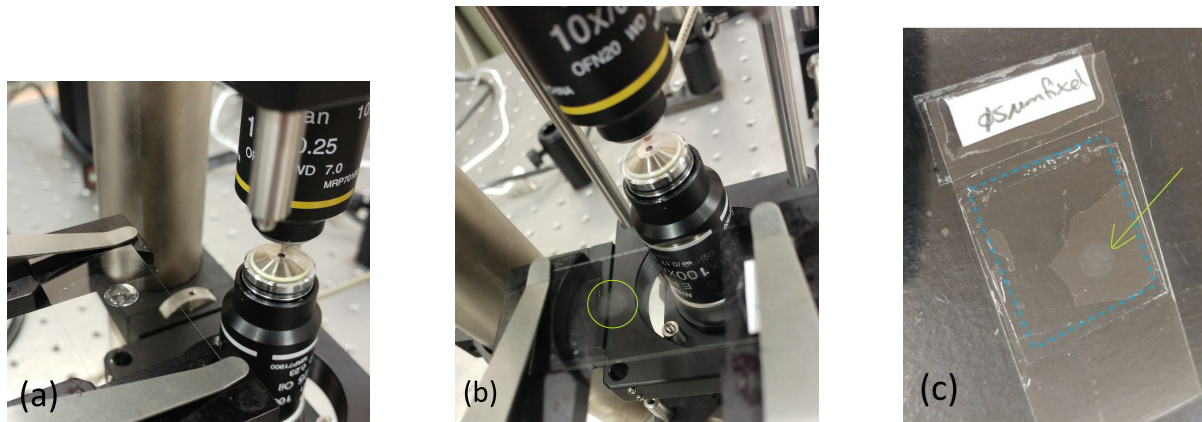


**Figure 3.6:** Sample preparation of silica beads and distilled water droplet on a cover slide. (a) A droplet of distilled water with diffused dielectric beads is placed on a cover slide (on the translation stage) in the trap setup. (b) Fixed beads on a cover slide are prepared by leaving droplet of beads-water suspension to dry. The water to evaporates, and the beads become fixed to the surface of the cover slide. (c) The suspension or dried beads (indicated by green arrow) can be protected from dust another cover slide placed over it. It is sealed to prevent evaporation (blue dotted line).

The concentration of the stock is 5%. It is further diluted with distilled water until only up to five beads are seen on the screen at a given time. This is to prevent multiple beads trapping simultaneously.

The  $4\ \mu\text{m}$  beads are also suspended in distilled water, diluted until the concentration is low enough for only up to one or two beads are imaged by the camera at a given time.

For the measurements that need fixed beads, a droplet is placed on the cover slide and then left for a few hours to allow the water to evaporate. An example of dried, fixed, beads on the surface of a cover slide is shown in figure 3.6 (b). Placing a cover slide over the beads protects it from dust.

To prevent evaporation of the water from the droplet and that the curved surface of the water does not influence the light imaged on the quadrant position detector, the sample can be covered using another cover slide. Also, to protect the fixed beads from dust another cover slide is placed on top of the fixed beads (figure 3.6 (c)). Using clear nail polish, a square is drawn on the bottom slide to create the cage walls (indicated in blue in the photo). A droplet of the beads-water suspension is then deposited into this cage and another cover slide placed on top. It is sealed and air bubbles are removed by wiping across the top cover slide with a piece of lens cleaning tissue.

### 3.1.5 Determining the bead size

An image of the beads on the camera is used to measure the average size of the beads. The diameter of the dielectric beads are determined by measuring the amount of pixels in the diameter of a bead. This is multiplied by the pixel calibration conversion factor determined as above in section 3.1.1. The image is captured using ThorCam software (*version 2.6.7064*) as setup as figure 3.1. The diameter of the beads is measured using *ImageJ* software (*Java 1.6.0\_20; 64 bit*).

For the larger beads, the diameter was measured for 10 beads and an average diameter of  $4.22\ \mu\text{m}$  was measured (standard deviation of  $0.156\ \mu\text{m}$ ). In the same way, the smaller beads are measured to be  $1.01\ \mu\text{m}$  (standard deviation of  $0.085\ \mu\text{m}$ ).

### 3.1.6 Determining the piezo driver calibration

To determine the displacement of the sample on the stage as a voltage is applied on the piezo drivers, a calibration is done using the  $10\ \mu\text{m}$  spacing grid from the distortion target (*Thorlabs R1L3S3P*). The grid is imaged with white light onto the camera (figure 3.1). Using the ATP User software mentioned above, a voltage is applied to the  $x$  and  $y$  drivers respectively and the distance the grid moves is recorded on the camera using Thorcam software. The displacement is averaged over 10 measurements and plotted in figure 3.7. A calibration of  $0.05\ \mu\text{m}$  per pixel is used using the same method as in section 3.1.1. In these graphs, the calibration curves show displacement in micron with respect to the voltage applied in each coordinate.

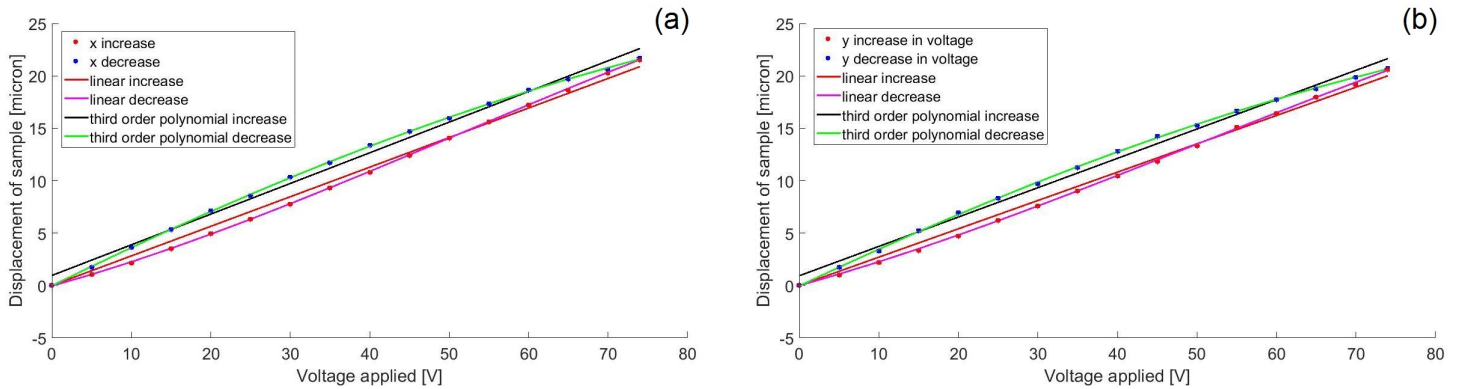


**Figure 3.7:** The piezo driver is calibrated along the  $x$  coordinate in (a) and  $y$  coordinate in (b), using the pixel calibration of  $0.05\ \mu\text{m}$  per pixel.

The voltage is increased from 0 V to 74 V first (74 V because the maximum allowed is 75 V) and then decreased to see whether the stage returns to the same position when decreasing the voltage. The two curves do not coincide exactly and the gradients differ, but the displacement at the maximum voltage is the same.

The displacement of the stage is in an approximately linear relation to the voltage applied. This is seen when a linear and a third order polynomial are fitted to the data points. The curves fitted for the displacement in micron,  $D$ , with respect to the potential applied,  $U$ , in figure 3.7 are displayed in table 3.2.

	Linear fit	$R^2$	Third order polynomial fit	$R^2$
$x$ : increase in voltage	$D_1(U) = 0.282x$	0.99	$D_3(U) = -1.41 \times 10^{-5}x^3 + 2.15 \times 10^{-3}x^2 + 0.209x + 0.048$	1
$x$ : decrease in voltage	$D_1(U) = 0.293x + 0.956$	0.99	$D_3(U) = -2.46 \times 10^{-6}x^3 + 9.12 \times 10^{-4}x^2 + 0.373x - 0.0288$	1
$y$ : increase in voltage	$D_1(U) = 0.27x$	1	$D_3(U) = -1.19 \times 10^{-5}x^3 + 1.79 \times 10^{-3}x^2 + 0.21x - 0.048$	1
$y$ : decrease in voltage	$D_1(U) = 0.28x + 0.931$	0.99	$D_3(U) = -2.56 \times 10^{-6}x^3 + 8.84 \times 10^{-4}x^2 + 0.36x - 0.0365$	1

**Table 3.2:** The curves fitted to the voltage-position calibration of the piezo drivers used with the nanomax translation stage are displayed here. The fits for both increasing and decreasing the voltage are given for  $x$  and  $y$  coordinates.

In the third order polynomials, the third order and second order terms have small coefficients and so the first order term dominates. (The constant term is on the same order as the standard deviation in the data, so this term is also neglected.) Neglecting the higher order terms, the polynomial equations become similar to the linear equations for the fits. In this way, and from the  $R^2$  values, it can be said that the linear curves

are good fits to the data and that the displacement is linear with respect to the voltage applied. Using the linear fits (figure 3.7), the piezos move the sample approximately  $0.28 \mu\text{m}$  for every 1 V applied.

As an experimental note, if a particle is too far from the trap, the piezo cannot displace the position of the stage large enough to reach that range. The piezo has a maximum range of 0 V to 75 V. For 74 V applied to the piezo, the stage is moved approximately  $21 \mu\text{m}$ . A maximum of 75 V can be applied to the piezos. To ensure movement of the stage within the active region, the piezos are initialized to 35 V, which corresponds to a possible displacement of approximately  $10 \mu\text{m}$  in  $x$  and  $y$ .

### 3.1.7 Distinguishing between the trapping of individual or multiple beads

When using the optical tweezers to trap silica beads, it is very likely that more than one bead will become trapped simultaneously. This will have undesired effects on, for example, the force calibration. When multiple beads are trapped, the beads stack vertically along the  $z$ -axis (optical axis). By only looking at the then-present image the camera, it is not always distinguishable when there is one or more than one bead in the trap.

Figure 3.8 compares the cases of trapping one or multiple  $1 \mu\text{m}$  beads simultaneously. The images were taken with the same exposure time of 4.09 ms, and the pixel intensity on a scale of zero to 255.

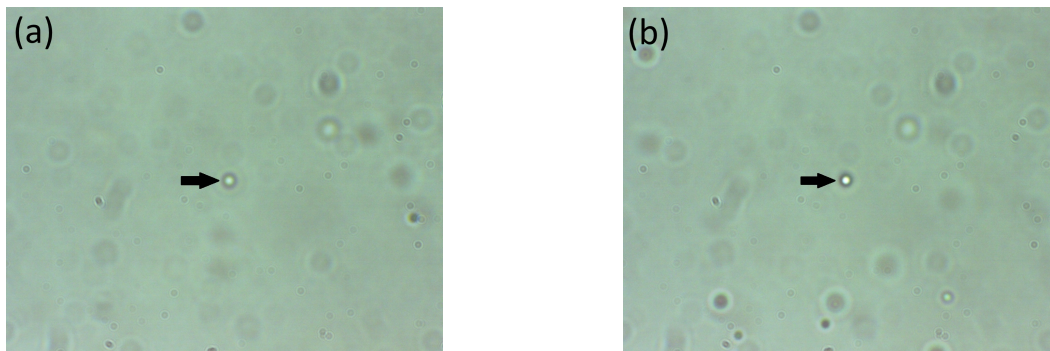


**Figure 3.8:** In (a) only one bead is trapped. In (b) multiple (three or more) beads have been trapped. The position of the trapped beads are indicated by the arrow. Looking at one image alone, it is difficult to say how many beads are trapped. However, comparing brightness of the trapped beads' image, one can say that in one case multiple beads are trapped.

The most notable difference between images (a) and (b) in figure 3.8 is the increase in brightness of the trapped beads when multiple beads are trapped. The spherical beads have a lensing effect when white light is transmitted through the beads. The beads are imaged onto the camera and by looking at horizontal line outs across the center of the trapped bead, a maximum pixel intensity (brightness) is measured. An average of this over repeated measurements, of one or multiple beads in the trap are tabulated in table 3.3.

As the number of beads in the trap increases, the pixel intensity measured by the camera increases. The difference between trapping one or two beads is an increase of 18% in the pixel intensity measured on the camera. The intensity measured when there is one bead in the trap is increased by 22% when there are three or more beads trapped. The approximately 20% increase in the pixel intensity can be used as a measure to determine if more than one bead has fallen into the trap.

Number of beads	Average pixel intensity (0 to 255)	Standard deviation
1	159	15
2	194	26
3+	204	12

**Table 3.3:** The maximum pixel intensities measured (horizontally across the center of the bead) when one or multiple 1  $\mu\text{m}$  beads are in the trap, are averaged over various measurements and tabulated here.

## 3.2 Characterizing the optical tweezers by force calibration setup

The setup of the optical trap, as seen in figure 3.1, is built to also measure the strength of the forces that the optical tweezers exert on a particle. This is done by determining the strength of the trap in terms of the force constant,  $k$ .

After passing through the sample, the NIR (975 nm) laser is reflected from the dichroic mirror (DM2) through a lens (L5) of focal length 40 mm. This lens images the collimated light from the back focal plane of the condenser on to the detector. A quadrant photodiode detector (QPD) is used for position measurements. The position of the bead relative to the center of the trap is imaged due to the refraction of the light through the bead in the trap. As a bead in the trap is displaced, the image on the QPD also changes and a different position is measured.

Alignment of the dichroic mirror, DM2, is done by removing the lens (L5), neutral density (ND) filter, and QPD. Two irises are placed on this horizontal cage-system-arm of the setup and the beam is aligned through these two irises by adjusting DM2. Once aligned, the lens, ND, and QPD are placed in the setup.

The position of the QPD from the lens is such that the detector's active region is not overfilled, but that the spot size on the detector is also large enough for a signal to be measured significantly in each quadrant. (The final spot size on the QPD is 3 mm in diameter).

A neutral density (ND) filter, with optical density of  $\text{OD} = 1.0$ , (*Thorlabs ND10A*) is placed before the QPD to prevent saturation of the detector. The power on the QPD must be in the detector's optimal range at trapping powers of the laser. From preliminary trapping of the 1  $\mu\text{m}$  silica beads (section 4.1), it is known that trapping occurs at trap powers between 48.3 mW and 197 mW. This corresponds to laser current settings between 150 mA and 500 mA (from section 3.1.3). Using a filter with optical density of 1.0, the power of the light on to the QPD is measured with the hand held power meter, and is tabulated in table 3.4. This optical density of 1.0 allows for using the trapping power of the laser that is optimal for trapping the beads, as well as being the range that the QPD is sensitive in. From this table it can be seen that the force calibration of the trap should therefore be done at a laser current setting between 150 mA and 400 mA.

The QPD is placed in a  $xy$  translation mount. The position sensing detector software from Thorlabs, ATP User software, (*ATPQuad, version 3.0.0(3.0.3)*) is used to measure the bead's position in the trap. The detector is aligned such that the trap position is in the center of the QPD. To center the trap position, the voltage difference measurements of a trapped bead are minimized by translating the QPD in  $x$  and  $y$ .

The force calibration procedure uses the OTKB software for optical tweezing from Thorlabs (*version 2.0.0*) and the movement of the stage is controlled using ATP User program

Laser current [mA]	Laser Power [W]	Power at QPD [mW]
50	$4.4 \times 10^{-3}$	0.027
100	$2.7 \times 10^{-2}$	0.168
150	$4.8 \times 10^{-2}$	0.306
200	$7.0 \times 10^{-2}$	0.444
250	$9.2 \times 10^{-2}$	0.582
300	$1.1 \times 10^{-1}$	0.717
350	$1.3 \times 10^{-1}$	0.85
400	$1.6 \times 10^{-1}$	0.985
450	$1.8 \times 10^{-1}$	1.11
500	$2.0 \times 10^{-1}$	1.24
550	**	1.36
600	**	1.49

**Table 3.4:** The power is measured at the position of the QPD for various laser current settings (calibrated in section 3.1.3) using the neutral density filter with optical density of 1.0. Above 500 mA laser current, the power in the trap is too large to be measured using the hand held power meter\*\*.

and monitored with the position sensing detector.

For the force constant to be determined, the temperature needs to be known and is measured using an infrared thermometer (*Mac Afric DT8530*, with resolution of 0.1 °C). The fluctuations in the position of the bead are very sensitive to external vibrations. For this reason, the optical table is isolated by floating the table on air.

### 3.2.1 The quadrant position detector (QPD)

The quadrant position detector (QPD) is used to determine the position of the bead. The output of the detector is a voltage signal which can be converted to a position measurement to detect the position of the bead relative to the trap.

The QPD detects the intensity of incident light in the four quadrants of the  $xy$  plane. It uses photo diode detectors to pass a voltage signal to the user. The voltage outputs in the  $x$ -coordinate,  $V_x$ , and  $y$ -coordinate,  $V_y$ , are difference voltages measurements [14, p. 266]. The QPD also gives a sum voltage,  $V_{sum}$ , that is used for normalizing the signal. The voltage difference from the sensor in the  $x$ -coordinate is inverted such that as the beam moves from left to right, the voltage becomes more negative [59].

In the following  $A$ ,  $B$ ,  $C$  and  $D$  refer to the four quadrants of the detector as shown in figure 3.9.

$$V_{x'} = (A + B) - (C + D) \quad (3.2)$$

$$V_{y'} = (A + C) - (B + D) \quad (3.3)$$

$$V_{sum} = A + B + C + D \quad (3.4)$$

Figure 3.9 illustrates the QPD output at an example of a bead positioned diagonally off center from the trap position on the QPD. The primed values are the values before inversion in the  $x$ -coordinate, and values without primes are those used by the system (that is after inversion of the  $x$ -coordinate).



**Figure 3.9:** The displacement of a bead to the right and above the trap center is imaged on to the QPD (quadrant position detector). The image results in a voltage signal in  $x$  and  $y$  that translates to the position of the beam relative to the center, as shown in the table.

### 3.2.2 Setup and procedure for position and force calibration using the OTKBFM-CAL module and software

The Thorlabs software, OTKBFM-CAL (*version 2.0*) is used for force calibration with the force module of this optical tweezers setup. With this software, one is able to determine the position and force calibration of the trap. In this section, the procedures outlining the position calibration and the force calibration are discussed.

#### 3.2.2.1 Position calibration

To calibrate the position measured from the voltage signal of the QPD detector, a plot of the voltage signal at various positions of a fixed bead in the trap must be made and a calibration curve fitted to this. Fitting a linear curve on the plot gives the calibration factor from volts to meters. The position is calibrated along the  $x$  and  $y$  axes of the trap respectively. The position calibration does not depend on the power, and therefore only needs to be done once at a chosen laser current setting. The position calibration is done using the OTKB software.

The position calibration is crucial for the equipartition method to determine the forces in the trap. However, in the power spectral method the frequency of the bead's fluctuations in position is recorded. The position calibration is therefore not used in this method.

To do the position calibration, a fixed bead is displaced across the beam. The bead will not move with the trap, so the position (known from the piezo stage) with respect to the measured QPD voltage is determined. This data is used for the position calibration.

Using the OTKB software, the fixed bead is centered on the QPD. Then translating this fixed bead through the trap center (left-to-right) in  $x$  and (up-down) in  $y$  will result in a oscillating voltage signal as the bead is imaged onto the different quadrants of the detector. This voltage signal is plotted and should have a linear region as the bead is moved across the trap center. This linear curve is the volts-to-meters position calibration curve.

#### 3.2.2.2 Force calibrations

The trap force calibration is done using the OTKB software. The temperature, bead radius and viscosity of the medium surrounding the bead are input as follows: the temperature recorded during the measurements with the infrared thermometer (was measured and updated constantly throughout, but had an average of 20.1 °C), a bead radius of 0.5  $\mu\text{m}$ , and a viscosity of 1.012 mPa.s. Data is recorded over a time period of 0.3 seconds.

One single, free bead is trapped and the force calibration is performed. For the trap strength constants measured using the equipartition method, the position calibration above is used.

For the power spectral density method, no position calibration is needed. The time domain data is plotted and a Fourier transform of the time domain data to the frequency domain is done. A Lorentzian is fitted to the data as discussed in section 2.3.2. The corner frequency is extracted from the fit and the force constant,  $k$ , is determined using the temperature, bead radius and viscosity given as input parameters.

### 3.3 Setup for the measurement of the stall forces of molecular motors

To determine the forces that molecular motors in an onion cell exert as they transport vesicles in the cell, the vesicles are trapped with the optical tweezers. The guide lines of an MIT practical outline for optical trapping [49] was used as a reference.

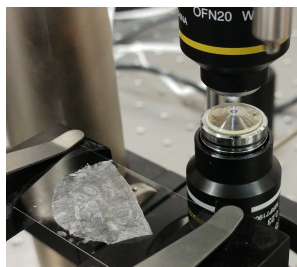


**Figure 3.10:** A photo of the onion cells sample preparation used for vesicle trapping is shown. A layer of onion is peeled off and placed on the cover slide in the tweezers setup.

A cover slide with one layer of onion is placed flat on a cover slide (figure 3.10). A second cover slide is placed on top, covering the sample to protect it from dust, and to ensure the onion layer remains flat.

A cell is brought into the focus and different dynamics in the cell can be observed. Different behaviours are observed, namely the random Brownian motion of some vesicles, thus not transported by motors, as well as the vesicles moving in a specific direction being transported by motors.

A vesicle transported by a molecular motor is identified by identifying a path that more than one vesicle follow continuously (at an approximate constant speed). The sample is positioned such that the path of the vesicles overlaps with the trap position. The laser power is increased, increasing the forces in the trap and making the trap strong enough to trap a vesicle moved along by a motor. At a threshold laser power, the vesicle will not be able to move through the trap without becoming trapped, stalling the motion of the motor. This power is recorded and can be converted to a stall force by using the calibration curve determined in section 3.2. The force is determined for a distance, no larger than the radius of the vesicle.  $0.5 \mu\text{m}$  is used, a small displacement from the trap center. If the laser power is decreased, the vesicle can continue its motion along the path if the motor is still attached. This is repeated several times with different cells and onions on different days.

*Remark.* The bead size used to determine the trap stiffness constant in calibration, should be similar to the size of the vesicle. This is due to the fact that the radius is a variable used in determining the trap constant using the more accurate power spectrum method. The refractive index of the vesicle is unknown, but it is assumed to be similar to that of the bead such that the force constant calibration with silica beads can be used.

The speeds of the vesicles are determined using *ImageJ* software and measuring the number of pixels a vesicle displaces in a certain number of frames. The temperature of the cells are not changed, but measured to be on average 20.1°C.

### 3.4 Setup for the integration of optical tweezers with fluorescence microscopy

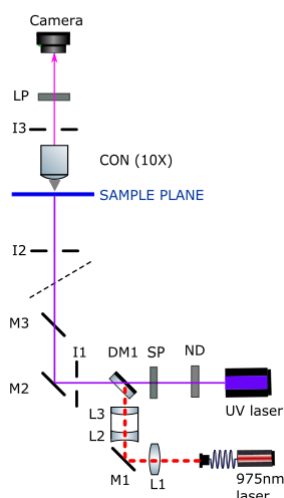


**Figure 3.11:** The setup of the integration of the optical tweezers with fluorescence imaging using a UV laser is shown here. The dotted red line shows where the previous trapping setup would be integrated if the 100X objective was in place.

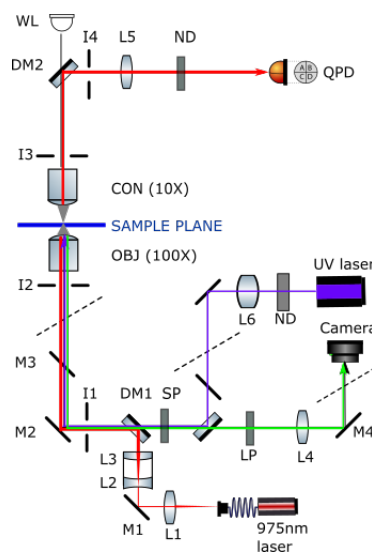


**Figure 3.12:** The ideal fluorescence (wide field) imaging integration with the optical tweezers setup for simultaneous tweezing and imaging.

In this section, the setup of integrating another laser to image a sample using fluorescence is described. The fluorescence is detected in transmission. An UV excitation laser of 405 nm is used to excite fluorescence from an onion layer stained with Rhodamine 6G dye and chlorophyll in a leaf. These samples were placed on a microscope slide in the setup as shown in figure 3.11. The chlorophyll in a leaf fluoresces between 650 nm and 700 nm [60]. The spectrum for the dye's fluorescence is shown in figure 3.13.

A neutral density filter is added after the UV laser to allow attenuation of the intensity onto the sample. No lens is used to focus the UV light onto the sample. The 10X condenser lens is used to capture the fluorescence and image it onto the camera. A 550 nm long pass (LP) filter (*Thorlabs FEL0550*, transmission of 88.2% at 578 nm) is used to remove the UV light that is transmitted through the sample, blocking it from the camera. A LP filter blocks light with a shorter wavelength and allows light with longer wavelengths to be



transmitted. Therefore the shorter wavelength 405 nm light does not reach the camera, but the longer, fluorescent wavelength does.

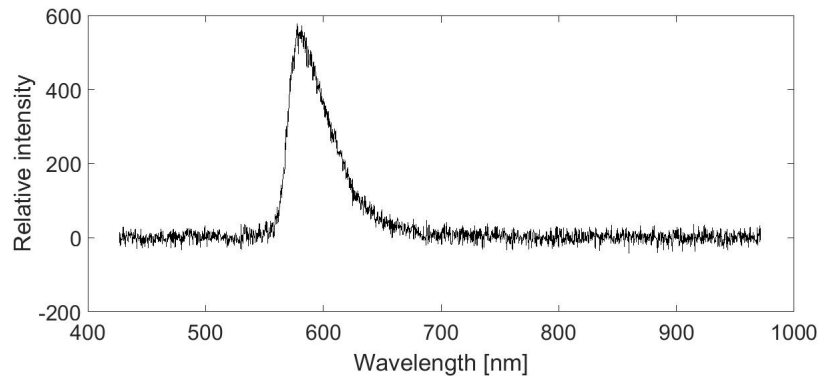


**Figure 3.13:** The fluorescence spectrum of Rhodamine 6G dye with excitation light of 405 nm is shown. The emission is seen to peak at 578 nm.

A 10 bit CMOS sensor (*Thorlabs DCC3240, USB 3.0 digital camera*) is used here as a detector. The larger dynamic range of the 10 bit sensor is advantageous to the 8 bit used earlier in optical tweezing section, as it is more sensitive to small changes in the intensity.

Wide field images are captured of the fluorescence from chlorophyll and the dye. For contrast, the image is taken first with the white light LED (placed in the position of the laser in the setup shown) and then the white light is turned off and the UV laser is switched on.

The ideal situation for this integrated setup would be epi-detection, as in a setup such as figure 3.12. This Fluorescence Microscopy Module is an extension module to the optical tweezers setup from Thorlabs, (*Thorlabs OTKB-FL*). The fluorescence excitation and optical tweezing lasers follow the same optical path and both can be used simultaneously, in parallel. Lens L6 is used to collimate the light for filling the back aperture of the objective lens and so stimulating the fluorescent process used in imaging. An emission filter can also be added after the lens to select a certain bandwidth to excite specific fluorescent processes. Unfortunately, for the samples used, the 100X objective captured too little fluorescent light and cannot be used to form images from the samples used, and therefore the setup in figure 3.11 is used.

**Sample preparation** The samples imaged using the setup described above were thin slices of a leaf placed on a microscope slide as well as an onion stained with drops of Rhodamine 6G dye. These are shown in figure 3.14. The leaf should be thin enough to allow light to be transmitted and detected by the camera.

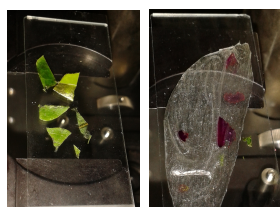


**Figure 3.14:** The samples used for imaging fluorescence are a thin piece of leaf (on the left), and a layer of onion stained with Rhodamine 6G dye (on the right).

### 3.5 Setup for ptychography

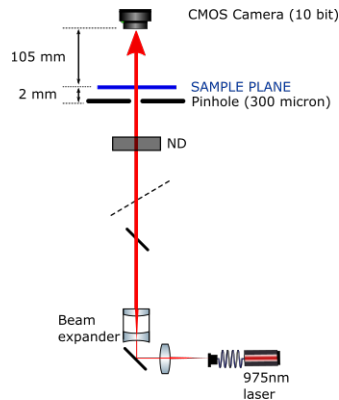


**Figure 3.15:** Ptychography is done using a 975 nm laser, creating diffraction patterns recorded on a 10 bit CMOS sensor in the far field. The sample is illuminated with a 300  $\mu\text{m}$  diameter pinhole at a distance of 2 mm from the sample.

The ptychography measurements were performed using the 975 nm laser from the optical tweezing setup. A schematic of the setup is shown in figure 3.15. After the beam expander, the collimated beam is reflected vertically upwards, passing through a neutral density filter with optical density of 2.0, (*Thorlabs ND20A filter*). The filter ensures that the detector is not saturated. The light then continues through a pinhole of 300  $\mu\text{m}$  in diameter. The pinhole is placed as close as possible to the sample (2 mm), so that the probe in the PIE algorithm can be assumed to have a flat phase and flat top amplitude.

The sample imaged is a sample of cellulose acetate, cut to a obtuse-angled corner. This sample is chosen as it is expected to give a relative phase to reconstruct, as well as possible amplitude changes where the sample is present. The sample is placed on the NanoMax-TS translation stage (*Thorlabs MAX 311D/M*) used for holding the sample during optical tweezing. The sample is moved by the stage such that the stationary illumination spot (beam and pinhole) is scanned across the sample. The sample is moved manually by hand. The step size of the sample translation is 100  $\mu\text{m}$  and a  $n \times m$  grid of illumination (probe) positions is created.

At each stage position, five images are captured so that the pixel intensity can be averaged over these images. The background light on the detector is also measured while the laser is off. The background is to be subtracted from the images to reduce the noise.

To ensure accurate Fourier transforms between object and frequency space, the diffraction patterns are recorded in the far field, at a distance 105 mm from the sample. A 10 bit CMOS sensor (*Thorlabs DCC3240, USB 3.0 digital camera*) is used as a camera.

The size of the active region of the detector is 6.78 mm by 5.43 mm. The larger the detector's active region, the higher the spatial frequencies that can be recorded. Higher spatial frequencies mean that sharper edges can be resolved of the object (real) space. The size of a pixel is 5.3  $\mu\text{m}$  (square pixels). At this distance of 105 mm from the sample, this implies an angle of  $5.05 \times 10^{-5}$  radians per pixel.

To reconstruct the sample as discussed earlier in section 2.5, the diffraction patterns are used as input to the PIE algorithm. The code used can be found in appendix A.

## Chapter 4

# Results and discussion

Using the setup from the previous chapter, the following results were found. The results are divided into three sections. First, optical tweezing was demonstrated (section 4.1). This included the trap strength calibration, as well as the measurement of molecular motor stall forces. Second, images were obtained using the fluorescence setup (section 4.2). Third, simulated and experimental results of ptychography will be discussed (section 4.3).

### 4.1 Optical tweezers

The optical tweezers setup was used to trap beads of  $1\ \mu\text{m}$  and  $4\ \mu\text{m}$  in diameter. The position of the trap is located through observing the behaviour of the beads (with the camera) in the vicinity of the trap, as they tend to accelerate towards it [61]. Once the bead is in the trap, translating the stage - and therefore the sample - left or right will not move this bead on the screen, while other beads in the background move left or right.

Figure 4.1 show the movement of the smaller beads in the trap. The consecutive frames are snapshots from a video taken whilst the sample is moved diagonally right and upwards with respect to the trap position. On the figures,  $T$  marks the trap position. The bead that is trapped therefore moves diagonally down and left with respect to the environment. The other beads in the images are not trapped. They are either diffusing in the water or lie on the cover slide (depending on the  $z$  position in the images). Another example of  $1\ \mu\text{m}$  beads trapped and tweezed in water is shown in video form and can be viewed at <http://hdl.handle.net/10019.1/103606>.

Optimal trapping occurs between the power in the trap being 48.3 mW (laser current setting of 150 mA) and 197 mW (laser current setting of 500 mA).



**Figure 4.1:** Movement of a trapped  $1\ \mu\text{m}$  bead (indicated by  $T$ ) diagonally down and left with respect to the other beads, not trapped, in the sample.

### 4.1.1 Force calibration of trap using dielectric beads

The force calibration results are described below. First, the position calibration must be completed to be used in the equipartition method (section 4.1.1.2). Then the forces in the trap can be calibrated using the equipartition- and power spectrum method. Comparison of the forces the optical tweezers exerted on beads of  $1\ \mu\text{m}$  and  $4\ \mu\text{m}$  in diameter follows.

#### 4.1.1.1 Position calibration of the quadrant position detector

A fixed bead is moved across the trap position along the  $x$  and  $y$  axes respectively. The bead's position is tracked on the QPD along the  $x$  axis and the QPD voltage output  $V_x$  is shown in figure 4.2. This was done using a  $1\ \mu\text{m}$  bead. The number of steps were 60 and the number of averages was 2000. The position calibration was completed in the detector's optimal range (at a laser current of 250 mA).

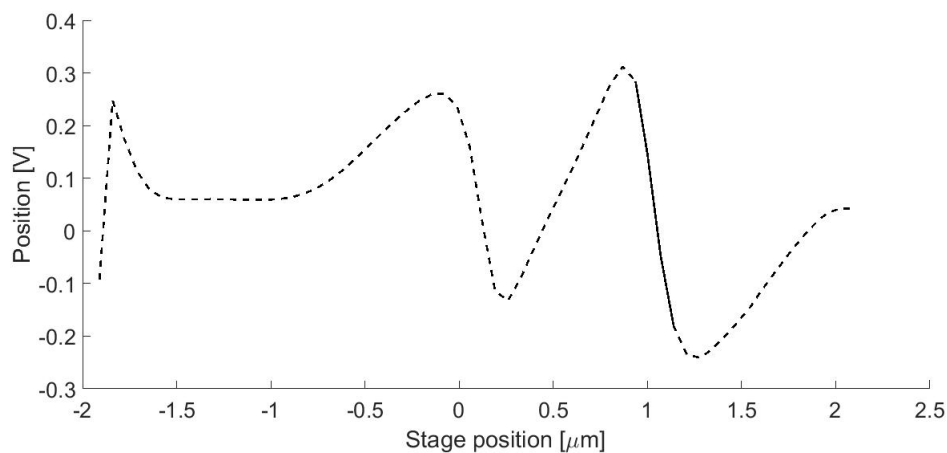


**Figure 4.2:** An example of the position calibration is shown for translation of the stage along the  $x$  axis. A linear slope is extracted along the solid part of the plot and a position calibration factor of  $-0.53\ \mu\text{m}/\text{V}$  found.

A linear slope is used to find the gradient and the position calibration factor determined. In this example a position calibration of  $-0.53\ \mu\text{m}/\text{V}$  was determined (fitting the linear segment with a mean square error of  $1.2 \times 10^{-3}$  along the solid segment of the plot in figure 4.2). Doing the calibration multiple times, similar factors were found.

Note that the  $z$  position of the fixed bead during the position calibration must be in the trapping plane. The position of the bead in all three coordinates is crucial and proved difficult to find exactly, consistently. This makes repeating the results of the position calibration nontrivial.

#### 4.1.1.2 Force calibration using the equipartition method (1)

This method was described in section 2.3.1. The variance in a trapped bead's position is measured and the trap constant,  $k$ , is determined using equation (2.4). The position calibration above is used and forces in the trap measured for various trap powers, figure 4.3. For each power, the calibration is averaged over ten measurements at approximately the same  $z$  position.

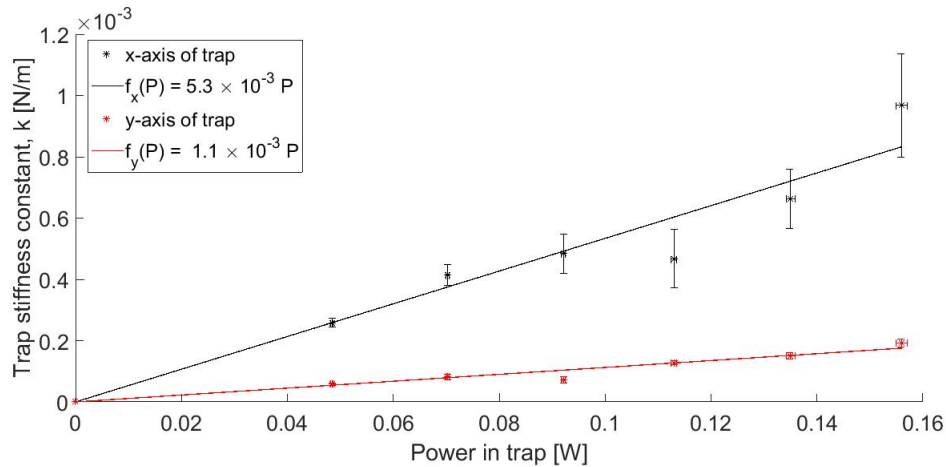


**Figure 4.3:** The force constants in the trap determined using the equipartition method for beads  $1 \mu\text{m}$  in diameter.

The trap constant,  $k$ , in  $\text{N/m}$  is seen to increase linearly as the trap power increases. The fits are as follows for the trapping constants in the  $x$  (black) and  $y$  (red) axes of the trapping plane as a function of the trapping power,  $P$ .

$$f_x(P) = 5.3 \times 10^{-3} P \quad R_x^2 = 1 \quad (4.1)$$

$$f_y(P) = 1.1 \times 10^{-3} P \quad R_y^2 = 0.95 \quad (4.2)$$

Looking for example at a trap power of 113 mW, for a displacement of  $0.5 \mu\text{m}$  from the trap center along the  $y$  axis, the bead will experience a force of 64 pN. The displacement  $x = 0.5 \mu\text{m}$  is chosen, because the parabolic approximation of the trapping potential is valid for displacements from the trap center up to the size of the particle's radius [14, p. 34]. This force is similar to other results from similar optical tweezers [10] and [56].

The difference in the trap stiffness constants along the  $x$  and  $y$  axes (the smaller gradient along linear fit in  $y$ ), can possibly be attributed to an astigmatism and a non-circular spot in the focus.

The smaller error in the  $y$  axis compared to that of the  $x$  axis, is possibly due to a poor position calibration here in  $x$ . The position calibration of section 4.1.1.1 was not always repeatable. This factor made the power spectral density method in the following section more reliable than the equipartition method in this setup.

#### 4.1.1.3 Force calibration using the power spectral density method (2)

The force calibration using the power spectral density (PSD) method is done here for  $1 \mu\text{m}$  beads at an average temperature ( $T$ ) of  $19.6^\circ\text{C}$  ( $292.8\text{K}$ ) and viscosity of the water  $1.012 \text{ mPa}\cdot\text{s}$ . For various trapping powers, the calibration is averaged over ten measurements at approximately the same  $z$  position.

This method was described in section 2.3.2. An example of the data acquired is taken at a trap power of 113 mW. As mentioned in the theory, the fluctuations in position of the bead in the trap are recorded on the QPD. Such a measurement is shown on the left in figure 4.4. The position of the trapped bead in the  $x$  axis fluctuates around an average position of relative to the center of the QPD. The power spectrum of the data is shown on the right. The power spectrum is plotted on a logarithmic scale to demonstrate the roll off of the amplitude at the corner frequency.

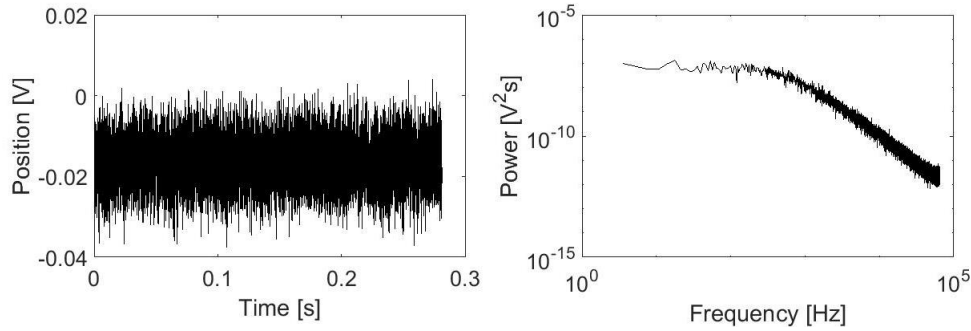


**Figure 4.4:** On the left, the position of the 1  $\mu\text{m}$  bead is shown fluctuating in the trap due to Brownian motion. The power spectrum of this is shown on the right.

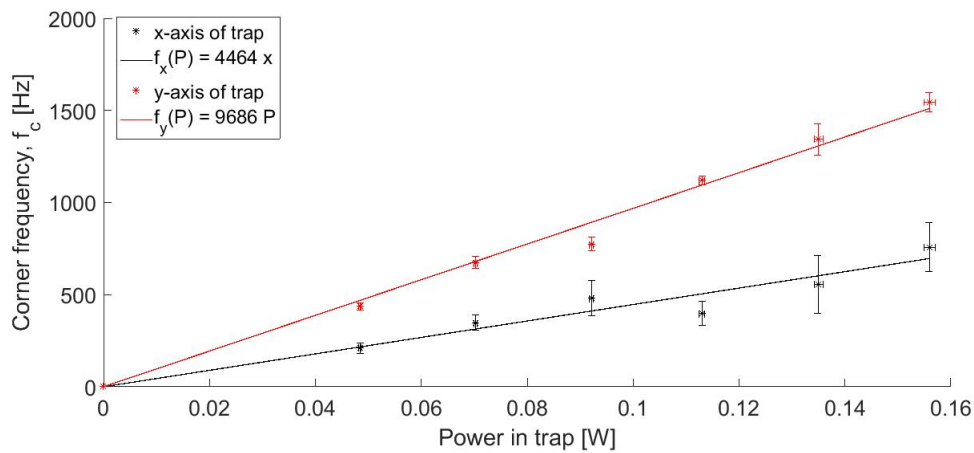


**Figure 4.5:** The corner frequency,  $f_c$ , is determined (in Hz) and plotted for various trap powers. As the power in the trap increases, the trap strength increases, and the corner frequency increases. This was done with beads of 1  $\mu\text{m}$  in diameter.

The corner frequency,  $f_c$ , measurements in  $x$  (black) and  $y$  (red) are plotted in figure 4.5 for various trapping powers. The frequencies existing in the trap at high powers reach up to a kHz. As the power in the trap increases the  $f_c$  also increases linearly as a function of the power,  $P$ , as follows,

$$f_{c_x}(P) = 4464P \quad R_x^2 = 1 \quad (4.3)$$

$$f_{c_y}(P) = 9686P \quad R_y^2 = 0.99 \quad (4.4)$$

The extracted corner frequency is used to determine the force constant from  $f_c = \frac{k}{2\pi\gamma}$ . The force calibration done for beads of a diameter of 1  $\mu\text{m}$  is shown in figure 4.6. The force constant is determined for the  $x$  (black) and the  $y$  (red) axes of the trapping plane. The measurements show picoNewton forces exerted on the 1  $\mu\text{m}$  bead in the trap. As the power in the trap increases by increasing the laser current, the forces in the trap become stronger - linearly. The linear fits in figure 4.6 as a function of the power,  $P$ , are

$$f_x(P) = 2.7 \times 10^{-4}P \quad R_x^2 = 0.93 \quad (4.5)$$

$$f_y(P) = 5.8 \times 10^{-4}P \quad R_y^2 = 0.99 \quad (4.6)$$

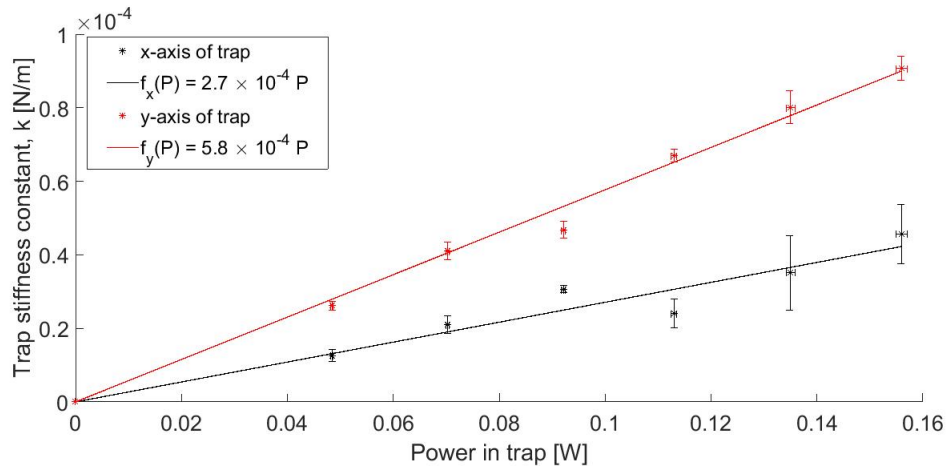


**Figure 4.6:** The force calibration for 1  $\mu\text{m}$  beads demonstrating the picoNewton forces on the bead in the trap. The force constant,  $k$ , is measured for varying values of the trapping power.

For a displacement of 0.5  $\mu\text{m}$  of the bead from the trap center, the forces on the bead are, as expected again, in the picoNewton range for particles of this micron sizes. For example, at 113 mW the force is 33 pN over a distance of 0.5  $\mu\text{m}$  along the  $y$  axis.

**Force calibration using 4 micron beads** The force calibration is also determined using beads with a larger diameter of 4  $\mu\text{m}$ . The force constant along the  $x$  axis is shown in figure 4.7 with a linear fit as a function of the power in the trap,  $P$ ,

$$f_x(P) = 2.6 \times 10^{-5} P \quad R_x^2 = 0.82 \quad (4.7)$$

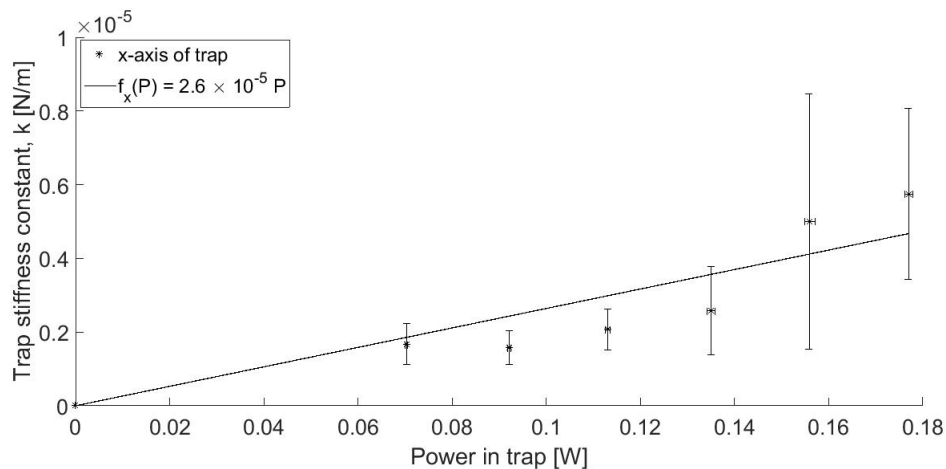


**Figure 4.7:** The trap constant of a 4  $\mu\text{m}$  bead is shown here along the  $x$  axis of the optical trap.

Taking the larger diameter into account, if the bead is displaced a distance of 2  $\mu\text{m}$  from the trap center, the force at for example 113 mW, is 5.9 pN.

For two different diameters of silica beads, the force on a micron sized particle was determined to be in the picoNewton range. The forces on the larger bead are determined to be smaller, but still in the picoNewton range. The trap is stronger for a smaller particle.

#### 4.1.1.4 Force calibration dependence on the $z$ position

The force calibration is different depending on whether the bead is trapped near the cover slide, in the center of the water droplet, or near the droplet's surface. To illustrate this, the force calibration was done for these three positions using a  $1\ \mu\text{m}$  bead. The results along only one axis in the trapping plane is shown here using the PSD method. First, the force calibration was done while holding a trapped bead close to the cover slide.

The second measurement is taken when the bead is trapped in the center of the water droplet, a significant distance away from the cover slide and droplet surface such that the two boundaries do not influence the bead.

The third  $z$  position used to measure the force calibration is when the bead in the trap is held close to the droplet surface. Again, the surface will affect the forces that act on the bead.

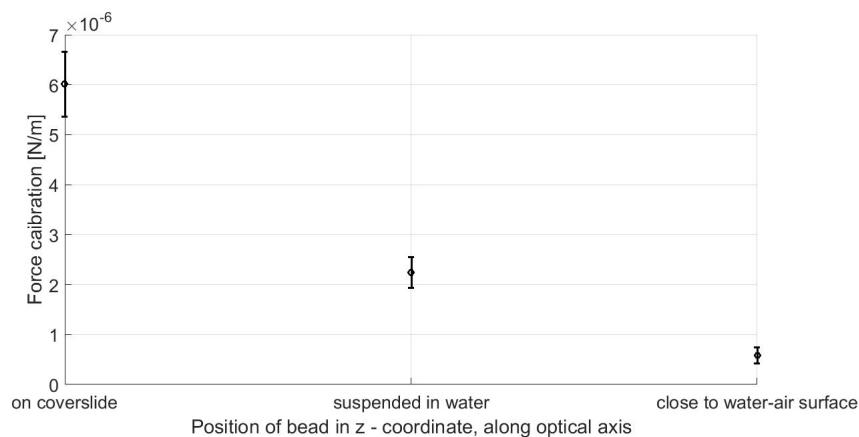


**Figure 4.8:** The force calibration is done on a  $1\ \mu\text{m}$  bead at three different  $z$  positions of the trap.

In figure 4.8, the force calibration was done for 134 mW. It is seen that the forces acting on the bead when it is close to the cover slide is more than when it is in the center of the droplet. Close to the cover slide the drag forces are larger, therefore the force required to trap the particle is also larger.

When the bead is held in the trap close to the surface of the droplet, one can see the trap is weaker, because the bead's position is no longer stationary as before. The surface boundary influences the trap strength.

As demonstrated, the position of the bead with respect to the water-glass or water-air interface, has a severe influence on the measured optical force. The bead should therefore be kept approximately in the center of the two when performing force measurements.

### 4.1.2 Measuring the forces needed to stall molecular motors using the optical tweezers

A layer of onion is placed on a cover glass slide and inserted into the optical tweezers setup. Due to the limited optical resolution of our imaging setup (from section 3.1.2 structures of  $2.19\ \mu\text{m}$  in size and possibly smaller, can be resolved) cellular structures in the onion cell, such as the filaments and microtubules, are too small to be imaged. Vesicles, however,



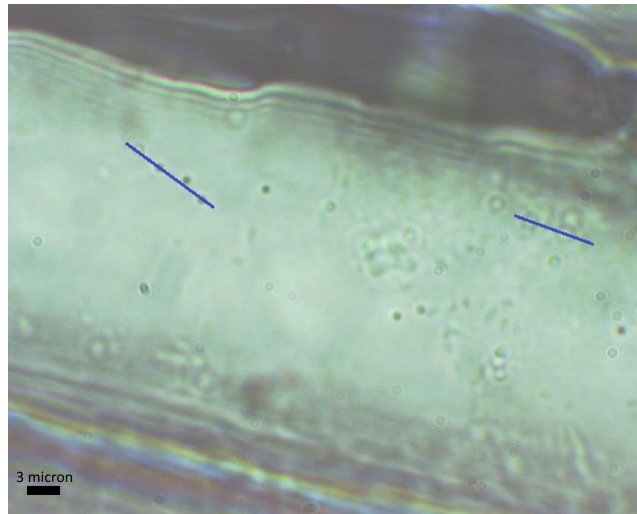


**Figure 4.9:** Vesicles transported along possible cytoskeletal structures by molecular motors are identified. The blue line indicates possible filaments, upon which multiple vesicles appear to follow the same path over time.

are identified as round spheres approximately  $0.42 \mu\text{m}$  to  $1.12 \mu\text{m}$  in diameter (measured and averaged over 50 vesicles to  $0.74 \mu\text{m}$  in diameter, standard deviation of  $0.15 \mu\text{m}$ ).

Figure 4.9 shows a single frame of a movie in which a few vesicles are seen moving in the cell. The full video can be seen at <http://hdl.handle.net/10019.1/103606>. Some of the vesicles are randomly diffusing and follow no clear path. However, vesicles transported along a path at a relatively constant speed can also be identified. These are possibly transported by myosin motors along actin filament tracks. A blue line is superimposed on two such tracks identified by the linear motion of the vesicles, figure 4.9.

The linear tracks seem to stretch across long distances in the cell. This suggests that the filaments have long persistence lengths. If the persistence length is much shorter than the length of the polymer, it means that over the length of the polymer, the polymer is more flexible than if the persistence length was longer [42, p. 110]. In general, persistence lengths indicate the flexibility of filaments or polymers. In some cells, by watching the vesicles move along linear tracks, they look as if they cross large distances in the cells. According to Ott, Magnasco, Simon, and Libchaber [62] the persistence length of actin filaments is approximately  $16.7 \mu\text{m}$ .

Using the optical tweezers, the vesicles can be trapped if the trap is strong enough, or in other words, if the laser power is high enough. This stalls the molecular motor's motion of transporting the vesicle along the filament. Decreasing the trap strength shows the vesicle continuing along the path once released from the trap. This indicates the vesicle is still attached to the motor and it is in fact the motor that is stalled. This also proves that trapping of the vesicles is a nondestructive process and the measurements do not interrupt the *in vivo* processes in the cell. This is an important property of the setup, because there is a large difference in the environments in which *in vivo* and *in vitro* measurements on the motors are performed [16]. The *in vivo* environment includes effects due to possible elastic tethering to structures in the cell and the viscous drag in the cell (when the fluid in the cell is not water as used in the force calibration).

The trap is positioned at a point along a filament. The trap strength is increased and the  $y$  component of the force required to stall the motion of the motors along the tracks are measured by measuring the trap power at which the vesicle becomes trapped, using the

trap strength to force constant ( $k_y$ ) calibration from section 4.1.1.3. The PSD calibration is used and not the equipartition theorem, because it is said to be more accurate as mentioned in section 4.1.1.2. The displacement of the vesicle by the motor was not along one particular axis,  $x$  or  $y$ . The  $y$  axis' calibration is used to determine the forces to demonstrate this idea, because the  $R^2$  value for the force calibration along the  $y$  axis is closer to one. The results are summarized in table 4.1.

	Trapping a vesicle attached to molecular motor	Trapping a randomly diffusing vesicle	Releasing a vesicle from trap
Average force [pN]	15.8	3.89	3.26
Standard deviation [pN]	3.98	2.52	4.18
Minimum [pN]	3.36	2.2	0.01
Maximum [pN]	21.9	15.0	15.0

**Table 4.1:** The stall force (component along the  $y$  axis of the trap) for vesicles transported along cell structures by molecular motors are shown here to be in the range of picoNewtons for displacements of  $0.5 \mu\text{m}$  from the trap center. The force at which the molecular motor recovers and removes the vesicle from the trap again are also shown. The average of these measurements are taken over many measurements and the standard deviation is indicated for these force measurements.

The magnitude of the force is determined across a distance of  $0.5 \mu\text{m}$ , using  $F = kx$ .  $x = 0.5 \mu\text{m}$  is chosen, because parabolic approximation of the trapping potential is valid up to displacements from the trap center up to the size of the particle's radius [14, p. 34], which is  $0.5 \mu\text{m}$ .

The trapping of vesicles is done for various vesicles, in various cells. The average stall force is 15.8 pN (standard deviation of 3.98 pN). This is the picoNewton force required to stop a molecular motor transporting a vesicle across a distance of  $0.5 \mu\text{m}$ .

The force required to stop the motion of a randomly diffusing vesicle that is not transported by a molecular motor in the cell, or traveling along any distinct path, is 3.89 pN (standard deviation of 2.52 pN). That means a larger force is required to stop the motion of a vesicle transported along by a molecular motor. This is because the motor is holding on to the vesicle and the cytoskeleton of the cell and as ATP is used the motor and vesicle move forward. The free diffusing vesicles have no attachment to a part of the cell. Therefore these vesicles require a smaller trapping force for the stochastic forces causing diffusion of the vesicle to be overcome and to trap the vesicle (no motors).

The force applied by the trap when the vesicle is released from the trap is 3.26 pN on average. This is less than half the force required to stall the motor. The trap strength when the motor continues to transport the vesicle varies greatly and the standard deviation is very large, 4.18 pN. Due to the resolution of the imaging with the white light and objectives, the filament cannot be viewed on the camera and may move while this trapping occurs. It is possible that the movement of the filaments on which the motors are attached may affect the recovery of the motion of the motor.

The range in which the results lie is very large. The forces vary greatly due to a number of reasons, the main reason being that this is a live cell and things are constantly moving. Not only must the traps  $x$  and  $y$  position be exactly in the path of the motor, but the trap's  $z$  position (height) should also be correctly aligned to ensure trapping the vesicle. This is done by changing the height of the stage such that the size of the vesicles moving in the cell are the same size as a trapped vesicle on the camera image. This would

mean that the vesicles on the track are the same height as the trap position. However, this proves difficult as the filaments constantly move. The fact that the filaments move in the  $z$  direction is evident when observing the cell for a few minutes. By viewing a constant focal plane, the paths the vesicles follow disappear and appear at different places in the cell as they move in the  $z$  axis.

**Speeds of the vesicles transported by molecular motors** Using the setup, the speeds of the vesicles were determined. Many measurements were taken and averaged over various cells and molecular motors. The motion of the vesicles are recorded on the camera and from this the speeds are determined. The temperature in the trap position when the NIR laser is off is, on average, 20.1°C.

For vesicles transported by a molecular motor, their speeds range between 1.6  $\mu\text{m/s}$  and 7.7  $\mu\text{m/s}$  if in the center of the cell, and between 2.8  $\mu\text{m/s}$  to 6.9  $\mu\text{m/s}$  if along the cell wall. It is possible that there are fewer obstructions in the motors' path when it is moving in the center of the cell and can therefore move slightly faster. If two vesicles are transported closely together (closer than twice the diameter of the vesicles), the speed decreases to ranging between 2.1  $\mu\text{m/s}$  and 3.7  $\mu\text{m/s}$ .

Many factors influence the speed of the molecular motors. The specifics of the environment is crucial. For example, the amount of ATP available will cause the speeds to differ, and temperature and the viscosity of the fluid in the cell will influence the movement of the vesicles. However, by observing the speeds at which the vesicles are transported, the literature discussed in section 2.4.1 supports the assumption that these vesicles are not transported by kinesin, but rather myosin motors [44; 47; 48].

## 4.2 Fluorescence measurements

Fluorescence measurements were completed as described in section 3.4. For a piece of a leaf, a white light image is shown in figure 4.10 (a) on the left. The dark parts of the image shows where the white light is not transmitted to the camera. To the right of this image in (b), is the leaf imaged using fluorescence, where the part that was dark before with the white light is now fluorescing as the fluorescence of chlorophyll in the leaf has a maximal emission peak between 650 nm and 700 nm [60].

Fluorescence imaging measurements of a layer of onion stained with Rhodamine 6G dye that fluoresces when excited by UV light were also conducted. On the left of figure 4.11 in (a), the brick like onion cells can be seen where the darker edges are regions where large amounts of the dye are found. The image on the right of figure 4.11 in (b) is the fluorescence image. Again as with the leaf, the fluorescing part of the sample (here the dye) is seen to contrast with the darker background.

The fluorescence of the dye in figure 4.11 is not bright, and there is poor contrast between where there is dye and not. This could be because the dye has been absorbed into the onion layer. Background fluorescence also occurs due to various reasons such as the fluorescence can scatter and be reflected through thick microscope slide. Other particles such as dust and water can also scatter and reflect the signal.

The images shown in this section were captured in a wide field geometry, where a large area of the sample is excited and imaged which generally delivers poor optical resolution. A large area of the sample is excited to fluoresce, and a section of it is imaged. A higher resolution alternative would be confocal imaging where only a small section of the sample

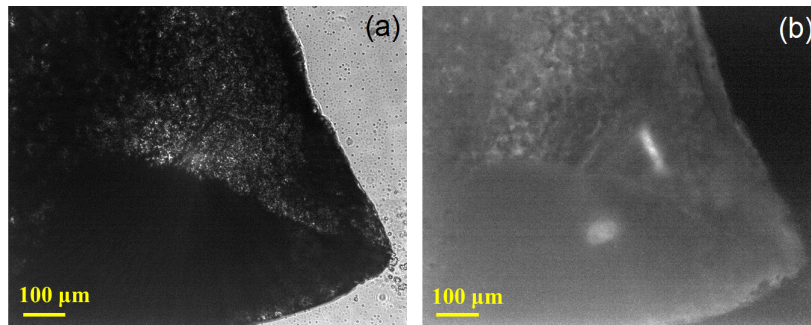


**Figure 4.10:** On the left (a) is a white light image of a piece of leaf and to the right (b) is the leaf imaged using the UV laser.

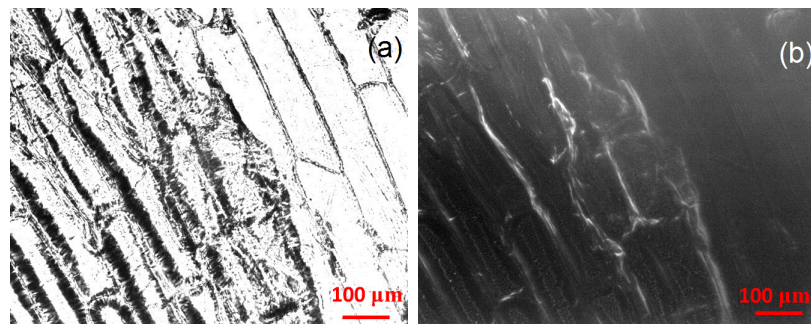


**Figure 4.11:** On the left (a) is a white light image of a layer of onion, with laser dye on the left most cells, and to the right (b) is the fluorescence image of onion stained with Rhodamine 6G.

would be allowed to fluoresce. The setup above can be expanded to not only linear microscopy but also nonlinear microscopy techniques. To do this the UV laser source for fluorescence can be replaced by a supercontinuum (SC) source. The supercontinuum pulses are short in time, therefore preventing photodamage to the samples and also of high intensities such as to stimulate nonlinear processes in a portion of the focal region only - increasing image resolution. In a confocal geometry, the supercontinuum beam will have to be scanned across the sample (by, for example, galvo mirrors) to image the signal from the nonlinear process at different positions on the sample, a raster scanning technique.

### 4.3 Ptychography

In this section, the ptychographic algorithms will be implemented. First, images will be used to represent the amplitude and phase of the transmitted light through samples to demonstrate the PIE and ePIE algorithms. Once the algorithms are shown successful, the results of experimental diffraction images can be used to reconstruct a sample using the setup from chapter 3.5.

#### 4.3.1 Simulation results

Using simulations, the algorithms can first be tested using known samples (given pictures). This eliminates factors introduced by the physical experiment to show the effectiveness of the algorithms. The PIE and ePIE algorithms were implemented in Matlab. The code we wrote can be found in Appendix A.

### 4.3.1.1 The ptychographic iterative engine (PIE)

An image of a light house is used to represent the sample's (or object's) amplitude ( $A$ ) and an image of arrow is used to represent the phase ( $\phi$ ) of the sample, figure 4.12. The sample's electric field description is  $Ae^{i\phi}$ , where both amplitude and phase are two dimensional matrices. PIE is a one-to-one imaging algorithm that will use the  $256 \times 256$  pixel images in figure 4.12.

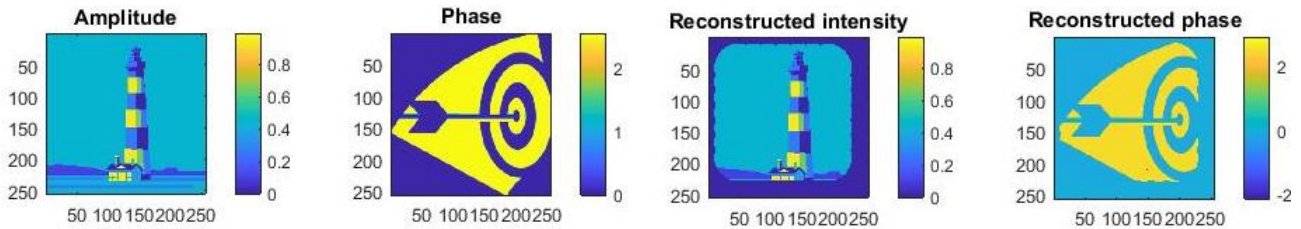


**Figure 4.12:** The sample for the simulation is chosen as a light house image (for the amplitude) and an arrow image (for the phase). These  $256 \times 256$  pixel images make up the sample that will be reconstructed with PIE and consequently, imaged.

**Figure 4.13:** The reconstructed amplitude (on the left) and relative phase (on the right) is shown after 30 iterations of the PIE algorithm. This one-to-one reconstruction is similar to the original sample ( $256 \times 256$  pixel images) in figure 4.12.

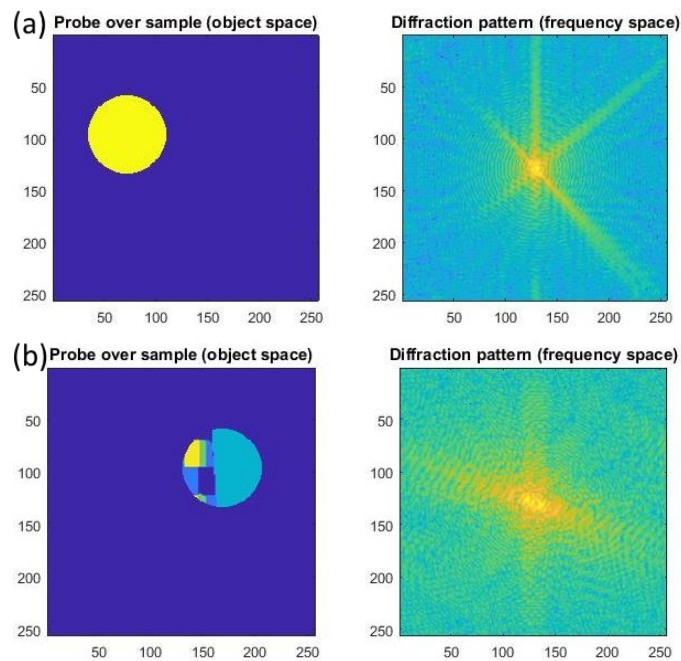


**Figure 4.14:** At a certain probe position (a) and (b), the pinhole is located over a part of the sample (images on the left of (a) and (b)), and light through the pinhole and sample will give a diffraction pattern as simulated on the right of (a) and (b). For different probe positions, different diffraction patterns are measured.

The probe is chosen as a circular flat top (with zero relative phase). After 30 iterations of PIE, the reconstruction is not changing considerably anymore and the simulation is stopped. A probe size of 75 pixels in radius is chosen with an overlap 80% when shifting the probe by 24 pixels to the neighbouring position. For this simulation the probe scans

the sample making a  $7 \times 7$  grid of positions across the sample using  $\alpha = 0.001$  and  $\beta = 0.95$ .

The diffraction patterns used include the high orders of diffraction, thus giving a large angular spectrum. Examples of the diffraction patterns used in the PIE simulation are shown on the right in figure 4.14. The images on the left, show the probe overlapping the amplitude matrix in object space. The corresponding diffraction pattern created when taking the fast Fourier transform (FFT) in two dimensions, shown on the right in frequency space. For display purposes only, the logarithm of the image of the diffraction pattern is shown to emphasize weaker pixel intensities of the diffraction. Seeing that the higher orders of diffraction are included in the simulation, high resolution reconstructed images are expected. In figure 4.14, two probe positions are shown in (a) and (b) to illustrate the changing diffraction pattern detected as the probe scans the sample.

The results after 30 PIE iterations are shown in figure 4.13, the amplitude on the left and relative phase on the right. The phase difference reconstructed, between the blue and yellow parts in the image representing the phase, is  $0.82\pi$ . This is the same relative difference between the arrow and background as in the original sample's phase (even though the colours are not the same, the difference in phase is).

#### 4.3.1.2 The extended Ptychographic Iterative Engine (ePIE)

For the PIE algorithm above, it was assumed that the probe has a flat top amplitude (normalized to 1) and no phase. However, if the probe has a different structured profile in amplitude or in phase, the ePIE algorithm can reconstruct the object, as well as the probe in amplitude and relative phase to a reasonable degree. The images used as the sample's and probe's associated amplitude and phase of the transmitted light are shown in figure 4.15. A probe of flat top (maximum pixel intensity of 0.5) is chosen for the amplitude, but the probe's relative phase is inserted as the image of a spiral with a varying gradient. This is what should be reconstructed using the algorithm.

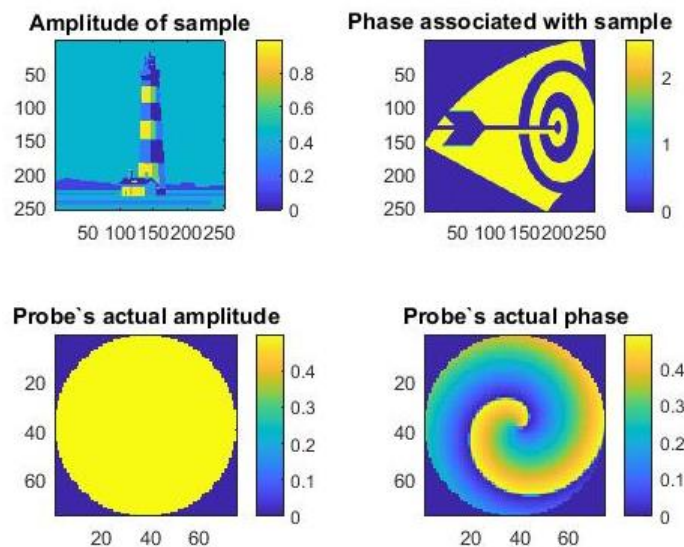


**Figure 4.15:** The images used as the sample's amplitude (left) and associated relative phase (right) are shown in the first row. The second row is the probe, in amplitude (left) and associated relative phase (right), used to create the simulated diffraction patterns. These are the object and probe properties the ePIE algorithm will reconstruct.

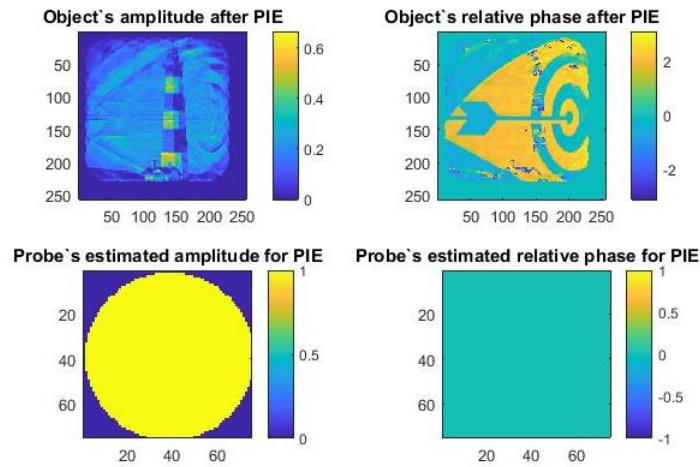


**Figure 4.16:** The first row show the reconstruction of the object in amplitude (left) and associated relative phase (right) after two PIE iterations. The second row shows the probe estimate used in the PIE iteration - which is not updated.

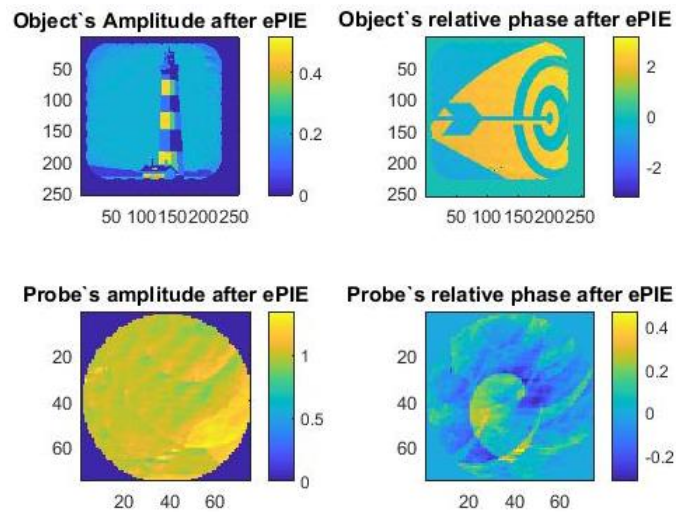


**Figure 4.17:** The object is reconstructed using 350 iterations of the ePIE algorithm, in amplitude (left) and associated relative phase (right). The probe is also updated and shown in the second row. This reconstructed probe can be compared to the actual probe, shown figure 4.15.

For the results in figures 4.16 and 4.17, a probe size of 75 pixels in radius is used. Again, a  $7 \times 7$  grid of probe spots is created with a probe step size of 24 pixels. As in PIE,  $\alpha = 0.001$ ,  $\beta = 0.95$  and  $\gamma = 0.95$ .

Figure 4.16 shows the results after the initial 2 PIE iterations completed before the ePIE starts to reconstruct the probe along side the object. These initial PIE iterations are completed to give the ePIE algorithm a more accurate initial guess than a zero matrix. The first row of images in figure 4.16 shows the amplitude and phase of the sample after the PIE iterations. This is what will be used as a starting point for the ePIE. The probe estimate is shown in the second row of figure 4.16. For the PIE iterations, the probe is estimated to be have a flat top amplitude (maximum pixel intensity of 1) and no relative phase.

350 ePIE iterations are completed using the initial amplitude and phase estimates shown in figure 4.16. These initial estimates for the object and probe and will be updated with ePIE iterations. The reconstruction after 350 ePIE iterations are shown in figure 4.17.

The first row of figure 4.17 shows the object's reconstructed in amplitude (left) and associated phase (right). The lighthouse and arrow can be seen reconstructed in the figures as the object, or sample.

The updated probe is shown in the second row of 4.17. The probe's amplitude (initially flat top normalized to one), still has a large relative phase difference to the background, even though it has not reconstructed the probe normalized to 0.5. It is also no longer completely flat at a pixel intensity of 1. Updating the probe has decreased the pixel intensity as expected (expect the amplitude to be at a pixel intensity of 0.5). The phase of the probe is also updated to show the spiral's structures expected as in the actual probe, figure 4.15.

There exists some amount of cross talk between the amplitude and phase images. This was also noted by Maiden and Rodenburg [51] in their reconstructions.

**Quantifying the convergence of the reconstruction** The difference function is calculated with equation (2.35) for the object after every PIE and ePIE iteration and plotted, figure 4.18. After a certain amount of iterations, the image is not updated significantly any more. The difference function,  $\sigma$ , (the average change in the absolute value of the pixels across the image, subtracted from that of the previous iteration) calculated is plotted and is seen to decrease as algorithm runs through the iterations. After some time  $\sigma$  is relatively small. This means that the reconstruction is not changing as much anymore as initially and is converging to a certain amplitude and phase of the object.

Initially  $\sigma$  decreases in large steps, as in the PIE graph. For the ePIE,  $\sigma$  decreases rapidly from  $2.422 \times 10^5$  after approximately only 20 iterations and the object can be recognized, but after this is it still decreasing and only reaches 18.97 after 350 iterations. After 350 iterations the change between iterations no longer significantly updates the object and the algorithm can be terminated, the image has been reconstructed.

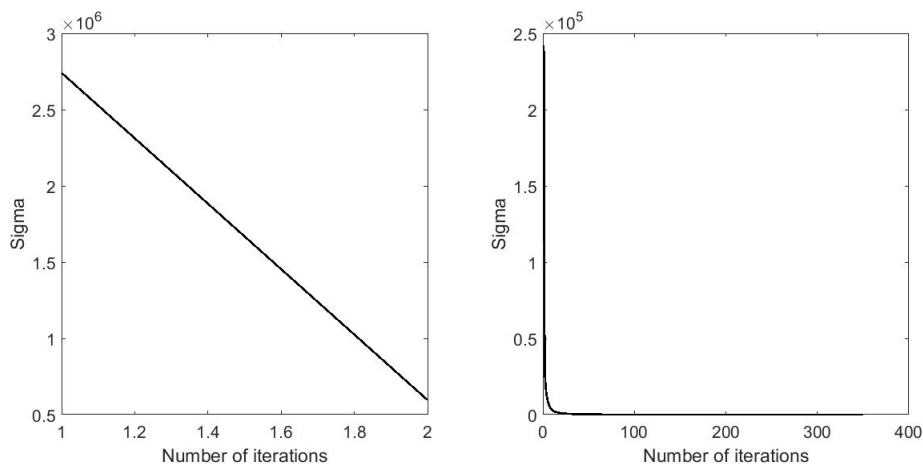


**Figure 4.18:** The difference function,  $\sigma$ , is plotted here for two PIE iterations (left) and 350 ePIE iterations (right) respectively. During the reconstruction, the average change in the absolute value of the pixels across the image is subtracted from that of the previous iteration.



In this section the algorithms of PIE and ePIE are shown to reconstruct the transmitted light's amplitude and relative phase as it passed through a sample. These algorithms can therefore be applied to physical systems where the assumptions made in the simulations are adhered to, for example, that the redundancy requirement is met.

### 4.3.2 Experimental results using the PIE algorithm

The PIE algorithm was implemented to image a cellulose acetate sample with one corner. Figure 4.19 shows a white light image of the sample on a CMOS detector. The probe is assumed to have a flat top amplitude (normalized to one) and no relative phase.

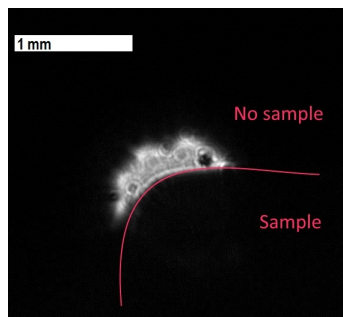


**Figure 4.19:** A cellulose acetate sample is cut into a rounded corner and imaged using the white light LED and CMOS camera in the ptychography setup. This is the sample seen reconstructed using the PIE algorithm.

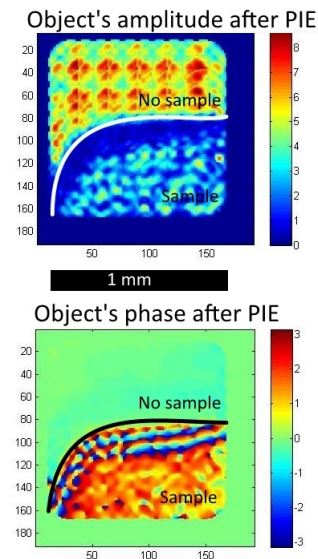


**Figure 4.20:** After 100 PIE iterations, the associated amplitude and relative phase of transmitted light is reconstructed to image the corner of the cellulose acetate sample.

**Reconstruction using PIE algorithm** The results of the reconstruction after 100 PIE iterations is shown in figure 4.20. In all the following reconstructions of PIE  $\alpha = 0.001$  and  $\beta = 0.5$  was used.

Referring to the reconstruction in figure 4.20, the top image represents the amplitude of the transmitted light. In places where the light is reflected, scattered or absorbed by the cellulose acetate sample, there is a relatively smooth amplitude of the light transmitted compared to where there is no sample (cellulose acetate). The image below shows the relative phase of the transmitted light. Again, there is a difference between where the light passes through the sample to where there is no sample. This indicates the relative phase change of the light transmitted to the detector, allowing for a reconstruction of the relative phase of the sample.

In the amplitude reconstruction, a periodic structure is seen to exist in the reconstruction. This can be attributed to the periodic probe shifts that are not varied in magnitude here [51].

To improve the reconstruction quality and give the resulting images seen in figure 4.20, modifications are made to the images before the PIE algorithm starts. What follows is a

list of improvements made to the ptychographic algorithms in the previous sections that correct for the experimental, physical limitations imposed on the resolution and quality of the reconstruction. For a few of them, the effect of removing the modification from the code is shown in figures 4.21 to 4.23.

- At every probe position, five diffraction pattern images are taken and the average of these images are used.
- Before starting the measurements with the sample, a background signal is measured by taking an image with no sample and no illumination (again the average over five images is used). This average background is subtracted from each image measured. If no background were subtracted, (but all other modifications applied), the reconstruction, after 100 PIE iterations, would be as seen in figure 4.21. The corner of the sample (cellulose acetate) is still relatively clear, but the quality of the reconstruction is not smooth across the constant amplitude regions as with the background subtraction.
- A region around the center of the diffraction is cut out (cut out size of 350 pixels used here in each direction). The images captured by the CMOS sensor are very large (1280 by 1024 pixels). Using large images increase the computation time of the code. However, a large border at the boundary of the image does not contain needed information. To reduce the amount of redundant pixels in the images, the images are cut out and made smaller.
- Pixel noise is subtracted from the images by averaging over the pixel intensity of a region on the outer edge of the images (a region with out large intensity diffraction orders). This averaged pixel intensity is subtracted across all pixels of the images. Note, it is necessary to make sure that all negative pixel values (pixels with a negative intensity value not between zero and 255), after the subtraction, are set to zero. If the pixel noise is not removed, (but all other modifications applied), the reconstruction, after 100 PIE iterations, would be as seen in figure 4.22.
- To reduce the risk of discontinuities and creating artifacts or periodic structures after Fourier transformations are applied, the image is zero padded along each of the four sides. If the images were not zero padded, (but all other modifications applied), the reconstruction, after 100 PIE iterations, would be as seen in figure 4.23.
- Lastly, in the PIE algorithm, for each even and odd iteration, the probe moves first horizontal and then vertical, and vice verse for the odd number of iterations.

If none of these modifications are put into effect, the reconstruction using 100 iterations of PIE is shown in figure 4.24. The reconstruction shown in figure 4.20 is of much better quality proving that these improvements to the code are justified. The images captured therefore require some adjusting before implementing the PIE algorithm such as removing background or pixel noise, or adding a border of zeroes for example.

After applying the image processing mentioned above, in both the amplitude and phase reconstruction, the corner of the cellulose acetate sample is clearly visible, showing that this setup can image a sample using the ptychographic (PIE) algorithm. In the reconstruction the overall structure of the image can be seen and it resembles that of the white light image in figure 4.19.

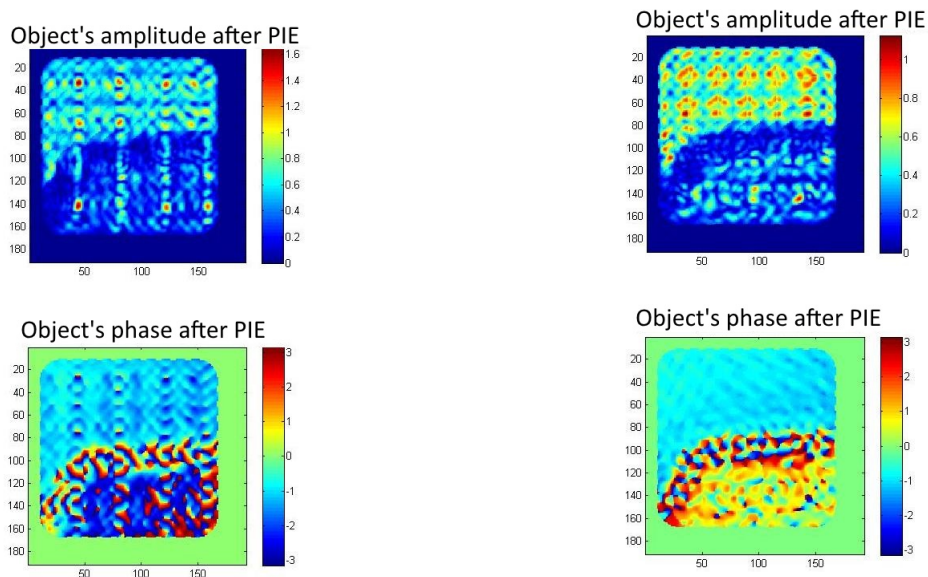


**Figure 4.21:** If no background is subtracted, the reconstruction of the associated amplitude and relative phase of the cellulose acetate sample after 100 PIE iterations is shown.

**Figure 4.22:** The reconstruction of the associated amplitude and relative phase of the sample (cellulose acetate) is shown where the pixel noise is not averaged and subtracted from the images.

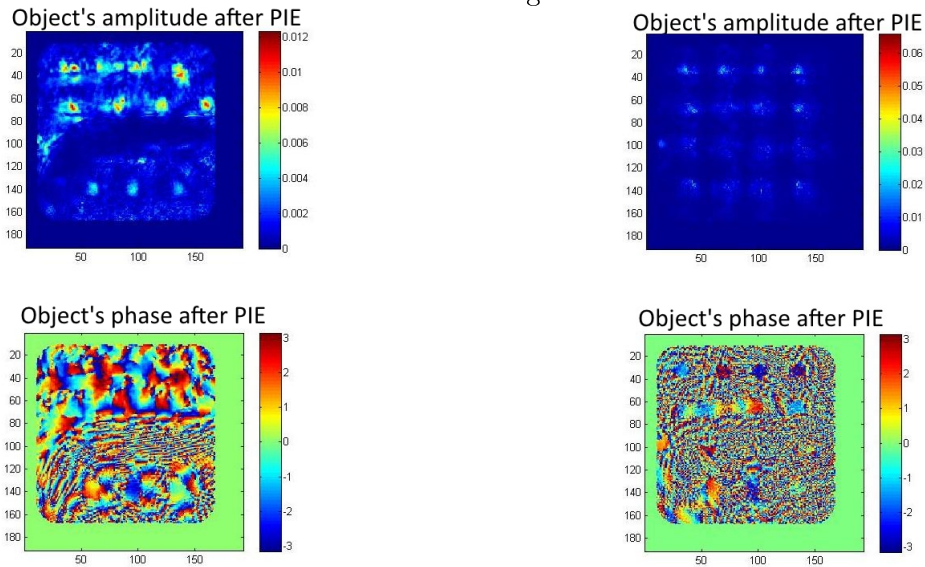


**Figure 4.23:** If the image is not zero-padded along the borders, the reconstruction of the associated amplitude and relative phase is shown. The outline of the sample (cellulose acetate) is slightly visible, but it is not a clear image.

**Figure 4.24:** If the images captured are not changed at all to improve the quality, the reconstruction is poor and the sample (cellulose acetate) is not imaged clearly at all compared to 4.20.

# Chapter 5

## Summary

Over all, different components of a multimodal microscopy setup were investigated in this work, with the focus on optical tweezing. This included the construction and calibration of an optical tweezers, and applying the optical tweezers to study biological samples. Once the optical tweezers setup was built and characterized, the possible integration of the optical tweezers with a multimodal microscopy setup was discussed. Another advanced imaging technique discussed in this work, was ptychography and ptychographic iterative engines.

The optical tweezers setup involved the trapping of silica beads by focusing a near infrared laser with a high numerical aperture lens. The trapping plane was imaged using white light wide field imaging, and the particle's position was detected using a quadrant photodiode detector. Set up of the optical tweezers also included calibrating the piezo translation stage displacements and power in the trap; sample preparation; and determining the resolution of the images captured with the white light source.

Once set up, the optical tweezers were used to trap and tweeze  $1\ \mu\text{m}$  and  $4\ \mu\text{m}$  silica beads suspended in water. The trapped beads could be translated throughout the sample in three dimensions. The optical tweezers was then characterized by determining the restoring forces applied to a trapped bead. This was done by determining the trap stiffness constant at various trap powers. Since the trap applies an approximately linear restoring force on particles displaced from the trap center, by finding the trap stiffness constant, the trap forces could be determined. It was found that the trap strength increases linearly as the trapping power increases. The forces that the trap exerts on  $1\ \mu\text{m}$  silica beads suspended in water were determined to be on the order of picoNewtons.

As an example of an application of the optical tweezers, the forces required to stall the movement of molecular motors along their predefined tracks in onion cells were determined. This was done by trapping vesicles transported by molecular motors along the cytoskeleton in a cell. Using the trap stiffness constant calibration mentioned above for  $1\ \mu\text{m}$  beads in water, it was found that the forces needed to stall these molecular motors are in the order of picoNewtons (agreeing with literature). These trapping forces were also compared to the forces needed to trap a freely diffusing vesicle in a cell. The trapping forces in the free vesicle case was found to be approximately four times less.

Optical tweezing proves useful in not only spatial manipulation of a sample, but also in studying intracellular forces in a biological system. Integrating the optical tweezers into a multiphoton microscopy setup would be the next step in future work. For example, in this work, wide field imaging with fluorescence was discussed as an extension to the optical tweezers setup to allow for simultaneous optical tweezing and imaging of the sample.

Another aspect of advanced microscopy looked at in this work was ptychography. Ptychography yields information about the amplitude and phase of the sample. This, and the fact that ptychography is a form of label-free imaging, are two advantages of imaging using the ptychographic algorithms such as those discussed in this work.

The ptychographic iterative engine (PIE), and an extension to the PIE - the extended ptychographic iterative engine (ePIE) - algorithms were implemented in this work. Simulations were completed using these algorithms and samples could be reconstructed to a reasonable degree. A setup for ptychography was built and a sample (cellulose acetate) was then imaged using the PIE algorithm. The sample was reconstructed with a relatively high level of success only after the diffraction images measured were computationally enhanced, for example, by reducing the background noise. Future work will entail expanding this to experimental results using the ePIE algorithm as well.

Multiphoton microscopy is inherently confocal and can yield resolution up to that of confocal microscopy, and even slightly better. The integration of the optical tweezers to the microscopy setup adds an extra dimension of accessibility to the sample. Ptychography, although requiring a different setup, is also an advanced imaging technique. This work gave insight into these different components, with a multimodal microscopy setup in mind for the future.

# Appendices

# Appendix A

## Ptychography code

The following is the code used in the ptychography sections to run the simulations and reconstruct the sample imaged experimentally. This code was written for this project based on algorithms found in literature, for example in [51] and [52].

### A.1 PIE

This code was used in simulating the PIE results in section 4.3.1.1:

```

1 clear all;
2 %% initialize variables
3 col = 7; % number of probe positions in x and y
4 row = 7;
5 beta = 0.95; % weighting of feedback in PIE
6 alpha = 0.001; % in update function to prevent \0 error
7 iter = 0; % ePIE iterations
8 iterPIE = 30; %conventional PIE iterations
9 %% "sample"
10 amplitude = double(rgb2gray(imread('lighthouse.png')));
11 phase = double(rgb2gray(imread('arrow.png')));
12 amplitude_norm = amplitude./256; %normalize the amplitude and phase
13 phase_norm = 2*pi* phase ./ 256;
14 f = amplitude_norm.*exp(1i.*phase_norm);
15 figure(1) % display "sample"
16 subplot(1,2,1)
17 imagesc(amplitude_norm)
18 axis image
19 title("Amplitude")
20 colorbar
21 subplot(1,2,2)
22 imagesc(phase_norm)
23 axis image
24 title("Phase")
25 colorbar
26
27 %% Make PROBE
28 % Make circular probe and calculate FWHM
29 % [ FWHM = (sigma)*2 sqrt(2 ln2)]
30 spotsize = 75; % probe size
31 FWHM = spotsize/2.355;
32 F = fspecial('gaussian', spotsize, FWHM);
33 F = F./max(max(F)); % normalize
34 I = find(F > 0.5); % make it flat top
35 I2 = find(F <= 0.5);
36 F(I) = 1; % set all values of the gaussian above half to 1
37 F(I2) = 0; % set all values of the gaussian below half to 0
38
39 %% Probe movement across sample
40 micron_step_exper = 24; % step size of probe shift
41 start_P_pos = 10; % to start the probe on initial guess (away from border)
42 P_shift = micron_step_exper; %distance probe moves in pixels
43 end_x = (start_P_pos + row*P_shift) - P_shift; %last probe position in x

```

```

44 end_y = (start_P_pos + col*P_shift)- P_shift; %last probe position in y
45 % shift probe, make matrices where probe is at all the different positions
46 for x_pos = start_P_pos : P_shift : end_x
47     for y_pos = start_P_pos : P_shift : end_y
48         % Create the probe matrix by looping through probe spots and
49         % add the value of the probe to the empty matrix, L,
50         % of the correct image size.
51
52         % Initialize an empty matrix (image) of the same size as the probe
53         % measured for probe to move across
54         L = zeros(size(f,1), size(f,2) );
55         %move probe across empty matrix making a cell of matrices with the
56         % various probe positions on.
57         for k = 1 : spotsize
58             for l = 1 : spotsize
59                 L(k + x_pos, l + y_pos) = L(k + x_pos, l + y_pos) + F(k, l);
60             end
61         end
62         %find center of probe spot
63         x_loc = round(((x_pos - start_P_pos))/P_shift +1);
64         y_loc = round(((y_pos - start_P_pos))/P_shift +1);
65         L_store{x_loc, y_loc} = L; % store probe positions
66
67         %first convolute with probe, then take to Fourier space
68         images_probe_conv_objectspace = (f.*L);
69         images_diff_E = fftshift(fft2(fftshift(images_probe_conv_objectspace)));
70         images_diff = images_diff_E.^2; % square for I only measured
71
72         %store diffraction at various probe positions in cell
73         images{x_loc, y_loc} = images_diff;
74
75         % figure(2) %image as loops through
76         % subplot(1,2,1)
77         % imagesc(abs(images_probe_conv_objectspace))
78         % title("Probe over sample (object space)")
79         % axis image
80         % subplot(1,2,2)
81         % imagesc(log(abs(images{x_loc, y_loc})))
82         % axis image
83         % title("Diffraction pattern (frequency space)")
84         % pause(0.5)
85     end
86 end
87
88 %% Initial guess in object space
89 Object = complex(zeros(size(f,1)), zeros(size(f,2))); %Efield in object space
90 % or use a random initial guess
91 % Object = rand(size(f));
92
93 %% PIE
94 for m = 1:iterPIE
95     %Iterate in a raster scanning left to right then down or resample the
96     %diffraction cell at random positions with
97     % for i = round(rand*(row-0.1)+0.5)
98     % but no resampling:
99     for i = 1:row %round(rand*(row-0.1)+0.5)
100         for j = 1: col %round(rand*(col-0.1)+0.5)
101             % for each probe position:
102             % make Efield intensity
103             Object_E = Object;
104             %initial guess at probe position in object space
105             Object_guess_objectspace = Object_E.*L_store{i, j};
106             Object_guess_Fourierspace = fftshift(fft2(fftshift(Object_guess_objectspace)
107             ));
108             % phase of approx guess
109             p = angle(Object_guess_Fourierspace);
110             % update E with measured I
111             Object_update_Fourierspace = sqrt(abs(images{i, j})).*exp(sqrt(-1).*p);
112             %updated E field in object space
113             Object_update_objectspace = fftshift(iff2(fftshift(
114                 Object_update_Fourierspace)));
115             Err = Object_update_objectspace - Object_guess_objectspace;
116             update_function_Objectspace = (conj(L_store{i, j})./max(max(abs...
117                 (L_store{i, j}))))).*abs(L_store{i, j})./...

```



```

116         (conj(L_store{i,j})*L_store{i,j}+alpha);
117     Object = Object + beta .* update_function_Objectspace .* Err;
118     % figure(3) %image as it updates
119     % subplot(121)
120     % imagesc(abs(Object));
121     % title('updating objects amplitude')
122     % axis image
123     % colorbar
124     % subplot(122)
125     % imagesc(angle(Object));
126     % title('updating objects phase')
127     % axis image
128     % colorbar
129     % pause(0.01);
130     end
131 end
132 %%store error
133 erroraveraged(m) = sum(Err(:))/N;
134 %%display image as it updates
135 % figure(2)
136 % subplot(121)
137 % imagesc(abs(Object));
138 % title('updating objects amplitude')
139 % axis image
140 % colorbar
141 % subplot(122)
142 % imagesc(angle(Object));
143 % title('updating objects phase')
144 % axis image
145 % colorbar
146 % pause(0.05);
147
148 end
149 %% store amplitude and phase of PIE reconstruction
150 Object_PIE = Object;
151 %% Sum squared error after PIE
152 Err_PIE = sum(Err(:))/(256*256);
153 % figure(4)
154 % plot(1:length(erroraveraged), abs(erroraveraged));
155 % title('Error averaged overall pixels (SSE)');
156 % xlabel('number of iterations');
157 % ylabel('absolute error');
158
159 %% Display PIE reconstruction
160 figure(3)
161 subplot(121)
162 imagesc(abs(Object))
163 axis image
164 colorbar
165 title('Reconstructed intensity')
166 subplot(122)
167 imagesc((angle((Object))))
168 title('Reconstructed phase')
169 axis image
170 colorbar

```

## A.2 ePIE

This code was used in simulating the ePIE results in section 4.3.1.2:

```

1 clear all;
2 %% initialize variables
3 col = 7; % number of probe positions in x and y
4 row = 7;
5 beta = 0.9; % weighting of feedback in PIE
6 alpha = 0.001; % in update function to prevent \0 error
7 gamma = 0.9; % weighting of feedback in ePIE
8 iter_ePIE = 350; %ePIE iterations
9 iter_PIE = 2; %conventional PIE iterations
10 %% "sample"
11 amplitude = double(rgb2gray(imread('lighthouse.png')));

```

```

12 phase = double(rgb2gray(imread('arrow.png')));
13 amplitude_norm = amplitude ./ 256; % normalize the amplitude
14 phase_norm = 2*pi* phase ./ 256; % normalize the phase
15 f = amplitude_norm.*exp(1i.*phase_norm); % normalised image from input
16 N = size(f, 1)*size(f,2); % number of pixels for SSE
17
18 %% Initialize probe
19 % Make circular probe (with Gaussian) and calculate FWHM
20 % FWHM [ FWHM = (sigma)*2 sqrt(2 ln2)]
21 spotsize = 75; % radius
22 FWHM = spotsize/2.355;
23 Probe = fspecial('gaussian', spotsize, FWHM);
24 Probe = Probe./max(max(Probe)); % normalize and half - smaller gradient
25 % Making probe flat top with structured phase
26 I1 = find(Probe>0.5); % to make it flat top
27 I21 = find(Probe<=0.5);
28 Probe(I1) = 0.5; % set all values of the gaussian above half to 1
29 Probe(I21) = 0; % set all values of the gaussian below half to 0
30 % Probe_amp = double(rgb2gray(imread('roofs75x75.png')))./256;
31 % Give the probe phase in the form of an image
32 Probe_phase = Probe.*double(rgb2gray(imread('spiral75x75.png')))./256;
33 Probe = Probe.*exp(1i.*Probe_phase);
34
35 %%%%%%%%%%%%%%%%%%%%%%%%%%%%%%%%%%%%%%%%%%%%%%%%%%%%%%%%%%%%%%%%%%%%%%%%%
36 % Simulate measuring diffraction patterns
37 %%%%%%%%%%%%%%%%%%%%%%%%%%%%%%%%%%%%%%%%%%%%%%%%%%%%%%%%%%%%%%%%%%%%%%%%%
38 %% Probe movement across sample
39 micron_step_exper = 24; % step size in experiment in micron
40 start_P_pos = 10; % to start the probe on initial guess (away from border)
41 P_shift = micron_step_exper; % distance probe moves in pixels
42 end_x = (start_P_pos + row*P_shift) - P_shift; % last probe position in x
43 end_y = (start_P_pos + col*P_shift) - P_shift; % last probe position in y
44 % Shift probe, make matrices where probe is at all the different positions
45
46 for x_pos = start_P_pos : P_shift : end_x
47     for y_pos = start_P_pos : P_shift : end_y
48         % Create the probe matrix by looping through probe spots and
49         % add the value of the probe to the empty matrix, L
50         % of the correct image size.
51
52         % Initialize an empty matrix (image) of the same size as the probe
53         % measured for probe to move across
54         L = zeros(size(f,1), size(f,2) );
55         % move probe across empty matrix making a cell of matrices with the
56         % various probe positions on.
57         for k = 1 : spotsize
58             for l = 1 : spotsize
59                 L(k + x_pos, l + y_pos) = L(k + x_pos, l + y_pos) + Probe(k, l);
60             end
61         end
62         % find center of probe spot
63         x_loc = round(((x_pos - start_P_pos))/P_shift + 1);
64         y_loc = round(((y_pos - start_P_pos))/P_shift + 1);
65         L_store_diffimages{x_loc, y_loc} = L; % store probe positions
66
67         %first convolute with probe, then take to Fourier space
68         images_probe_conv_objectspace = (f.*L);
69         images_diff_E = fftshift(fft2(fftshift(images_probe_conv_objectspace)));
70         images_diff = images_diff_E.^2; % square for I only measured
71
72         %store diffraction at various probe positions in cell
73         images{x_loc, y_loc} = images_diff;
74
75         %% display diffraction patterns as sample moves through probe
76         % figure(2)
77         % subplot(1,2,1)
78         % imagesc(abs(images_probe_conv_objectspace));
79         % axis image
80         % title('Probe over sample (object space)');
81         % subplot(1,2,2)
82         % imagesc(abs(images{x_loc, y_loc}))
83         % axis image
84         % title('Diffraction patterns (frequency space)')
85         % pause(0.5)

```

```

86     end
87 end
88
89 %%%%%%%%%%%%%%%%%%%%%%%%%%%%%%%%%%%%%%%%%%%%%%%%%%%%%%%%%%%%%%%%%%%%%%%%%
90                               % PIE
91 %%%%%%%%%%%%%%%%%%%%%%%%%%%%%%%%%%%%%%%%%%%%%%%%%%%%%%%%%%%%%%%%%%%%%%%%%
92
93 %% create probe spots with flat top to convolve with initial guess
94 % use flat top probe with no phase in PIE
95 Probe_F = fspecial('gaussian', spotsize, FWHM);
96 Probe_F = Probe_F./max(max(Probe_F)); % normalize and half - smaller gradient
97 Probe_PIE = Probe_F;
98 I = find(Probe_PIE>0.5); %to make it flat top
99 I2 = find(Probe_PIE<=0.5);
100 Probe_PIE(I) = 1; % set all values of the gaussian above half to 1
101 Probe_PIE(I2) = 0; % set all values of the gaussian below half to 0
102
103 for x_pos = start_P_pos : P_shift : end_x
104     for y_pos = start_P_pos : P_shift : end_y
105         % Create the probe matrix by looping through probe spots and
106         % add the value of the probe to the empty matrix, L,
107         % of the correct image size.
108
109         % initialize an empty matrix (image) of the same size as the probe
110         % measured for probe to move on
111         L = zeros(size(f,1), size(f,2) );
112         %move probe across empty matrix making a cell of matrices with the
113         % various probe positions on
114         for k = 1 : spotsize
115             for l = 1 : spotsize
116                 L(k + x_pos, l + y_pos) = L(k + x_pos, l + y_pos) + Probe_PIE(k,l);
117             end
118         end
119         % find center of probe spot
120         x_loc = round(((x_pos - start_P_pos))/P_shift + 1);
121         y_loc = round(((y_pos - start_P_pos))/P_shift + 1);
122         L_store_PIE{x_loc, y_loc} = L; % store probe position for PIE
123     end
124 end
125
126 %% Initial guess in object space
127 Object = complex(zeros(size(f,1)), zeros(size(f,2))); %Efield in object space
128 % or use a random initial guess
129 % Object = rand(size(f));
130
131 %% PIE (used flat top probe and no phase, probe_PIE, stored in L_store_PIE)
132 for m = 1:iter_PIE
133     %iterate in a raster scanning left to right then down or resample the
134     %diffraction cell at random positions with
135     % for i = round(rand*(row-0.1)+0.5)
136     for i = 1:row % round(rand*(row-0.1)+0.5)
137         for j = 1:col %round(rand*(col-0.1)+0.5)
138             % for each probe position
139             % make Efield intensity
140             Object_E = Object;
141             %initial guess at probe position in object space
142             Object_guess_objectspace = Object_E.*L_store_PIE{i,j};
143             Object_guess_Fourierspace = fftshift(fft2(fftshift(Object_guess_objectspace)
144             ));
145             % phase of approx
146             p = angle(Object_guess_Fourierspace);
147             %update E with measured I
148             Object_update_Fourierspace = sqrt(abs(images{i,j})).*exp(sqrt(-1).*p);
149             %SSE in diffraction plane
150             SSE_E_f = (abs(Object_update_Fourierspace).^2 - abs(Object_guess_Fourierspace
151             ).^2).^2;
152             %updated E field in object space
153             Object_update_objectspace = fftshift(iff2(fftshift(
154             Object_update_Fourierspace)));
155             Err = Object_update_objectspace - Object_guess_objectspace;
156             update_function_Objectspace = (conj(L_store_PIE{i,j})./max(max(abs...
157             (L_store_PIE{i,j})))).*abs(L_store_PIE{i,j})./...
158             (conj(L_store_PIE{i,j})*L_store_PIE{i,j} + alpha);
159             Object = Object + beta .* update_function_Objectspace .* Err;

```

```

157 %         SSE_E = (abs(Object_update_objectspace).^2 - abs(Object_guess_objectspace)
        .^2).^2;
158 %         %image as it updates
159 %         figure(3)
160 %         subplot(2,2,1)
161 %         imagesc(abs(Object))
162 %         axis image
163 %         colorbar
164 %         title('updating objects amplitude')
165 %         subplot(2,2,2)
166 %         imagesc(angle(Object))
167 %         axis image
168 %         title('updating objects phase')
169 %         colorbar
170 %         pause(0.01)
171     end
172 end
173
174 % store updated PIE images in cell
175 % store_updatingObject{1,m} = abs(Object);
176 %% store error: sum squared error after PIE
177 erroraveraged(m) = sum(SSE_E_f(:))/N;
178
179 %% display image as it updates with PIE
180 %     subplot(2,2,3)
181 %     imagesc(abs(Object));
182 %     title('updating amplitude with PIE')
183 %     axis image
184 %     colorbar
185 %     subplot(2,2,4)
186 %     imagesc(angle(Object));
187 %     title('updating phasse with PIE')
188 %     axis image
189 %     colorbar
190 %     pause(0.05);
191 %% probe of PIE (Would not have changes during PIE iterations)
192 L_PIEprobe{m} = L_store_PIE{i,j}(start_P_pos + (j-1)*P_shift : start_P_pos + (j-1)...
193     *P_shift + (spotsize-1), start_P_pos + (i-1)*P_shift : start_P_pos + (i-1)*...
194     P_shift + (spotsize-1));
195 end
196 %% store amplitude and phase of PIE reconstruction
197 Object_PIE = Object;
198 %% Display probe after only PIE reconstruction
199 % figure(4)
200 % subplot(1, 2, 1)
201 % imagesc(abs(L_PIEprobe{m}))
202 % axis image
203 % colorbar
204 % title('Probes amplitude after PIE')
205 % subplot(1, 2, 2)
206 % imagesc((angle((L_PIEprobe{m}))))
207 % title('Probes phase after PIE')
208 % axis image
209 % colorbar
210
211 %%%%%%%%%%%%%%%%%%%%%%%%%%%%%%%%%%%%%%%%%%%%%%%%%%%%%%%%%%%%%%%%%%%%%%%%%%
212 % ePIE
213 %%%%%%%%%%%%%%%%%%%%%%%%%%%%%%%%%%%%%%%%%%%%%%%%%%%%%%%%%%%%%%%%%%%%%%%%%%
214 %% Initial guess of probe in object space, guessed flat top amp + no phase
215 L_store_ePIE = L_store_PIE; % flat top, no phase used for PIE
216
217 %% ePIE
218 for n = 1:iter_ePIE
219     %iterate in a raster scanning left to right then down or resample the
220     %diffraction cell at random positions with
221     % for i = round(rand*(row-0.1)+0.5)
222
223     for i = 1:row % round(rand*(row-0.1)+0.5)
224         for j = 1:col %round(rand*(col-0.1)+0.5)
225             % for each probe position
226             % make Efield intensity
227             Object_E = Object;
228             %initial guess at probe position in object space
229             Object_guess_objectspace = Object_E.*L_store_ePIE{i,j};

```

```

230     Object_guess_Fourierspace = fftshift(fft2(fftshift(Object_guess_objectspace)
    ));
231     %phase of approx
232     p = angle(Object_guess_Fourierspace);
233     %update E with measured I
234     Object_update_Fourierspace = sqrt(abs(images{i,j}))*exp(sqrt(-1).*p);
235     %SSE in diffraction plane
236     SSE_E_f = (abs(Object_update_Fourierspace).^2 - abs(Object_guess_Fourierspace
    ).^2).^2;
237     %updated E field in object space
238     Object_update_objectspace = fftshift(fft2(fftshift(
    Object_update_Fourierspace)));
239     Err = Object_update_objectspace - Object_guess_objectspace;
240 %     SSE_E = (abs(Object_update_objectspace).^2 - abs(Object_guess_objectspace
    ).^2).^2;
241
242     % update function for OBJECT from Maiden and Rodenburg (2009):
243 %     update_function_Objectspace = conj(L_store_ePIE{i,j})./( max((L_store_ePIE
    {i,j}).^2) );
244     %
245     update_function as in PIE:
246     update_function_Objectspace = (conj(L_store_ePIE{i,j})./max(
    max(abs...
247     (L_store_ePIE{i,j})))).*abs(L_store_ePIE{i,j})./...
248     ((abs(L_store_ePIE{i,j})).^2 + alpha);
249
250     % update function for PROBE from Maiden and Rodenburg (2009):
251 %     update_function_L_Objectspace = conj(Object_guess_objectspace)./( max((
    Object_guess_objectspace).^2) );
252     %
253     update_function as in PIE:
254     update_function_L_Objectspace = (conj(Object_guess_objectspace)./
    max(max(abs(...
255     Object_guess_objectspace))))).*abs(Object_guess_objectspace)
256     ./...
257     ((abs(Object_guess_objectspace)).^2 + alpha);
258
259     %new object and probe
260     Object = Object + beta .* update_function_Objectspace .* Err;
261     L_store_ePIE{i,j} = L_store_ePIE{i,j} + gamma .*
262     update_function_L_Objectspace .* Err;
263 %%% Image as it reconstructs with ePIE
264 %     figure(5)
265 %     subplot(221)
266 %     imagesc(abs(Object));
267 %     title('updating image amplitude with ePIE')
268 %     axis image
269 %     colorbar
270 %     subplot(222)
271 %     imagesc(angle(Object));
272 %     title('updating image phasse with ePIE')
273 %     axis image
274 %     colorbar
275 %     subplot(223)
276 %     imagesc(abs(L_store_ePIE{i,j}));
277 %     title('updating probe amplitude with PIE')
278 %     axis image
279 %     colorbar
280 %     subplot(224)
281 %     imagesc(angle(L_store_ePIE{i,j}));
282 %     title('updating probe phasse with PIE')
283 %     axis image
284 %     colorbar
285 %     pause(0.01)
286
287     end
288
289     % store probe updates on the go - doesnot work for random positions
290     L_newProbe_store{n} = L_store_ePIE{i,j}(start_P_pos + (j-1)*P_shift : start_P_pos + (
    j-1)...
291     *P_shift + (spotsize-1), start_P_pos + (i-1)*P_shift : start_P_pos + (i-1)*...
292     P_shift + (spotsize-1));
293
294     % Image probe as it updates after ePIE
295     figure(6)
296     subplot(121)
297     imagesc(abs(L_newProbe_store{n}));
298     title('updating probe amplitude with PIE')

```

```

293 %         axis image
294 %         colorbar
295 %         subplot(122)
296 %         imagesc(angle(L_newProbe_store{n}));
297 %         title('updating probe phasse with ePIE')
298 %         axis image
299 %         colorbar
300 %         pause(0.01)
301
302 %% store error Sum squared error after ePIE
303 erroraveraged_ePIE(n) = sum(SSE_E_f(:))/N;
304 %% display image as it updates with ePIE
305 %         figure(7)
306 %         subplot(221)
307 %         imagesc(abs(Object))
308 %         axis image
309 %         colorbar
310 %         title('updating object amplitude in ePIE');
311 %         subplot(222)
312 %         imagesc(angle(Object))
313 %         colorbar
314 %         title('updating object phase in ePIE');
315 %         axis image
316 %         title('updating of probe in ePIE');
317 %         subplot(223)
318 %         imagesc((abs(L_newProbe_store{n})))
319 %         colorbar
320 %         title('updating amplitude of probe in ePIE');
321 %         axis image
322 %         subplot(224)
323 %         imagesc(angle((L_newProbe_store{n})))
324 %         colorbar
325 %         title('updating phase of probe in ePIE');
326 %         axis image
327 %         pause(0.5)
328 end
329
330 %% store amplitude and phase after ePIE reconstruction: Object and probe
331 % store object / "sample"
332 Object_ePIE = Object;
333 % store probe
334 L_newProbe_ePIE = L_store_ePIE{i,j}(start_P_pos + (j-1)*P_shift : start_P_pos + (j-1)...
335 *P_shift + (spotsize-1), start_P_pos + (i-1)*P_shift : start_P_pos + (i-1)*...
336 P_shift + (spotsize-1));
337
338 %%%%%%%%%%%%%%%%%%%%%%%%%%%%%%%%%%%%%%%%%%%%%%%%%%%%%%%%%%%%%%%%%%%%%%%%%%
339 %% Display ALL ePIE reconstruction
340 %%%%%%%%%%%%%%%%%%%%%%%%%%%%%%%%%%%%%%%%%%%%%%%%%%%%%%%%%%%%%%%%%%%%%%%%%%
341 figure(8)
342 subplot(221)
343 imagesc(abs(f))
344 colorbar
345 axis image
346 title('Amplitude of sample')
347 subplot(222)
348 imagesc(angle(f));
349 colorbar
350 axis image
351 title('Phase associated with sample')
352 subplot(223)
353 imagesc(abs(Probe))
354 colorbar
355 axis image
356 title('Probe's actual amplitude')
357 subplot(224)
358 imagesc(angle(Probe))
359 colorbar
360 axis image
361 title('Probe's actual phase')
362
363 figure(9)
364 subplot(221)
365 imagesc(abs(Object_PIE))
366 colorbar

```

```

367 axis image
368 title('Object's amplitude after PIE')
369 subplot(222)
370 imagesc(angle(Object_PIE));
371 colorbar
372 axis image
373 title('Object's relative phase after PIE')
374 subplot(223)
375 imagesc(abs(L_PIEprobe{m}))
376 colorbar
377 axis image
378 title('Probe's estimated amplitude for PIE')
379 subplot(224)
380 imagesc(angle(L_PIEprobe{m}));
381 colorbar
382 axis image
383 title('Probe's estimated relative phase for PIE')
384
385 figure(10)
386 subplot(221)
387 imagesc(abs(Object_ePIE))
388 colorbar
389 axis image
390 title('Object's Amplitude after ePIE')
391 subplot(222)
392 imagesc(angle(Object_ePIE))
393 colorbar
394 axis image
395 title('Object's relative phase after ePIE')
396 subplot(223)
397 imagesc(abs(L_newProbe_ePIE))
398 colorbar
399 axis image
400 title('Probe's amplitude after ePIE')
401 subplot(224)
402 imagesc(angle(L_newProbe_ePIE))
403 colorbar
404 axis image
405 title('Probe's relative phase after ePIE')
406
407 %% plots of absolute change between iterations
408 figure(11)
409 subplot(1,2,1)
410 plot(1:length(erroraveraged), abs(erroraveraged));
411 title('Absolute change between iterations of PIE (SSE)');
412 xlabel('Number of iterations');
413 ylabel('SSE');
414 subplot(1,2,2)
415 plot(1:length(erroraveraged_ePIE), abs(erroraveraged_ePIE));
416 title('Absolute change between iterations of ePIE (SSE)');
417 xlabel('Number of iterations');
418 ylabel('SSE');

```

### A.3 Experimental results

This code was used in the PIE reconstruction results in section 4.3.2. One directory was created to store the diffraction images (stored as the name *images\_1.tif* for example), and another for the background images taken. These should be inserted in the code where needed.

```

1 clear all;
2 %—Measurement Details: (number of images in each direction, stepsize)—%
3 col = 10;
4 row = 10;
5 numIm = col*row;
6 Pinhole = 300; %in micron
7 micron_step_exper = 100; % in micron
8 %—Reconstruction Parameters—%
9 beta = 0.5;

```

```

10 alpha = 0.001;
11 theta = 0.5;
12 iter = 0;
13 iterPIE = 100;
14 start = 10;
15 %---Cut out size of images (square)---%
16 cutout = 350;
17 %---size of zero padding---%
18 numRows = 2;
19 numcols = 2;
20 coladd = complex(zeros(cutout*2,cutout*2*numrows));
21 rowadd = complex(zeros(cutout*2*numrows,cutout*2*(numrows+numcols+1)));
22
23 Probe_size = 40;
24 FWHM_newProbe = 40/2.355; %100 - probe used for PIE
25 newProbe_option = 1; %1 for flattop, 0 for gaussian to be used as probe
26 %---resized image dimension---%
27 res = 800;
28
29 %% READ IN IMAGES
30 file = dir('*.tif');
31 NF = length(file); % number of 'file's (jpegs) in the folder.
32 for back = 1:1:5
33     Background{back} = double(imread([ 'C:\Users\labuser\Documents\Anneke - Ptychography
        \24 Oct 2016\Transparency (2) Corner 10x10 100 micron steps\Background\image_',
        num2str(back+505), '.tif' ]));
34 end
35 % Average over 5 images of the background taken
36 Background = (Background{1}+Background{2}+Background{3}+Background{4}+Background{5})/5;
37
38 for i = 1:1:numIm
39     for k = 1:1:5
40         % Read in images
41         images_read1{i,k} = double(imread([ 'image_', num2str(k+5*(i-1)), '.tif' ]));
42         % Subtract average background from each image
43         images_read1{i,k} = images_read1{i,k} - Background;
44         % Set all pixels with vaue below 0 to 0
45         neg = find(images_read1{i,k}<0);
46         images_read1{i,k}(neg) = 0;
47     end
48 end
49 % Average over 5 images taken at measurement each point
50 for i = 1:1:numIm
51     images_read{i} = (images_read1{i,1}+images_read1{i,2}+images_read1{i,3}+images_read1{
        i,4}+images_read1{i,5})/5;
52     % Cut out a region around the center of the diffraction
53     images_read{i} = images_read{i}(500-cutout:500+cutout-1,...
        700-cutout:700+cutout-1);
54 end
55
56
57 %% NOISE SUBSTRACTION AND NORMALIZATION
58 % Average over the pixel intensity of a square on the edge of the image
59 for t = 1:1:numIm
60     noise_level(t) = mean(mean(images_read{t}(1:100,1:100)));
61 end
62 % Average
63 Noise_Level = mean(noise_level);
64 for t = 1:1:numIm
65     images_read{t} = images_read{t}-1*Noise_Level;
66     neg = find(images_read{t}<0);
67     images_read{t}(neg) = 0;
68 end
69 for t = 1:1:numIm
70     max_im(t) = max(max(images_read{t}));
71 end
72 for zd = 1:1:numIm
73     images_read{zd} = images_read{zd}./abs(max(max_im));
74 end
75
76 %% ZEROPADDING AND DIGITAL ENHANCEMENT
77
78 % Iterate through all images and add zeros as border
79 for zeropad = 1:1:numIm
80     images_wihout{zeropad} = images_read{zeropad};

```



```

81     %—Zeropadding of images—%
82     images_read{zeropad} = [coladd images_read{zeropad} coladd];
83     images_read{zeropad} = [rowadd; images_read{zeropad}; rowadd];
84     % resize image
85     images_read{zeropad} = imresize(images_read{zeropad}, [res res]);
86 end
87
88
89 %% NORMALIZATION
90
91 for t = 1:1:numIm
92     images_read{t} = (images_read{t});
93     max_im(t) = max(max(images_read{t}));
94 end
95 for zeropad = 1:1:numIm
96     images_read{zeropad} = images_read{zeropad} ./ abs(max(max_im));
97     neg1 = find(images_read{zeropad} < 0);
98     images_read{zeropad}(neg1) = 0;
99     images_read{zeropad} = (sqrt(images_read{zeropad}));
100
101 end
102 images = transpose(reshape(images_read, [col, row]));
103
104 %% READ PROBE INFORMATION
105 %
106 % Probe_airy = (double(imread('Probe.tif')));
107 % Probe_airy = Probe_airy - Background;
108 % max_probe = max(max(Probe_airy));
109 % neg = find(Probe_airy < 0);
110 % Probe_airy(neg) = 0;
111 % [r, c] = find(Probe_airy == max(Probe_airy(:)));
112 % Probe_airy = Probe_airy(round(mean(r)) - cutout : round(mean(r)) ...
113 %     + cutout - 1, round(mean(c)) - cutout : round(mean(c)) + cutout - 1);
114 % Probe_array = imresize(Probe_airy, [res res]);
115 % Probe_array = Probe_array(res/2, :);
116
117 %% SETTING UP RECONSTRUCTION PARAMETERS
118
119 dimensions = size(images{1,1}); %size of probe image measured
120 dim = dimensions(1);
121 spotsize = round(FWHM_newProbe*2.355*1.5); %matrix size
122 % F_newProbe is flat top, no phase, probe used in PIE, made same size as
123 % real probe.
124 F_newProbe = fspecial('gaussian', spotsize, FWHM_newProbe);
125 F_newProbe = F_newProbe ./ max(max(F_newProbe));
126 if newProbe_option == 1
127     % if this == 0, the estimate for probe starts as a Gaussian default
128     I = find(F_newProbe > 0.5);
129     I2 = find(F_newProbe <= 0.5);
130     F_newProbe(I) = 1;
131     F_newProbe(I2) = 0;
132 end
133 spot_mask = F_newProbe;
134 sum_F = sum(sum(F_newProbe));
135 P_shift = round(Probe_size*micron_step_exper/Pinhole);
136
137 %%%%%%%%%%%%%%%%%%%%%%%%%%%%%%%%%%%%%%%%%%%%%%%%%%%%%%%%%%%%%%%%%%%%%%%%%%%
138 %% PIE
139 %%%%%%%%%%%%%%%%%%%%%%%%%%%%%%%%%%%%%%%%%%%%%%%%%%%%%%%%%%%%%%%%%%%%%%%%%%%
140
141 % Initial guess of object as zero matrix
142 Object = complex(zeros(dim), zeros(dim));
143
144 for m = 1:1:iterPIE
145     for i = 1:row%round(rand*9.9+0.5)
146         for j = 1:col%round(rand*9.9+0.5)
147
148             P_shift = round(Probe_size*micron_step_exper/Pinhole);
149             % P_shift = P_shift+round((2*rand-1)*0.05*P_shift);
150
151             % for even/odd iteration numbers scan probe horizontal/vertical first
152             if mod(m,2) == 1
153                 % make matrix for probe to move on
154                 Probe_Matrix = zeros(dimensions(1)+1000, dimensions(2)+1000);

```

```

155     Probe_Matrix(start+(i-1)*P_shift : start+(i-1)*P_shift + ...
156         spotsize-1, start+(j-1)*P_shift : start+(j-1)*P_shift ...
157         +spotsize-1) = F_newProbe;
158     Probe_Matrix = Probe_Matrix(1:dim, 1:dim);
159
160     Object_Guess = Object.*Probe_Matrix; % object guess
161
162     % measured amplitude and guessed phase done in freq space
163     % then whole thing changed back to object space
164     Obj_update = fftshift(iff2(fftshift(((images{i,j})) ...
165         .*exp(sqrt(-1).*angle(fftshift(fft2(fftshift ...
166         ((Object_Guess)))))))));
167     Err = Obj_update - Object_Guess; %done in object space
168
169     update_function_Object = (conj(Probe_Matrix)./max(max(abs ...
170         (Probe_Matrix)))).*abs(Probe_Matrix)./...
171         (conj(Probe_Matrix).*Probe_Matrix+alpha);
172
173     Object = Object + beta .* update_function_Object .* Err;
174
175     F_newProbe = Probe_Matrix(start+(i-1)*P_shift : start+(i-1) ...
176         *P_shift+(spotsize-1), start+(j-1)*P_shift : start+(j-1) ...
177         *P_shift+(spotsize-1));
178     end
179
180     if mod(m,2) == 0
181         % make matrix for probe to move on
182         Probe_Matrix = zeros(dimensions(1)+1000,dimensions(2)+1000);
183         Probe_Matrix(start+(j-1)*P_shift : start+(j-1)*P_shift + ...
184             spotsize-1, start+(i-1)*P_shift : start+(i-1)*P_shift ...
185             +spotsize-1) = F_newProbe;
186         Probe_Matrix = Probe_Matrix(1:dim, 1:dim);
187
188         Object_Guess = Object.*Probe_Matrix; % object guess
189
190         % measured amplitude and guessed phase done in freq space
191         % then whole thing changed back to object space
192         Obj_update = fftshift(iff2(fftshift(((images{j,i})) ...
193             .*exp(sqrt(-1).*angle(fftshift(fft2(fftshift ...
194             ((Object_Guess)))))))));
195
196         Err = Obj_update - Object_Guess; % done in object space
197
198         update_function_Object = (conj(Probe_Matrix)./max(max(abs ...
199             (Probe_Matrix)))).*abs(Probe_Matrix)./...
200             (conj(Probe_Matrix).*Probe_Matrix+alpha);
201
202         Object = Object + beta .* update_function_Object .* Err;
203
204         F_newProbe = Probe_Matrix(start+(j-1)*P_shift : start+(j-1) ...
205             *P_shift+(spotsize-1), start+(i-1)*P_shift : start+(i-1) ...
206             *P_shift+(spotsize-1));
207     end
208     end
209     end
210 end
211
212 % store the object from the PIE reconstruction
213 Object_PIE = Object;
214 Err_PIE = Err;
215 Obj_update_PIE = Obj_update;
216
217 %%%%%%%%%%%%%%%%%%%%%%%%%%%%%%%%%%%%%%%%%%%%%%%%%%%%%%%%%%%%%%%%%%%%%%%%%
218 %% EPIE
219 %%%%%%%%%%%%%%%%%%%%%%%%%%%%%%%%%%%%%%%%%%%%%%%%%%%%%%%%%%%%%%%%%%%%%%%%%
220
221 % make matrix for probe to move on
222 Probe_Matrix = zeros(dimensions(1)+1000,dimensions(2)+1000);
223
224 for n = 1:1:iter
225     for i = 1:1:row
226         for j = 1:1:col
227             P_shift = round(Probe_size*micron_step_exper/Pinhole);
228             % P_shift = P_shift+round((2*rand-1)*0.2*P_shift);

```

```

229
230 % for even/odd iteration numbers scan probe horizontal/vertical first
231 if mod(m,2) == 0
232     Probe_Matrix ( start+(i-1)*P_shift : start+(i-1)*P_shift + ...
233         spotsize-1, start+(j-1)*P_shift : start+(j-1)*P_shift ...
234         +spotsize-1) = F_newProbe;
235     Probe_Matrix = Probe_Matrix (1:dim, 1:dim);
236
237     Object_Guess = Object .* Probe_Matrix; % object guess
238
239     % measured amplitude and guessed phase done in freq space
240     % then whole thing changed back to object space
241     Obj_update = fftshift ( ifft2 ( fftshift ( (((images{i,j})) ...
242         .* exp (sqrt(-1) .* angle ( fftshift ( fft2 ( fftshift ...
243         ((Object_Guess))))))));
244
245     Err = Obj_update - Object_Guess; % in object space
246
247     % update function for the object:
248     update_function_Object = ( conj (Probe_Matrix) ./ max (max (abs (...
249         Probe_Matrix))) .* abs (Probe_Matrix) ./ ( conj (Probe_Matrix) ...
250         .* Probe_Matrix + alpha);
251     % update function for the probe:
252     update_function_Probe = ( conj (Object_Guess) ./ max (max (abs (...
253         Object_Guess))) .* abs (Object_Guess) ./ ( conj (Object_Guess) ...
254         .* Object_Guess + alpha);
255     % update the object
256     Object = Object + beta .* update_function_Object .* Err;
257     % update the probe
258     Probe_Matrix = Probe_Matrix + theta .* ...
259         update_function_Probe .* Err;
260
261     F_newProbe = Probe_Matrix ( start+(i-1)*P_shift : start+(i-1) ...
262         *P_shift+(spotsize-1), start+(j-1)*P_shift : start+(j-1) * ...
263         P_shift+(spotsize-1));
264 end
265
266 if mod(m,2) == 1
267     %
268         Probe_Matrix = zeros ( dimensions (1)+1000, dimensions (2)
269         +1000);
270     Probe_Matrix ( start+(j-1)*P_shift : start+(j-1)*P_shift + ...
271         spotsize-1, start+(i-1)*P_shift : start+(i-1)*P_shift ...
272         +spotsize-1) = F_newProbe;
273     Probe_Matrix = Probe_Matrix (1:dim, 1:dim);
274
275     Object_Guess = Object .* Probe_Matrix; % object guess
276
277     % measured amplitude and guessed phase done in freq space
278     % then whole thing changed back to object space
279     Obj_update = fftshift ( ifft2 ( fftshift ( (((images{j,i})) ...
280         .* exp (sqrt(-1) .* angle ( fftshift ( fft2 ( fftshift ...
281         ((Object_Guess))))))));
282
283     Err = Obj_update - Object_Guess; % in object space
284
285     % update function for the object:
286     update_function_Object = ( conj (Probe_Matrix) ./ max (max (abs (...
287         Probe_Matrix))) .* abs (Probe_Matrix) ./ ( conj (Probe_Matrix) ...
288         .* Probe_Matrix + alpha);
289     % update function for the probe:
290     update_function_Probe = ( conj (Object_Guess) ./ max (max (abs (...
291         Object_Guess))) .* abs (Object_Guess) ./ ( conj (Object_Guess) ...
292         .* Object_Guess + alpha);
293     % update the object:
294     Object = Object + beta .* update_function_Object .* Err;
295     % update the probe:
296     Probe_Matrix = Probe_Matrix + theta .* ...
297         update_function_Probe .* Err;
298
299     F_newProbe = Probe_Matrix ( start+(j-1)*P_shift : start+(j-1) ...
300         *P_shift+(spotsize-1), start+(i-1)*P_shift : start+(i-1) * ...
301         P_shift+(spotsize-1));
302 end
303 end

```

```

302     end
303 end
304
305 F_newProbe = Probe_Matrix(start+(j-1)*P_shift : start+(j-1)...
306     *P_shift+(spotsize-1), start+(i-1)*P_shift : start+(i-1)*...
307     P_shift+(spotsize-1));
308
309 %% FIGURES
310
311 % plot the PIE and ePIE reconstruction as well as probe reconstruction
312 % using ePIE. cut out to display the section where the image is and
313 % remove border with no object information.
314 figure(1)
315 %...
316 subplot(3,2,3)
317 imagesc(abs(Object(start : start+col*P_shift+spotsize, start : ...
318     start+row*P_shift+spotsize).^2))
319 colorbar
320 daspect([1 1 1])
321 title('Object after ePIE')
322 colormap hsv
323 subplot(3,2,4)
324 imagesc(angle(Object(start : start+col*P_shift+spotsize, start : ...
325     start+row*P_shift+spotsize)))
326 colorbar
327 daspect([1 1 1])
328 title('Object's Phase after ePIE')
329 colormap hsv
330 subplot(3,2,5)
331 imagesc(abs(F_newProbe))
332 colorbar
333 daspect([1 1 1])
334 title('Probe after ePIE')
335 colormap jet
336 subplot(3,2,6)
337 imagesc(angle(F_newProbe))
338 colorbar
339 daspect([1 1 1])
340 title('Probe's Phase after ePIE')
341
342 figure(2)
343 subplot(3,2,3)
344 imagesc(abs(Object))
345 colorbar
346 daspect([1 1 1])
347 title('Object after ePIE')
348 colormap hsv
349 subplot(3,2,4)
350 imagesc(angle(Object))
351 colorbar
352 daspect([1 1 1])
353 title('Object's Phase after ePIE')
354 colormap hsv
355 subplot(3,2,5)
356 imagesc(abs(F_newProbe))
357 colorbar
358 daspect([1 1 1])
359 title('Probe after ePIE')
360 colormap jet
361 subplot(3,2,6)
362 imagesc(angle(F_newProbe))
363 colorbar
364 daspect([1 1 1])
365 title('Probe's Phase after ePIE')
366
367 figure(3)
368 subplot(2,2,1)
369 imagesc(((abs(Object(start : start+col*P_shift+spotsize, start : ...
370     start+row*P_shift+spotsize))))))
371 colorbar
372 colormap jet
373 daspect([1 1 1])
374 title('Object after PIE')
375 subplot(2,2,3)

```

```
376 imagesc((angle(Object(start:start+col*P_shift+spotsize, start:...
377     start+row*P_shift+spotsize+1))))
378 colorbar
379 daspect([1 1 1])
380 title('Object's Phase after PIE')
```

# List of References

- [1] Zipfel, W.R., Williams, R.M. and Webb, W.W.: Nonlinear magic: multiphoton microscopy in the biosciences. *Nature Biotechnology*, vol. 21, no. 11, pp. 1369–1377, 2003. ISSN 1087-0156.
- [2] Masters, B.R. and So, P.T.C. (eds.): *Handbook of Biomedical Nonlinear Optical Microscopy*. Oxford University Press, Oxford, 2008. ISBN 9780195162608.
- [3] Liu, Y., Tu, H., Benalcazar, W.A., Chaney, E.J. and Boppart, S.A.: Multimodal nonlinear microscopy by shaping a fiber supercontinuum from 900 to 1160nm. *IEEE Journal on Selected Topics in Quantum Electronics*, vol. 18, no. 3, pp. 1209–1214, 2012. ISSN 1077260X.
- [4] Ashkin, A.: Acceleration and Trapping of Particles by Radiation Pressure. *Physical Review Letters*, vol. 24, no. 4, pp. 156–159, 1970. ISSN 00319007.
- [5] Ashkin, A., Dziedzic, J.M., Bjorkholm, J.E. and Chu, S.: Observation of a single-beam gradient force optical trap for dielectric particles. *Optics Letters*, vol. 11, no. 5, pp. 288–290, 1986. ISSN 0146-9592.
- [6] Moffitt, J.R., Chemla, Y.R., Smith, S.B. and Bustamante, C.: Recent Advances in Optical Tweezers. *Annual Review of Biochemistry*, vol. 77, pp. 205–228, 2008. ISSN 0066-4154.
- [7] Finer, J.T., Simmons, R.M. and Spudich, J.A.: Single myosin molecule mechanics: piconewton forces and nanometre steps. *Nature*, vol. 368, no. 6467, pp. 113–118, 1994. ISSN 0028-0836.
- [8] Kulin, S., Kishore, R., Helmerson, K. and Locascio, L.: Optical Manipulation and Fusion of Liposomes as Microreactors. *Langmuir*, vol. 19, no. 20, pp. 8206–8210, 2003. ISSN 0743-7463.
- [9] Berns, M.W.: Laser Scissors and Tweezers. *Scientific American*, vol. 278, no. 4, pp. 62–67, 1998. ISSN 0036-8733.
- [10] Neuman, K.C. and Block, S.M.: Optical trapping. *Review of Scientific Instruments*, vol. 75, no. 9, pp. 2787–2809, 2004. ISSN 0034-6748.
- [11] Ashkin, A. and Dziedzic, J.: Optical trapping and manipulation of viruses and bacteria. *Science*, vol. 235, no. 4795, pp. 1517–1520, 1987. ISSN 0036-8075.
- [12] Ashkin, A. and Dziedzic, J.M.: Internal cell manipulation using infrared laser traps. *Proceedings of the National Academy of Sciences*, vol. 86, no. 20, pp. 7914–7918, 1989. ISSN 0027-8424.
- [13] Smith, S.B., Cui, Y. and Bustamante, C.: Overstretching B-DNA: The Elastic Response of Individual Double-Stranded and Single-Stranded DNA Molecules. *Science*, vol. 271, no. 5250, pp. 795–799, 1996. ISSN 0036-8075.

- [14] Jones, P.H., Maragò, O.M. and Volpe, G.: *Optical tweezers: principles and applications*. Cambridge University Press, United Kingdom, 2015. ISBN 9781107051164.
- [15] Fällman, E., Schedin, S., Jass, J., Andersson, M., Uhlin, B.E. and Axner, O.: Optical tweezers based force measurement system for quantitating binding interactions: system design and application for the study of bacterial adhesion. *Biosensors and Bioelectronics*, vol. 19, no. 11, pp. 1429–1437, 2004. ISSN 09565663.
- [16] Blehm, B.H., Schroer, T.A., Trybus, K.M., Chemla, Y.R. and Selvin, P.R.: In vivo optical trapping indicates kinesin's stall force is reduced by dynein during intracellular transport. *Proceedings of the National Academy of Sciences*, vol. 110, no. 9, pp. 3381–3386, 2013. ISSN 0027-8424.
- [17] Schermelleh, L., Heintzmann, R. and Leonhardt, H.: A guide to super-resolution fluorescence microscopy. *The Journal of Cell Biology*, vol. 190, no. 2, pp. 165–175, 2010. ISSN 0021-9525.
- [18] Maiden, A.M., Rodenburg, J.M. and Humphry, M.J.: Optical ptychography: a practical implementation with useful resolution. *Optics Letters*, vol. 35, no. 15, pp. 2585 – 2587, 2010. ISSN 0146-9592.
- [19] Rodenburg, J., Hurst, A. and Cullis, A.: Transmission microscopy without lenses for objects of unlimited size. *Ultramicroscopy*, vol. 107, no. 2-3, pp. 227–231, 2007. ISSN 03043991.
- [20] Marrison, J., Rätty, L., Marriott, P. and O'Toole, P.: Ptychography - a label free, high-contrast imaging technique for live cells using quantitative phase information. *Scientific Reports*, vol. 3, no. 2369, pp. 1 – 7, 2013. ISSN 2045-2322.
- [21] Denk, W., Strickler, J. and Webb, W.: Two-photon laser scanning fluorescence microscopy. *Science*, vol. 248, no. 4951, pp. 73–76, 1990. ISSN 0036-8075.
- [22] So, P.T.: Two-photon Fluorescence Light Microscopy. In: *Encyclopedia Of Life Sciences*, pp. 1–5. Macmillan Publishers Ltd, Chichester, 2002. ISBN 9780470015902.
- [23] Xu, C. and Webb, W.W.: Measurement of two-photon excitation cross sections of molecular fluorophores with data from 690 to 1050 nm. *Journal of the Optical Society of America B*, vol. 13, no. 3, pp. 481 – 491, 1996. ISSN 0740-3224.
- [24] Boyd, R.W.: *Nonlinear Optics*. 3rd edn. Boston: Academic Press, Amsterdam, 2008. ISBN 9786611763695.
- [25] Cox, G., Kable, E., Jones, A., Fraser, I., Manconi, F. and Gorrell, M.D.: 3-Dimensional imaging of collagen using second harmonic generation. *Journal of Structural Biology*, vol. 141, no. 1, pp. 53–62, 2003. ISSN 10478477.
- [26] Barad, Y., Eisenberg, H., Horowitz, M. and Silberberg, Y.: Nonlinear scanning laser microscopy by third harmonic generation. *Applied Physics Letters*, vol. 70, no. 8, pp. 922–924, 1997. ISSN 0003-6951.
- [27] Graf, B. and Boppart, S.: Multimodal in vivo skin imaging with integrated optical coherence and multiphoton microscopy. *IEEE Journal of Selected Topics in Quantum Electronics*, vol. 18, no. 4, pp. 1280 – 1286, 2011. ISSN 1077-260X.
- [28] Arkhipov, S.N., Saytashev, I. and Dantus, M.: Intravital Imaging Study on Photodamage Produced by Femtosecond Near-infrared Laser Pulses In Vivo. *Photochemistry and Photobiology*, vol. 92, no. 2, pp. 308–313, 2016. ISSN 00318655.

- [29] Liu, Y., King, M., Tu, H., Zhao, Y. and Boppart, S.: Broadband nonlinear vibrational spectroscopy by shaping a coherent fiber supercontinuum. *Optics express*, vol. 21, no. 7, pp. 8269 – 8275, 2013. ISSN 1094-4087.
- [30] Lang, M.J., Fordyce, P.M., Engh, A.M., Neuman, K.C. and Block, S.M.: Simultaneous, coincident optical trapping and single-molecule fluorescence. *Nature methods*, vol. 1, no. 2, pp. 1 – 7, 2004. ISSN 1548-7091.
- [31] van Dijk, M.A., Kapitein, L.C., van Mameren, J., Schmidt, C.F. and Peterman, E.J.G.: Combining optical trapping and single-molecule fluorescence spectroscopy: enhanced photobleaching of fluorophores. *The journal of physical chemistry. B*, vol. 108, no. 20, pp. 6479–6484, 2004. ISSN 1932-7447.
- [32] Agate, B., Brown, C.T.A., Sibbett, W. and Dholakia, K.: Femtosecond optical tweezers for in-situ control of two-photon fluorescence. *Optics Express*, vol. 12, no. 13, pp. 3011 – 3017, 2004. ISSN 1094-4087.
- [33] Petrov, D.V.: Raman spectroscopy of optically trapped particles. *Journal of Optics A: Pure and Applied Optics*, vol. 9, no. 8, pp. S139–S156, 2007. ISSN 1464-4258.
- [34] Kas, J.A.U.o.L.: Optical Traps.  
Available at: <http://home.uni-leipzig.de/pwm/web/?section=introduction&page=opticaltraps>
- [35] Bechhoefer, J. and Wilson, S.: Faster, cheaper, safer optical tweezers for the undergraduate laboratory. *American Journal of Physics*, vol. 70, no. 4, pp. 393 – 400, 2002. ISSN 00029505.
- [36] Mas, J., Farré, A., Cuadros, J., Juvells, I. and Carnicer, A.: Understanding optical trapping phenomena: A simulation for undergraduates. *IEEE Transactions on Education*, vol. 54, no. 1, pp. 133–140, 2011. ISSN 00189359.
- [37] Tlustý, T., Meller, A. and Bar-Ziv, R.: Optical Gradient Forces of Strongly Localized Fields. *Physical Review Letters*, vol. 81, no. 8, pp. 1738–1741, 1998. ISSN 0031-9007.
- [38] Appleyard, D.C., Vandermeulen, K.Y., Lee, H. and Lang, M.J.: Optical trapping for undergraduates. *American Journal of Physics*, vol. 75, no. 1, pp. 5–14, 2007. ISSN 0002-9505.
- [39] Berg-Sørensen, K. and Flyvbjerg, H.: Power spectrum analysis for optical tweezers. *Review of Scientific Instruments*, vol. 75, no. 3, pp. 594–612, 2004. ISSN 00346748.
- [40] Gittes, F. and Schmidt, C.F.: Thermal noise limitations on micromechanical experiments. *European Biophysics Journal*, vol. 27, no. 1, pp. 75–81, 1998. ISSN 01757571.
- [41] Batchelor, G.K.: *An Introduction to Fluid Dynamics*. Cambridge University Press, Cambridge, 1967. ISBN 9780511800955.
- [42] Howard, J.: *Mechanics of Motor Proteins and the Cytoskeleton*. Sinauer Associates, Inc., Sunderland (Massachusetts), 2001. ISBN 0878933344.
- [43] Padgett, M. and Di Leonardo, R.: Holographic optical tweezers and their relevance to lab on chip devices. *Lab on a Chip*, vol. 11, no. 7, pp. 1196 – 1205, 2011. ISSN 1473-0197.
- [44] Lodish, H., Berk, A., Zipursky, S.L., Matsudaira, P., Baltimore, D. and Darnell, J.: *Molecular Cell Biology*. 4th edn. W. H. Freeman and Company, New York, N.Y., 1999. ISBN 071673706X.



- [45] Yildiz, A. and Selvin, P.R.: Fluorescence imaging with one nanometer accuracy: Application to molecular motors. *Accounts of Chemical Research*, vol. 38, no. 7, pp. 574–582, 2005. ISSN 00014842.
- [46] Alhadeff, R. and Warshel, A.: Reexamining the origin of the directionality of myosin V. *Proceedings of the National Academy of Sciences*, vol. 114, no. 39, pp. 10426 – 10431, 2017. ISSN 0027-8424.
- [47] Cheney, R.E., O’Shea, M.K., Heuser, J.E., Coelho, M.V., Wolenski, J.S., Espreafico, E.M., Forscher, P., Larson, R.E. and Mooseker, M.S.: Brain myosin-V is a two-headed unconventional myosin with motor activity. *Cell*, vol. 75, no. 1, pp. 13–23, 1993. ISSN 00928674.
- [48] Coy, D.L., Wagenbach, M. and Howard, J.: Kinesin takes one 8-nm step for each ATP that it hydrolyzes. *Journal of Biological Chemistry*, vol. 274, no. 6, pp. 3667–3671, 1999. ISSN 00219258.
- [49] MIT department of Physics: Optical trapping. Tech. Rep., MIT, 2012.
- [50] Mehta, A.D., Rock, R.S., Rief, M., Spudich, J.A., Mooseker, M.S. and Cheney, R.E.: Myosin-V is a processive actin-based motor. *Nature*, vol. 400, no. 6744, pp. 590–593, 1999. ISSN 0028-0836.
- [51] Maiden, A.M. and Rodenburg, J.M.: An improved ptychographical phase retrieval algorithm for diffractive imaging. *Ultramicroscopy*, vol. 109, no. 10, pp. 1256–1262, 2009. ISSN 03043991.
- [52] Faulkner, H. and Rodenburg, J.: Error tolerance of an iterative phase retrieval algorithm for moveable illumination microscopy. *Ultramicroscopy*, vol. 103, no. 2, pp. 153–164, 2005. ISSN 03043991.
- [53] Rodenburg, J.M. and Faulkner, H.M.L.: A phase retrieval algorithm for shifting illumination. *Applied Physics Letters*, vol. 85, no. 20, pp. 4795–4797, 2004. ISSN 0003-6951.
- [54] Goodman, J.W.: *Introduction to Fourier Optics*. 3rd edn. Roberts & Company, Englewood, Colorado, 2005. ISBN 978-0974707723.
- [55] Vanhecke, D., Graber, W. and Studer, D.: Chapter 9 Close-to-Native Ultrastructural Preservation by High Pressure Freezing. In: *Methods in cell biology, volume 88*, chap. 9, pp. 151–164. Elsevier Inc., Bern, Switzerland, 2008.
- [56] Lee, W.M., Reece, P.J., Marchington, R.F., Metzger, N.K. and Dholakia, K.: Construction and calibration of an optical trap on a fluorescence optical microscope. *Nature Protocols*, vol. 2, no. 12, pp. 3226–3238, 2007. ISSN 1754-2189.
- [57] Olympus (Olympus Corporation).  
Available at: [http://www.olympus-ims.com/en/microscope/terms/luminous\\_flux/](http://www.olympus-ims.com/en/microscope/terms/luminous_flux/)
- [58] Kubitscheck, U. (ed.): *Fluorescence Microscopy: From Principles to Biological Applications*. Wiley-Blackwell, Weinheim, Germany, 2013. ISBN 9783527329229.
- [59] Thorlabs: TPA101 Beam Position Aligner User Guide. 2016.
- [60] Pedrós, R., Moya, I., Goulas, Y. and Jacquemoud, S.: Chlorophyll fluorescence emission spectrum inside a leaf. *Photochemical & Photobiological Sciences*, vol. 7, no. 4, pp. 498 – 502, 2008. ISSN 1474-905X.

- [61] Smith, S.P., Bhalotra, S.R., Brody, A.L., Brown, B.L., Boyda, E.K. and Prentiss, M.: Inexpensive optical tweezers for undergraduate laboratories. *American Journal of Physics*, vol. 67, no. 1, pp. 26–35, 1999. ISSN 0002-9505.
- [62] Ott, A., Magnasco, M., Simon, A. and Libchaber, A.: Measurement of the persistence length of polymerized actin using fluorescence microscopy. *Physical Review E*, vol. 48, no. 3, pp. R1642–R1645, 1993. ISSN 1063-651X.